

DISSERTATION

IMAGING SINGLE BARIUM ATOMS IN SOLID XENON FOR BARIUM TAGGING IN THE
NEXO NEUTRINOLESS DOUBLE BETA DECAY EXPERIMENT

Submitted by

Timothy Walton

Department of Physics

In partial fulfillment of the requirements

For the Degree of Doctor of Philosophy

Colorado State University

Fort Collins, Colorado

Fall 2015

Doctoral Committee:

Advisor: William M. Fairbank, Jr.

Bruce Berger
Alan Van Orden
Robert Wilson

Copyright by Timothy Walton 2015

All Rights Reserved

ABSTRACT

The nEXO experiment will search for neutrinoless double beta decay of the isotope ^{136}Xe in a ton-scale liquid Xe time projection chamber, in order to probe the Majorana nature of neutrinos. Detecting the daughter (^{136}Ba) of double beta decay events, called barium tagging, is a technique under investigation which would provide a veto for a background-free measurement. This would involve detecting a single barium ion from within a macroscopic volume of liquid xenon. One proposed barium tagging method is to trap the barium ion in solid xenon (SXe) at the end of a cold probe, and then detect it by its fluorescence in the solid xenon. In this thesis, new studies on the spectroscopy of deposits of Ba and Ba^+ in solid Xe are presented. Imaging of Ba atoms in solid Xe is demonstrated with ultimate sensitivity down to the single atom level. Achievement of this level of sensitivity is a major step toward barium tagging by this method.

ACKNOWLEDGEMENTS

I thank my adviser William M. Fairbank, Jr. with inadequate words for his inspiring courage, foresight, and intuition as a physicist. The success of this thesis, those to come, and of the experimental method which they work toward belongs foremost to him. Special thanks also to Chris Chambers for tireless help with experiment and analysis, and ambition to continue the work. I thank him and Adam Craycraft for companionship and intellectual input. I thank Shon Cook and Brian Mong for developing the apparatus, pioneering the work, and training me along with Cesar Benitez and Kendy Hall. I also thank the nEXO collaboration for their support, and especially their spokesman Giorgio Gratta. I thank my wife for supporting and enduring the physicist lifestyle, and everyone in my family for inspiration and vital support.

This dissertation is typset in L^AT_EX using a document class designed by Leif Anderson.

Dedicated to my new son Logan.

TABLE OF CONTENTS

Abstract	ii
Acknowledgements	iii
Chapter 1. Introduction	1
1.1. Neutrinos	2
1.2. Double Beta Decay	6
1.3. Enriched Xenon Observatory	8
Chapter 2. Theory	20
2.1. Ba/Ba ⁺ Spectroscopy in Vacuum	20
2.2. 5-level System	22
2.3. Matrix Isolation Spectroscopy	26
2.4. Fluorescence Efficiency	28
Chapter 3. Experimental	31
3.1. Ion Beam	31
3.2. Ba Getter Source	40
3.3. Sample Deposition	41
3.4. Laser Excitation	43
3.5. Collection Optics	47
3.6. Wavelength Calibration	49
3.7. Vibrations and Effective Laser Region	50
3.8. Laser Scanning	52
Chapter 4. Method	54

4.1. Fitting of Spectra	54
4.2. Background Spectra	56
Chapter 5. Results: Spectroscopy	62
5.1. Excitation and Emission of Ba in SXe.....	62
5.2. 619-nm Peak Attribution.....	65
5.3. Annealing/Temperature Dependence	66
5.4. Bleaching.....	69
5.5. Blue Excitation / Candidate Ba ⁺ Lines	78
Chapter 6. Results: Imaging	80
6.1. Imaging 577- and 591-nm Fluorescence.....	80
6.2. Imaging 619-nm Fluorescence	81
6.3. Scanned Images.....	86
Chapter 7. Conclusions	89
7.1. Future Work.....	89
Bibliography	92

CHAPTER 1

INTRODUCTION

Neutrinos are elusive fundamental particles of great importance in the continuing study of particle physics. Though extremely difficult to study, with tiny yet non-zero masses, no electric charge, and low interaction cross-sections, neutrinos have provided great insight into nuclear physics, geophysics, astrophysics, and may provide the key to understanding the matter/anti-matter asymmetry of the universe. Neutrinos were first predicted by W. Pauli in 1930. He proposed the existence of a neutral, unobserved particle to explain the apparent violation of energy conservation in beta decay [1]. He admitted that neutrinos (then deemed “neutrons” – what we now know as neutrons had not been discovered yet either) should be difficult to observe experimentally, but also that it seemed unlikely that they would never have been noticed before. As it turns out, they are much more difficult to observe than he predicted. Their probabilities for interaction are extremely small.

A theory formulated in 1933 by E. Fermi for beta decay [2], including the neutrino, was the beginning of weak interaction theory. Eventually, progress led to a unified treatment of electromagnetic, weak and strong forces and the development of the very successful Standard Model (SM) of particle physics. In the SM, neutrinos are massless. The discovery of non-zero neutrino mass via neutrino oscillations in the late 1990s [3] shows that there is more new physics to be discovered beyond the SM, and presents a path to follow.

The See-saw Mechanism is a theory which explains the extreme lightness of neutrinos compared to other particles, while also predicting very heavy neutrino partners. The existence of heavy neutrinos in the high-energy environment of the early universe, coupled with

the possibility of the violation of CP conservation in decays of these heavy neutrinos, could explain why the universe became dominated by matter. [4]

If neutrinos are Majorana particles rather than Dirac particles, the process of neutrinoless double beta decay ($0\nu\beta\beta$) is allowed if the neutrino mass is non-zero. Observation of $0\nu\beta\beta$ would simultaneously demonstrate that neutrinos are Majorana particles, as well as aid in determining the absolute mass itself [5]. This chapter outlines the current theory for neutrinos, and then describes the $0\nu\beta\beta$ experiments EXO-200 and nEXO, in order to motivate barium tagging for nEXO.

1.1. NEUTRINOS

Neutrinos are chargeless leptons which only interact via the weak force (and gravity). There are three known “flavors” of neutrinos, ν_e , ν_μ , and ν_τ , each corresponding to one of the three known leptons. These are the eigenstates in the basis of the weak force, so they are the states in which a neutrino will interact via the weak force.

1.1.1. NEUTRINO OSCILLATION AND MASS

If neutrinos have an energy basis which is different from the flavor basis, the phenomenon of oscillation may occur, that is, the time evolution of an initially pure flavor state (as a neutrino will be produced) will result in a time-dependent probability of measuring the other two flavors as well.

The very small mass of a neutrino relative to its momentum lets one write the relativistic Hamiltonian in terms of mass squared differences $\Delta m_{ij}^2 = m_i^2 - m_j^2$, where $i,j = 1,2,3$, referring to what we then call mass states. The mass basis is really the energy basis with

the small mass approximation, along with dropping some constant terms in the Hamiltonian (which do not affect time evolution).

The mixing between the 3-vector mass and flavor bases is defined by a rotation in terms of three mixing angles, θ_{12} , θ_{23} , and θ_{13} . Transformation between the flavor and mass bases is done with the following unitary matrix, called the Pontecorvo–Maki–Nakagawa–Sakata (PMNS) matrix [6]:

$$(1) \quad U = \begin{pmatrix} 1 & 0 & 0 \\ 0 & c_{23} & s_{23} \\ 0 & -s_{23} & c_{23} \end{pmatrix} \begin{pmatrix} c_{13} & 0 & s_{13}e^{-i\delta} \\ 0 & 1 & 0 \\ -s_{13}e^{i\delta} & 0 & c_{13} \end{pmatrix} \begin{pmatrix} c_{12} & s_{12} & 0 \\ -s_{12} & c_{12} & 0 \\ 0 & 0 & 1 \end{pmatrix} \begin{pmatrix} 1 & 0 & 0 \\ 0 & e^{i\alpha_1/2} & 0 \\ 0 & 0 & e^{i\alpha_2/2} \end{pmatrix}$$

$$= \begin{pmatrix} c_{12}c_{13} & s_{12}c_{13} & s_{13}e^{-i\delta} \\ -s_{12}c_{23} - c_{12}s_{23}s_{13}e^{i\delta} & c_{12}c_{23} - s_{12}s_{23}s_{13}e^{i\delta} & s_{23}c_{13} \\ s_{12}s_{23} - c_{12}c_{23}s_{13}e^{i\delta} & -c_{12}s_{23} - s_{12}c_{23}s_{13}e^{i\delta} & c_{23}c_{13} \end{pmatrix} \begin{pmatrix} 1 & 0 & 0 \\ 0 & e^{i\alpha_1/2} & 0 \\ 0 & 0 & e^{i\alpha_2/2} \end{pmatrix}$$

where $c_{ij} = \cos \theta_{ij}$ and $s_{ij} = \sin \theta_{ij}$. δ and α_i are Dirac and Majorana, respectively, CP-violating phases. Transformation between bases is done by Eq. 2:

$$(2) \quad |\nu_\alpha\rangle = \sum_i U_{\alpha i}^* |\nu_i\rangle, \\ |\nu_i\rangle = \sum_\alpha U_{\alpha i} |\nu_\alpha\rangle.$$

A two-neutrino approximation demonstrates how this results in neutrino oscillation. In this case, there is only one mixing angle θ and one mass squared difference Δ , and the Hamiltonian H and mixing matrix U are as follows:

$$(3) \quad H = \frac{1}{4E} \begin{pmatrix} -\Delta & 0 \\ 0 & \Delta \end{pmatrix}$$

$$U = \begin{pmatrix} \cos \theta & \sin \theta \\ -\sin \theta & \cos \theta \end{pmatrix}.$$

Applying time evolution to a pure electron neutrino state (where the two neutrino flavors here are ν_e and ν_μ) then leads to the following time-dependent state:

$$(4) \quad |\nu(t)\rangle = (e^{it\Delta/4E} \cos^2 \theta + e^{-it\Delta/4E} \sin^2 \theta) |\nu_e\rangle$$

$$+ \cos \theta \sin \theta (-e^{it\Delta/4E} + e^{-it\Delta/4E}) |\nu_\mu\rangle$$

where E is the neutrino energy. Note that if θ is zero, the case where the mass basis is the same as the flavor basis, the state remains pure $|\nu_e\rangle$. The same is true if Δ is zero. Thus, the discovery of neutrino oscillation was the first (and only, so far) demonstration that neutrinos have a non-zero mass.

Studying oscillations of neutrinos from different kinds of sources, with different energies and path lengths, can isolate sensitivities to the different mixing angles and mass squared differences. For example, the study of solar neutrinos (neutrinos emanating from nuclear fusion reactions in the core of the sun) provides sensitivity to θ_{12} and Δm_{12}^2 . The oscillation parameters so far measured are shown in Table 1.1.

TABLE 1.1. Best-fit values for neutrino oscillation parameters, from a global fit to oscillation experiment data. Parameters which depend on the mass hierarchy have values for NH (IH). The atmospheric parameter Δm^2 is defined as $\Delta m^2 = \Delta m_{31}^2 - \Delta m_{21}^2/2 > 0$ ($\Delta m^2 = \Delta m_{32}^2 + \Delta m_{21}^2/2 < 0$). [6]

Parameter	Measurement ($\pm 1\sigma$)
Δm_{12}^2	$7.54^{+0.26}_{-0.22} 10^{-5} \text{ eV}^2$
$ \Delta m^2 $	$2.43 \pm 0.06 (2.38 \pm 0.06) 10^{-3} \text{ eV}^2$
$\sin^2 \theta_{12}$	0.308 ± 0.017
$\sin^2 \theta_{23}$	$4.37^{+0.033}_{-0.023} (4.55^{+0.039}_{-0.031})$
$\sin^2 \theta_{13}$	$0.0234^{+0.0020}_{-0.0019} (0.0240^{+0.0019}_{-0.0022})$
δ/π (2σ range)	$1.39^{+0.38}_{-0.27} (1.31^{+0.29}_{-0.33})$

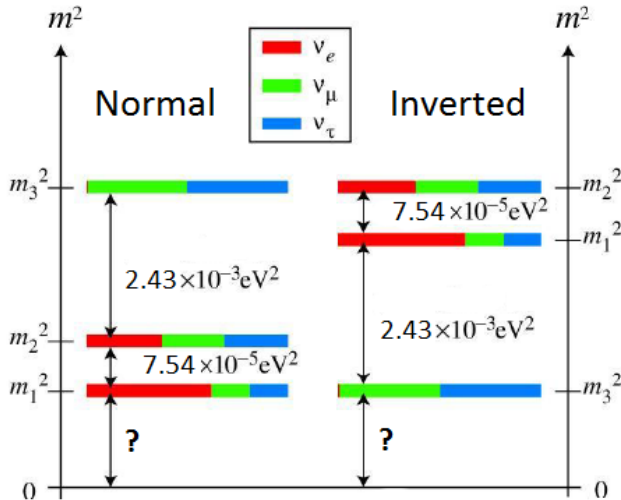


FIGURE 1.1. The two possible hierarchies of neutrino masses. The colors depict the mixing between the mass and flavor bases.

Since only the absolute value of the atmospheric neutrino oscillation parameter Δm^2 is known, there are two possibilities for the hierarchy of the three neutrino masses. These are called the Normal and Inverted Hierarchies, as shown in Fig. 1.1.

The correct mass hierarchy remains unknown, but next-generation neutrino experiments, possibly including nEXO, may be able to discern this.

Neutrino oscillation demonstrates that neutrinos have non-zero mass, and though oscillation experiments measure the mass squared differences, the absolute masses of the three neutrinos remain unknown. Cosmology can put limits on the sum of the three neutrino



FIGURE 1.2. Two-neutrino (left) and neutrinoless (right) double beta decay.

masses. The Planck collaboration reports an upper bound on this sum at $\sum_i m_i < 0.23 \text{ eV}$ [7]. The KATRIN experiment will search for absolute neutrino mass with sensitivity of $m_{\bar{\nu}_e} < 0.2 \text{ eV}$ (90% CL) by measuring the spectrum of tritium beta decay near the Q-value (maximal decay energy) [8].

1.2. DOUBLE BETA DECAY

Double beta decay is the simultaneous decay of two neutrons in a nucleus into two protons and two electrons. Two-neutrino double beta decay ($2\nu\beta\beta$), shown in Fig. 1.2(left), is allowed by the Standard Model and has been observed in eleven isotopes with half-lives between 10^{19} and 10^{21} years. Similar to beta decay, a neutrino accompanies each electron in this decay, broadening the spectrum of the summed electron energy. This is a second-order process, making it a rare decay, and requiring low backgrounds to measure.

Neutrinoless double beta decay, shown in Fig. 1.2(right), is a postulated mode of double beta decay. In this case, the neutrino is exchanged as a virtual particle (which would require that it is its own anti-particle, i.e. a Majorana particle), and there are no neutrinos in the

final products. If discovered, neutrinos be determined to be Majorana particles, and lepton number would be violated. The measured $0\nu\beta\beta$ half-life would also aid in determining absolute neutrino mass according to Eq. 5:

$$(5) \quad T_{1/2}^{0\nu} = (G^{0\nu}(Q, Z)|M^{0\nu}|^2 \langle m_\nu \rangle^2)^{-1}$$

where $T_{1/2}^{0\nu}$ is the $0\nu\beta\beta$ half-life, $G^{0\nu}$ is a known phase space factor, and $M^{0\nu}$ is a model-dependent nuclear matrix element. $\langle m_\nu \rangle$ is the effective Majorana neutrino mass:

$$(6) \quad \langle m_\nu \rangle = \sum_i U_{ei}^2 m_i.$$

The terms U_{ei} contain the measured mixing angles θ_{12} and θ_{13} , as well as the unknown CP-violating phases δ , α_1 , and α_2 .

The sum of the energies of the emitted electrons in double beta decay will serve as the distinction between the two-neutrino and zero-neutrino modes, shown in Fig. 1.3. In the two-neutrino mode, the total decay energy is shared probabilistically between the electrons and the neutrinos (the nuclear recoil energy is negligible), resulting in a broad distribution in the summed electron energy. (Recall the similarly broad electron energy in single beta decay, which ultimately led to discovery of the neutrino involved.) But in the zero-neutrino mode, essentially all of the decay energy is carried away by the two electrons, resulting in essentially a single allowed value for the total electron energy – a peak in the summed electron energy spectrum at the Q-value.

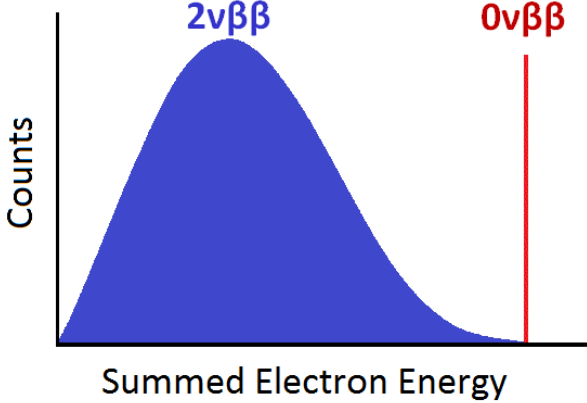


FIGURE 1.3. Conceptual two-neutrino (blue) and zero-neutrino (red) double beta decay spectra.

The rarity of double beta decay requires very low backgrounds, especially around the Q-value for the $0\nu\beta\beta$ search. The next sections describe the experiments EXO-200 and its next-generation successor, nEXO, and how the barium tagging method progressed in this work could be critical in obtaining essentially zero background in the second phase of nEXO operation.

1.3. ENRICHED XENON OBSERVATORY

EXO-200 and nEXO (EXO standing for Enriched Xenon Observatory) are a progression of two experiments, each a liquid xenon (LXe) time projection chamber (TPC) designed to study the double beta decay of the isotope ^{136}Xe , and ultimately to search for the zero-neutrino mode. ^{136}Xe is unique among the double beta decay isotopes in that it can be studied in a gas or liquid TPC instead of solid crystals or foils. The 3D event position reconstruction abilities of a TPC have advantages in background reduction, described in section 1.3.1. Purification of Xe is straightforward and can be done continuously in a detector. LXe is transparent, and produces substantial ionization and scintillation at 178 nm when energy is deposited in the LXe [9]. A liquid TPC approach also offers the opportunity to

identify, or “tag”, the daughter $^{136}\text{Ba}^{++}$ at the site of the double beta decay event, which would provide a method for background-free identification of $0\nu\beta\beta$ [10]. Barium tagging is the focus of our group at CSU and is the subject of this thesis. The following sections describe the EXO-200 experiment, as well as nEXO, the next-generation tonne-scale LXe TPC, which is now in the research and development stage. EXO-200 does not have barium tagging implemented, but it is hoped that nEXO will in the second phase of operation.

1.3.1. EXO-200

Located about half a mile underground in the Waste Isolation Pilot Plant (WIPP) near Carlsbad, NM, EXO-200 has been operational since 2011. It is a TPC using LXe enriched to $80.672 \pm 0.14\%$ ^{136}Xe [9], with a fiducial volume corresponding to 66.20 kg of ^{136}Xe . It is designed to probe Majorana neutrino masses down to around 100 meV [11]. The WIPP mine is in a salt basin, which contains lower levels of Uranium and Thorium than rock in a typical mine.

A schematic diagram of the TPC in the class 100 cleanroom is shown in Fig. 1.4. Several layers of lead wall surround the copper cryostat, which is filled with HFE-7000, a cryogenic fluid which keeps the TPC cooled to LXe temperatures. The HFE also provides shielding for the detector. The TPC vessel is made of low-radioactivity copper, and is kept as thin as possible to minimize backgrounds. Scintillating panels on the outside of the cleanroom provide a cosmic ray muon veto.

A cut-away view of the EXO-200 detector is shown in Fig. 1.5. It is two mirrored TPCs which share a cathode. The detection planes are a combination of ionized charge induction/collection wires and large area avalanche photodiodes (LAAPDs), which detect scintillation light [12].



FIGURE 1.4. Drawing of EXO-200 TPC Vessel with surrounding cryostat, lead walls, and muon veto panels.

A view into one of the TPCs is shown in Fig. 1.7. On the detection plane, holes for the LAAPDs can be seen below the cross-hatched u- and v-wires. The white material on the inner wall is the Teflon reflector. When a double beta decay event occurs in the LXe, the energetic electrons ionize many surrounding Xe atoms, as well as produce a scintillation signal.

The cathode is set to -8 kV, providing an electric field of 374 V/cm across the 20 cm drift length of each TPC. Ionized electrons drift from the decay site, first passing the v-wires, which receive an induction signal as depicted in Fig. 1.8, and are then collected by the u-wires, which are set at a 60° angle from the v-wires. An electric field of 778 V/cm between the u- and v-wires ensures 100% v-wire transparency. The charge collection provides an energy measurement. Together, the u- and v-wires give an x/y position measurement for



FIGURE 1.5. EXO-200 TPC cutaway view [9].

the event. The time between the initial scintillation detection and the charge collection give a z position. Thus a 3D position can be reconstructed for the event if u-wire, v-wire, and scintillation signals are detected. [9]

A well-known microscopic anti-correlation between ionization and scintillation signals in LXe [13] is exploited in EXO-200 to improve the energy resolution. Energies measured by ionization and scintillation of events produced by the ^{228}Th gamma source, one of the sources used to calibrate the EXO-200 detector, are plotted in Fig. 1.6. The tilt of the full

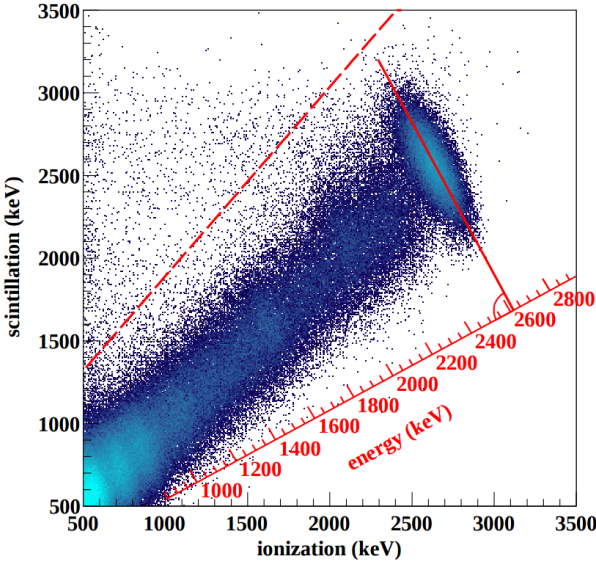


FIGURE 1.6. Anti-correlation between ionization and scintillation in events from the ^{228}Th calibration source in EXO-200. The dashed red line defines a cut on non-reconstructed events. [14]

absorption ellipse of the 2615 keV gamma line demonstrates the anti-correlation. A “rotated energy” is defined according to this tilt in order to optimize energy resolution.

Having a reconstructed 3D event position is important in several ways. Firstly, position-based corrections to scintillation and charge collection can be applied. For charge, electronegative impurities in the LXe will absorb the drifting charge, requiring a drift-length (z-position) correction. High purity levels, measured in terms of electron lifetime, of 2-5ms and higher are maintained in EXO-200, resulting in a correction of a few % for maximal drift lengths. For scintillation, a 3D correction is applied, as some regions have more efficient light collection by the LAAPDs. A 3D position also allows a fiducial volume to be defined. A standoff distance from detector surfaces aids in distinction between gamma ray events and double beta decay events. Gamma backgrounds, which mostly come from detector materials, exhibit some attenuation in the LXe. Double beta decay events are uniformly distributed in the LXe. Finally, 3D reconstruction allows the distinction between single-site (SS) and

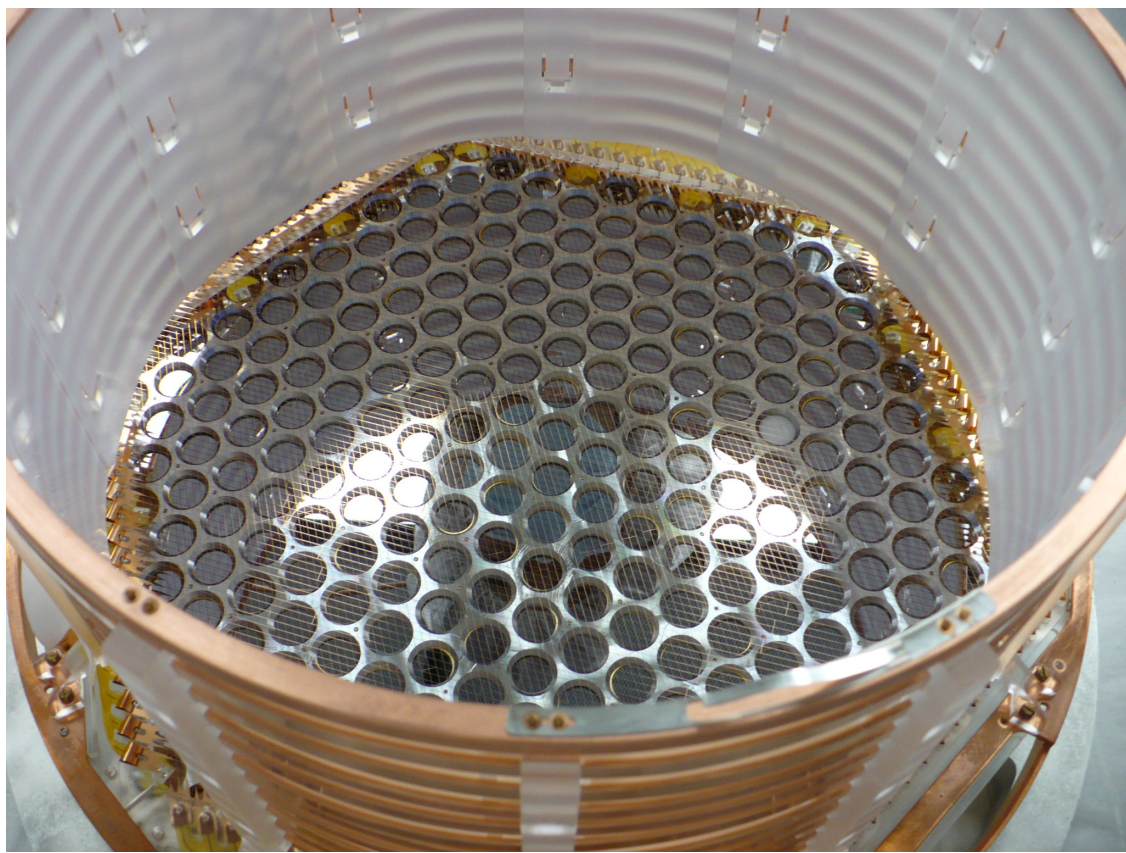


FIGURE 1.7. View of the detection plane in one of the two EXO-200 TPCs.

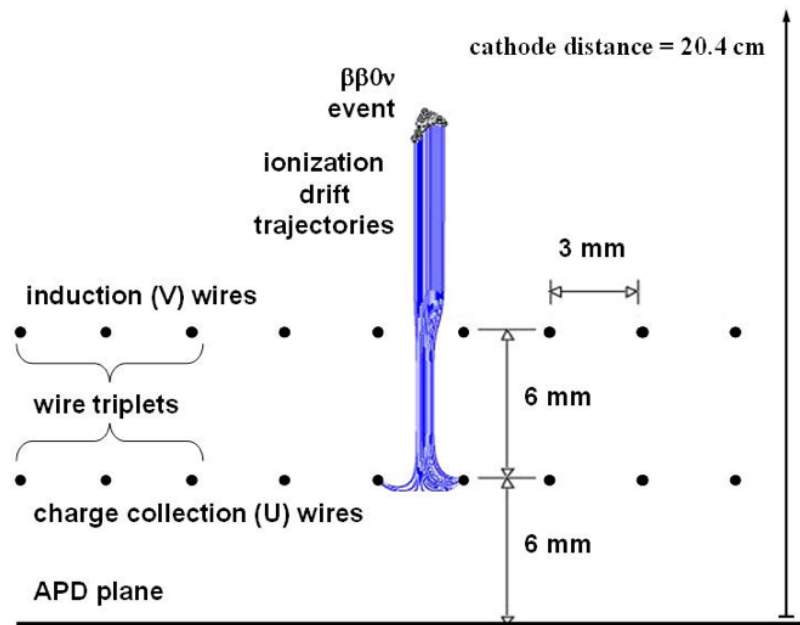


FIGURE 1.8. EXO-200 event topology.

multi-site (MS) events. A MS event is one where two spatially separated events occur in the same $2048\text{-}\mu\text{s}$ time window. These are mostly caused by gamma events, which can Compton-scatter several times in the LXe. Rejecting MS events further aids in separating gamma events from double beta decay events. [9] Barium tagging will also benefit from a 3D reconstructed position in nEXO.

The final data set is fit using a combination of probability distribution functions (PDFs) for $0\nu\beta\beta$, $2\nu\beta\beta$, and background components. Fits to the final energy spectrum data for (a) SS events, and (b) MS events are shown in Fig. 1.9 for the most recent $0\nu\beta\beta$ analysis. The green bands beneath each plot show the residuals vs. energy. The $2\nu\beta\beta$ spectrum, in gray, dominates the signal in the SS spectrum below the Q-value. The vertical red lines in the SS spectrum outline the $\pm 2\sigma$ region of interest around the Q-value, where the $0\nu\beta\beta$ peak will lie. The insets are a zoom into this region. The best fit value for $0\nu\beta\beta$ in this dataset is non-zero, but it is consistent with the null hypothesis at 1.2σ . This sets an upper limit on the $0\nu\beta\beta$ half-life at $T_{1/2}^{0\nu\beta\beta} < 1.1 \times 10^{25}$ yr (90% CL), which corresponds to $\langle m_{\nu_e} \rangle < 190$ -450 meV depending on nuclear matrix element calculations [15]. EXO-200 reports the $2\nu\beta\beta$ half-life measurement in [9] of $T_{1/2}^{2\nu\beta\beta} = 2.165 \pm 0.016(\text{stat}) \pm 0.059(\text{sys}) \times 10^{21}$ yr. This is the most precise $2\nu\beta\beta$ measurement to date and is consistent with previous measurements by EXO-200 in 2011 [16] and KamLAND-ZEN in 2012 [17].

1.3.2. nEXO

The next-generation successor to EXO-200 is nEXO, a ~ 5 ton LXe TPC which will probe Majorana neutrino masses down to the 10 meV scale. A schematic diagram of the nEXO detector in the SNOLAB cryopit, one of the possible locations for nEXO, is shown in Fig. 1.10. Similar to EXO-200, the copper-housed TPC will be submerged in HFE fluid, inside

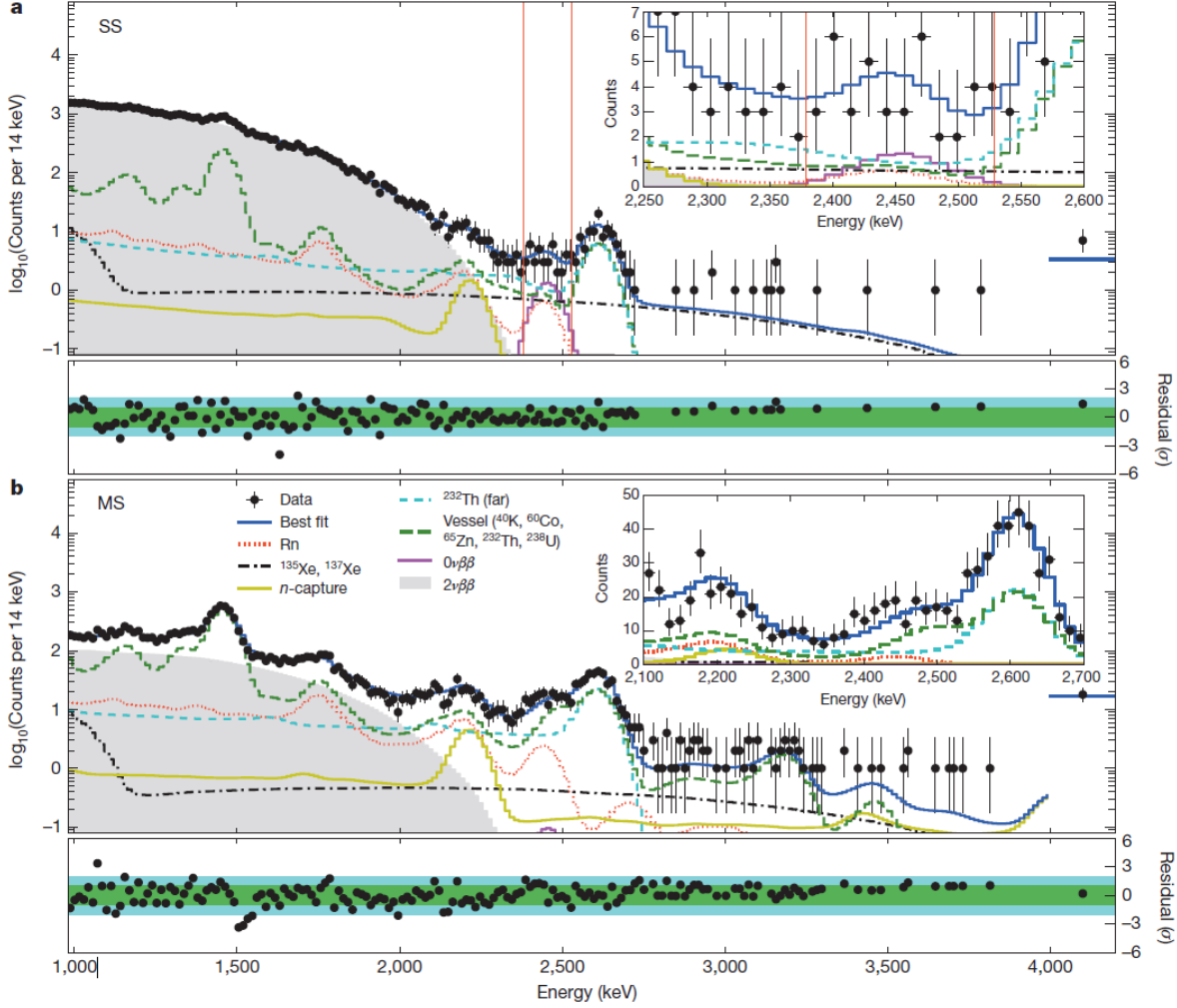


FIGURE 1.9. EXO-200 energy spectrum of events from the latest $0\nu\beta\beta$ search analysis. The insets $2\nu\beta\beta$ end point. [15]

a copper cryostat. The cryostat will be insulated and submerged in a large volume of water shielding, in which photo-multiplier tubes will provide muon veto by observing Cherenkov radiation. nEXO will be a single TPC. Rather than wires, nEXO will use tile electrodes for charge readout, shown in Fig. 1.11. Silicon photo-multipliers on the sides of the detector will be used for light detection.

The sensitivity projections for nEXO are shown in Fig. 1.12, along with those of EXO-200. nEXO will reach the non-degenerate region where the two possible mass hierarchies split, and will probe the full inverted hierarchy. The addition of barium tagging would be a



FIGURE 1.10. nEXO TPC in the SNOLAB cryopit.



FIGURE 1.11. nEXO readout.

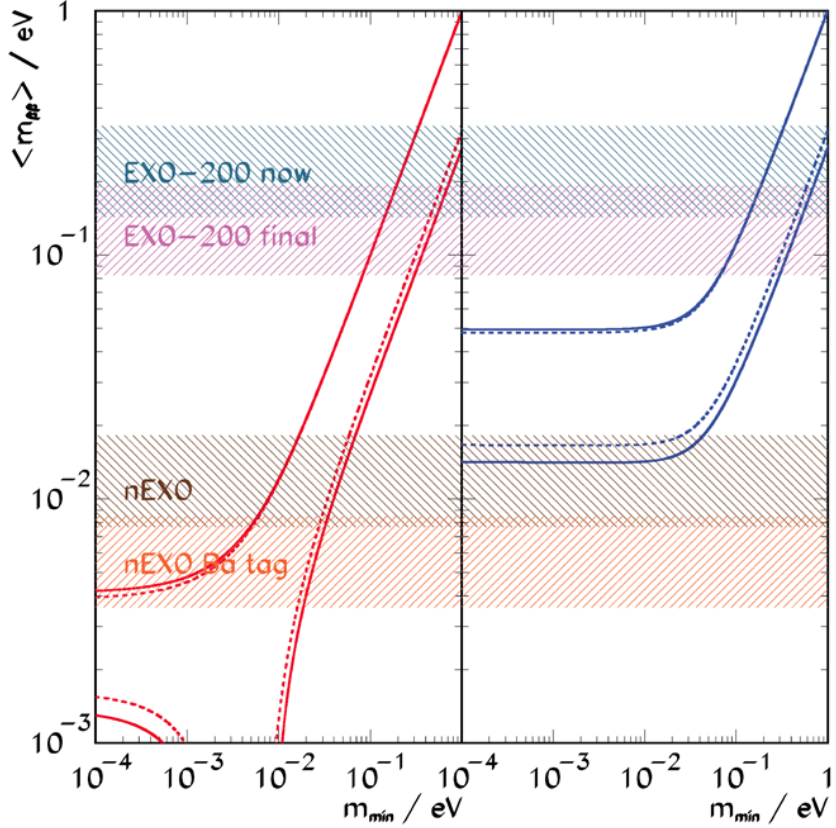


FIGURE 1.12. nEXO projected sensitivity to the Majorana neutrino mass vs. the minimum of the three masses m_{\min} . Dotted (solid) lines are 1(2)- σ bands on measured neutrino oscillation parameters.

very significant advance, as it would push the mass sensitivity down into the region allowed only by the normal hierarchy.

1.3.3. BARIUM TAGGING

The ability to observe the daughter of each $0\nu\beta\beta$ event is the ultimate background rejection technique. No background events generate a Ba daughter except $2\nu\beta\beta$ of ^{136}Xe [10]. Several possible barium tagging techniques have been proposed for nEXO. The original and most natural concept is to direct one or more lasers at the decay site to induce fluorescence of the barium daughter. This technique was explored by our group, and has been abandoned for now because Ba $^+$ fluorescence was not unambiguously identified in LXe [18].

A few barium tagging techniques continue to be explored. One of these is to grab the daughter on a probe surface, brought to the decay site by a probe. It would then be moved to a location where it can be desorbed from that surface by an infrared laser, and subsequently resonantly ionized by two lasers in order to detect it by time-of-flight spectroscopy. The apparatus for the study of this method is described in [19], along with some initial results.

The other leading technique for barium tagging in LXe, now the focus of our group and the subject of this thesis, is barium tagging in SXe. In this method, a cold probe would be inserted to the site of the candidate $0\nu\beta\beta$ event, and additional cooling would be applied to trap the Ba or Ba⁺ daughter in a small amount of SXe. The single Ba/Ba⁺ would be observed by laser-induced fluorescence in the SXe, a technique more generally called matrix isolation spectroscopy. A concept for a probe is shown in Fig. 1.13. The SXe layer is formed on a sapphire window at the end of the probe. Sapphire is a good candidate for a substrate because it has good thermal conductivity at low temperature and is highly transparent. An excitation laser may be brought into the probe through a fiber, and scanned across the sapphire to excite the Ba/Ba⁺ in the SXe. A return fiber could collect the laser reflections to measure the SXe thickness via interference fringes. The Ba/Ba⁺ fluorescence would then be collected by a lens/filter system and imaged onto a CCD. Additional components, not shown, would be required for cooling the sapphire, either by liquid He or by a Joule-Thompson nozzle.

Whether the daughter Ba will neutralize or remain ionized in SXe is not yet known. It is, however, expected that a Ba⁺⁺ daughter of $0\nu\beta\beta$ will neutralize rapidly to Ba⁺ by charge transfer in LXe, since the LXe conduction band gap is slightly less than the ionization potential for Ba⁺ [10]. Further neutralization by recombination with the electron cloud

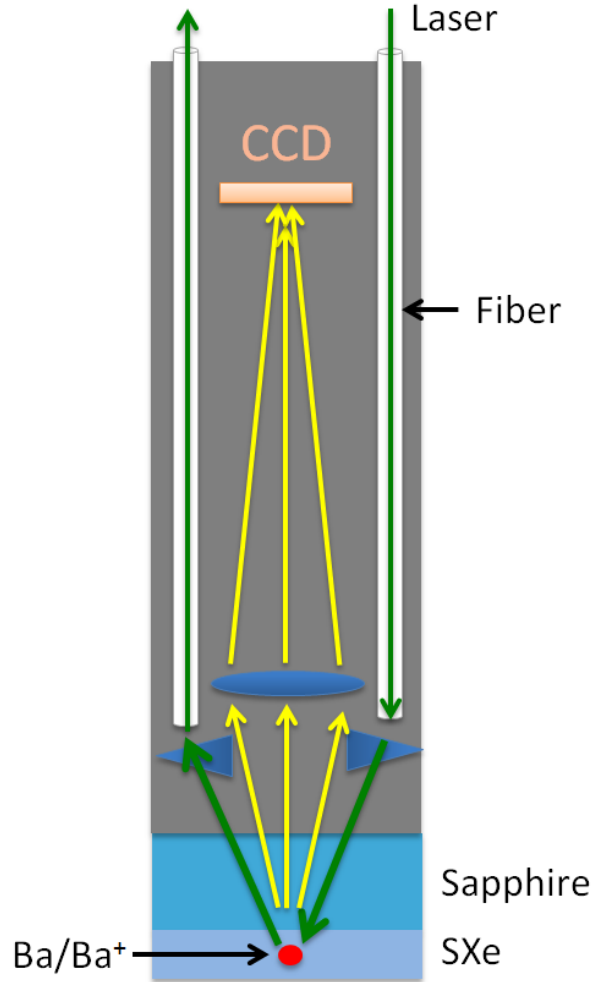


FIGURE 1.13. Concept for a cryoprobe containing excitation/collection optics.

could also occur. However, a study of neutralization of ^{214}Bi daughters of ^{214}Pb beta decay in EXO-200 has observed a high percentage, 76(5)%, of ionized daughters, and negligible subsequent neutralization in many minutes [21]. This provides an expectation of a high percentage of ionized ^{136}Ba daughters of $0\nu\beta\beta$.

CHAPTER 2

THEORY

Need into paragraph?

Needs cross section calc. like Shon now.

2.1. BA/BA⁺ SPECTROSCOPY IN VACUUM

Some of the low-lying energy levels for Ba in vacuum are shown in Fig. 2.1. The main transition is between the ground $6s^2 \ ^1S_0$ state to the excited $6s6p \ ^1P_1^o$ state. Branching ratios from the $^1P_1^o$ state result in a decay to one of three metastable D states in about 1 in 330 excitations. Decays back to ground from the D states are parity-forbidden, resulting in very low decay rates of around 4 s^{-1} for the 1D_2 state, and around 0.01 s^{-1} for the 3D states. Transition rates for the lowest-lying Ba energy levels in vacuum are shown in Table 2.1.

The low-lying energy levels of Ba⁺ in vacuum are shown in Fig. 2.2. Two strong transitions exist between the ground $6s \ ^2S_{1/2}$ state and the $6p \ ^2P_{1/2}$ and $6p \ ^2P_{3/2}$ excited states. Branching ratios to the two metastable 2D states result in a decay into a 2D state after about 4 excitations. Transition rates between these levels are listed in Table 2.1.

Single atom/ion detection by spectroscopy requires many excitation/emission cycles in order to detect an observable number of photons from a single atom/ion. For Ba/Ba⁺, in addition to the main excitation laser, lasers may be needed to depopulate the metastable D states once the atom/ion becomes optically pumped into one of them. This recovery is called re-pumping. In Ba, re-pumping can be accomplished via three infrared lasers at wavelengths 1107.6 nm, 1130.0 nm, and 1500.0 nm for the direct transitions back to the

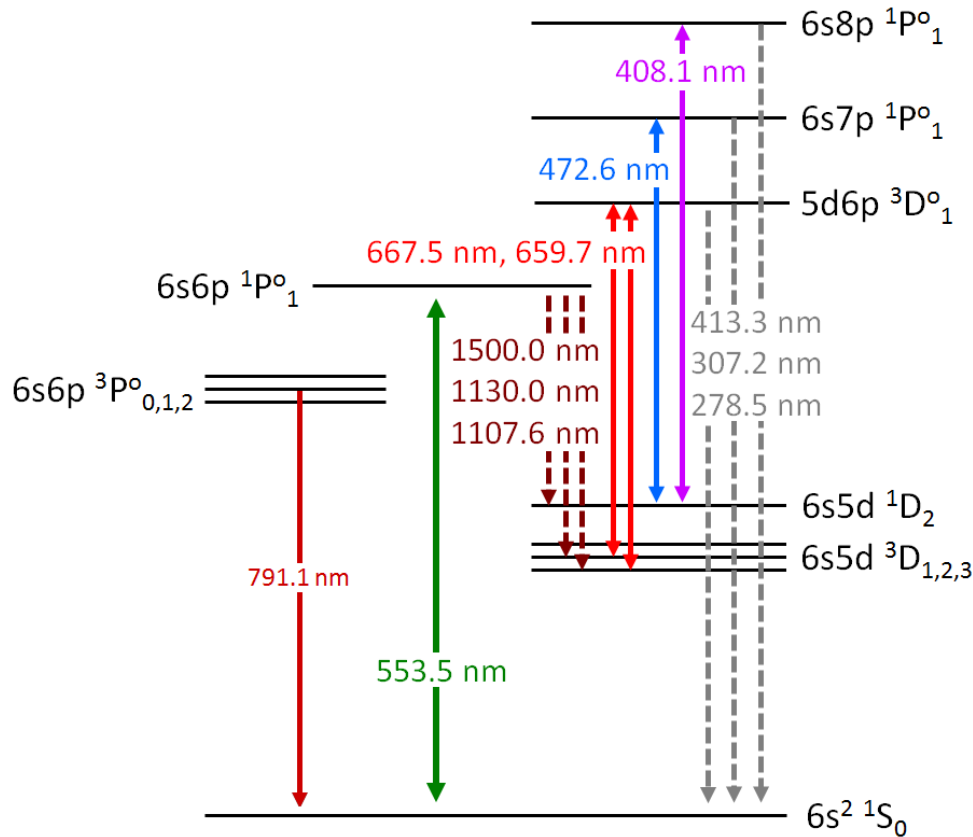


FIGURE 2.1. Ba energy levels in vacuum.

TABLE 2.1. Transition rates for the lowest-lying energy levels of Ba and Ba⁺ in vacuum.

	Transition	Rate (s^{-1})	[Reference]
Ba	$6s6p \ ^1P_1^o \rightarrow 6s^2 \ ^1S_0$	1.19×10^8	[22]
	$6s6p \ ^1P_1^o \rightarrow 6s5d \ ^1D_2$	2.50×10^5	[22]
	$6s6p \ ^1P_1^o \rightarrow 6s5d \ ^3D_2$	1.1×10^5	[22]
	$6s6p \ ^1P_1^o \rightarrow 6s5d \ ^3D_1$	3.1×10^3	[22]
	$6s5d \ ^1D_2 \rightarrow 6s^2 \ ^1S_0$	4	[23]
	$6s5d \ ^3D_2 \rightarrow 6s^2 \ ^1S_0$	1.45^{-2}	[24]
	$6s5d \ ^3D_1 \rightarrow 6s^2 \ ^1S_0$	1.7^{-2}	[23]
Ba ⁺	$6p \ ^2P_{3/2}^o \rightarrow 6s \ ^2S_{1/2}$	1.11×10^8	[22]
	$6p \ ^2P_{1/2}^o \rightarrow 6s \ ^2S_{1/2}$	9.53×10^7	[22]
	$6p \ ^2P_{3/2}^o \rightarrow 5d \ ^2D_{5/2}$	4.12×10^7	[22]
	$6p \ ^2P_{3/2}^o \rightarrow 5d \ ^2D_{3/2}$	6.00×10^6	[22]
	$6p \ ^2P_{1/2}^o \rightarrow 5d \ ^2D_{3/2}$	3.10×10^7	[22]
	$5d \ ^2D_{5/2} \rightarrow 6s \ ^2S_{1/2}$	3.8×10^{-2}	[25]
	$5d \ ^2D_{3/2} \rightarrow 6s \ ^2S_{1/2}$	1.3×10^{-2}	[26]

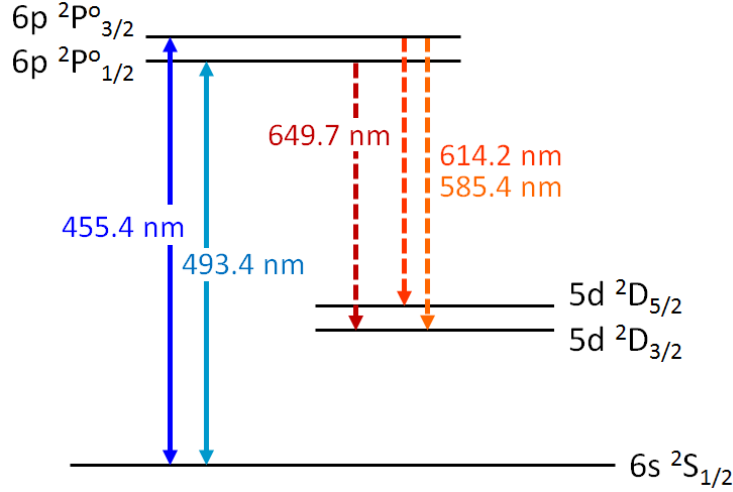


FIGURE 2.2. Ba^+ energy levels in vacuum.

$6s6p\ ^1P_1^o$ state. An alternative re-pumping scheme is via excitation to higher-level states which have paths back to the ground state or the $6s6p\ ^1P_1^o$ state. A few such higher-level re-pump transitions are shown in Fig. 2.1, including two red transitions to the $5d6p\ ^3D_1^o$, and blue and violet transitions to the $6s7p\ ^1P_1^o$ and $6s8p\ ^1P_1^o$ states. Trapping/detection of Ba atoms in a magneto-optical trap (MOT) was achieved in [27]. This was done with two separate re-pumping schemes: by incorporating three infrared re-pump transitions, as well as with two infrared re-pump transitions along with a 659.7-nm laser re-pumping the $6s5d\ ^3D_1$ state via the $5d6p\ ^3D_1^o$ state. Observation of trapped single Ba^+ ions in vacuum has been achieved using 493.4 nm along with one re-pump laser at 649.7 nm [28, 29].

2.2. 5-LEVEL SYSTEM

The model for Ba transitions in vacuum with excitation to the $6s6p\ ^1P_1^o$ state is a 5-level system, shown schematically in Fig. 2.3. States 1 and 2 represent the $6s^2\ ^1S_0$ and $6s6p\ ^1P_1^o$ states, respectively, and states 3, 4 and 5 represent the $6s5d\ ^1D_2$, $6s5d\ ^3D_2$, and $6s5d\ ^3D_1$

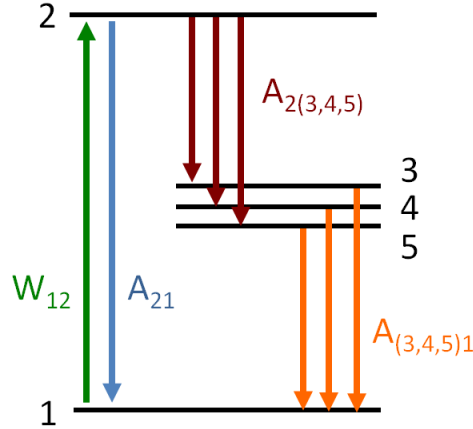


FIGURE 2.3. 5-level system diagram with excitation rate W_{12} and decay rates A_{ij} .

states, respectively. The rate equations for this system, neglecting stimulated emission, are given in Eq. 7:

$$\begin{aligned}
 \frac{dN_1}{dt} &= -W_{12}N_1 + A_{21}N_2 + A_{31}N_3 + A_{41}N_4 + A_{51}N_5 \\
 \frac{dN_2}{dt} &= W_{12}N_1 - N_2(A_{21} + A_{23} + A_{24} + A_{25}) \\
 (7) \quad \frac{dN_3}{dt} &= A_{23}N_2 - A_{31}N_3 \\
 \frac{dN_4}{dt} &= A_{24}N_2 - A_{41}N_4 \\
 \frac{dN_5}{dt} &= A_{25}N_2 - A_{51}N_5
 \end{aligned}$$

where N_i is the population in state i , A_{ij} is the decay rate from state i to state j , and W_{12} is the excitation rate.

Under some experimental conditions, the assumption can be made that W_{12} is small compared to the rates out of the ${}^1\text{P}_1{}^\circ$ state. In this case the population in the excited state N_2 is negligible. For these conditions, there is an effective pumping rate for the D states:

$$(8) \quad W_{1i} = W_{12} \frac{A_{2i}}{A_{21} + A_{23} + A_{24} + A_{25}}$$

where $i = 3, 4, 5$. Eq. 8 is also true for $i = 1$, where W_{11} represents the fluorescence rate. The fraction in Eq. 8 is the respective branching ratio from the excited state. With this definition, the rate equations for states 3, 4, and 5 can be re-written as:

$$(9) \quad \begin{aligned} \frac{dN_3}{dt} &= W_{13}N_1 - A_{31}N_3 \\ \frac{dN_4}{dt} &= W_{14}N_1 - A_{41}N_4 \\ \frac{dN_5}{dt} &= W_{15}N_1 - A_{51}N_5 \end{aligned}$$

where $N_1 = 1 - N_3 - N_4 - N_5$ by conservation of total population. For a numerical solution of these equations, initially all population is in the ground state ($N_3 = N_4 = N_5 = 0$). The model calculates the state populations N_i at the end of each iterative time step, t_{step} , as:

$$(10) \quad N_i = N_{i,\text{previous}} + \frac{dN_i}{dt}t_{\text{step}}$$

where $i = 3, 4, 5$, and dN_i/dt is determined at the beginning of each time step according to Eq. 9. Time steps of $t_{\text{step}} = 1 \mu\text{s}$ were used. In order to model data, which is taken in exposure time (t_{exp}) frames, the model iterates through $t_{\text{exp}}/t_{\text{step}}$ steps in each frame, accumulating fluorescence photons emitted at each step (ΔS_{step}) according to the fluorescence rate $N_1 W_{11}$ times t_{step} , amounting to:

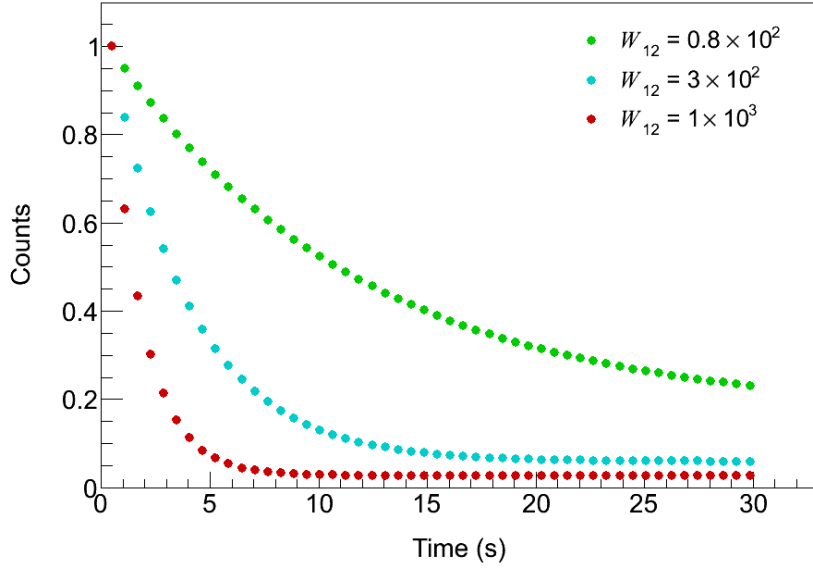


FIGURE 2.4. Modeled photons emitted in 0.5-s exposure frames for three values of W_{12} , using vacuum Ba transition rates, normalized to the first point. A readout time of 0.1 s is used between frames.

$$(11) \quad \Delta S_{\text{step}} = W_{12} \frac{A_{21} N_1}{A_{21} + A_{23} + A_{24} + A_{25}} t_{\text{step}}$$

To incorporate camera readout time, where laser exposure continues but fluorescence is not observed, populations and derivatives are iterated without adding to total counts.

Examples of modeled normalized photons emitted vs. time are shown in Fig. 2.4 for three values of W_{12} , using the transition rates of Ba in vacuum from Table 2.1. Decay of fluorescence occurs as atoms are optically pumped into the metastable D states. For long times the curves reach a steady state value. This model is compared to bleaching data of Ba in SXe in Sec. 5.4.1.

2.3. MATRIX ISOLATION SPECTROSCOPY

In the matrix isolation technique, a species of interest is trapped in a crystal, or “matrix,” of inert atoms/molecules such that it can be studied at leisure without guest-guest interactions. To be effective, the temperature must be low enough to prevent diffusion of guest atoms, and the guest concentration must be low enough to prevent interaction. The technique was originally proposed and demonstrated in [30], where short-lived species in chemical reactions were studied by isolating them in various solid matrices. The proposed method of Ba tagging in SXe is a unique application of matrix isolation spectroscopy. In order to understand the spectroscopic effects which may be encountered due to interaction between the guest Ba/Ba⁺ and the host Xe atoms, some effects encountered in systems of metal atoms in rare-gas matrices are discussed.

The leading interaction between a guest atom and the host noble gas atoms is an induced dipole-dipole Van der Waals force. For a metal atom of group I or II, this interaction is quite different when the atom is in the excited P state vs. the ground S state, resulting in general in different shaped potential energy curves [31]. As an approximation to these curves, the ground state potential for a BaXe molecule and a guess at the excited state potential is shown in Fig. 2.5. In a cold matrix, the system will be mainly in the ground lattice vibrational state ($\nu = 0$) before excitation. According to the Franck-Condon principle, the strongest electronic excitation will occur to vibrational states whose wavefunctions overlap that of the ground state. Because this occurs for a band of vibrations, the absorption is broadened. The peak absorption energy is determined by the difference in potential energy between the ground and excited states, which in general is not the same as the absorption energy in vacuum. In the excited state, rapid decay occurs to the lowest vibrational mode, and then

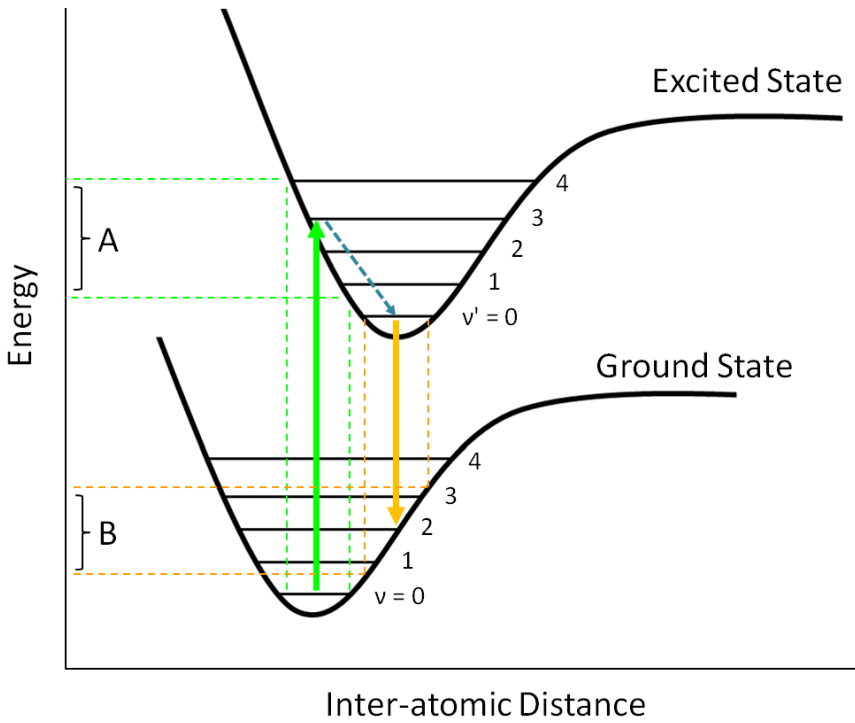


FIGURE 2.5. Illustration of the Franck-Condon Principle resulting in redshifted emission as well as broadening in absorption (A) and emission (B) due to vibrational modes ν (ν') in the ground (excited) state.

a similar broadening in the spontaneous emission energy occurs. A redshift in the emission is observed relative to the excitation. Additionally, splitting of orbital degeneracy in the P state can produce triplet structures in the absorption according to the Jahn-Teller effect [32]. These features depend on the specific configuration of atoms surrounding the guest, and thus different spectra can be observed from guest atoms occupying different matrix “sites.” Annealing a matrix after deposition can reveal relative stability of various matrix sites [31].

As an example, the spectroscopy on Na atoms in solid rare-gas matrices was studied in [33]. Spectral features are exemplified in Fig. 2.6 for Na atoms in SAr, SKr, and SXe. Excitation and emission are broadened to 10s of nm. Two or three different matrix sites are observed in the three matrices, with the largest red-shift in emission observed in SXe. The triplet structures in excitation spectra are attributed to the Jahn-Teller effect. The specific

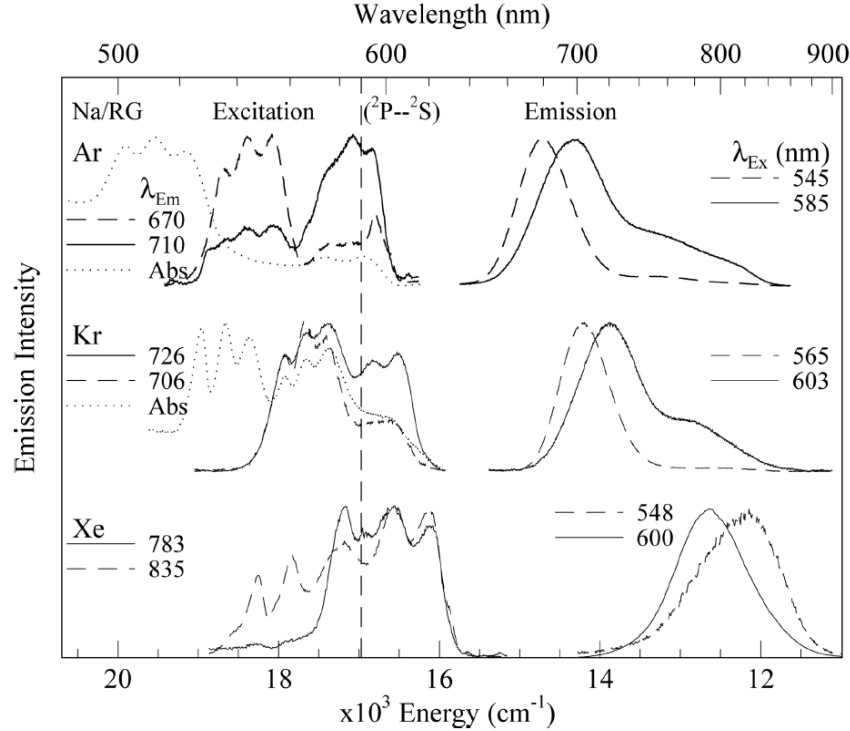


FIGURE 2.6. Excitation and emission spectra of Na atoms in SAr, SKr, and SXe. [33]

matrix configuration associated with each excitation triplet is identified in this paper through theoretical modeling of the Na-matrix interactions.

2.4. FLUORESCENCE EFFICIENCY

Fluorescence efficiency (ϵ_f) is the ratio of total fluorescence photons emitted to photons absorbed. This can be calculated by Eq. 12:

$$(12) \quad \epsilon_f = \frac{f}{W_{12}\epsilon_c}$$

where f is the number of fluorescence photons observed per atom per second, W_{12} is the excitation rate, and ϵ_c is the collection efficiency of the system. W_{12} can be calculated by Eq. 13:

$$(13) \quad W_{12} = \frac{\sigma I}{h\nu}$$

where σ is the cross section for the excitation interaction, I is the laser intensity, and $h\nu$ is the excitation photon energy.

The cross section can be calculated using the shape of an excitation spectrum according to Eq. 14:

$$(14) \quad \sigma(\nu) = A_{21} \frac{g_2}{g_1} \frac{c^2}{8\pi\nu^2} g(\nu)$$

where A_{21} is the atomic transition rate, g_1 and g_2 are the ground and excited state degeneracies, respectively, and ν is the photon frequency. $g(\nu)$ is the normalized line shape, satisfying:

$$(15) \quad \int_0^\infty g(\nu) d\nu = 1$$

Integrating Eq. 14 then yields:

$$(16) \quad \int_0^\infty \sigma(\nu) \nu^2 d\nu = A_{21} \frac{g_2}{g_1} \frac{c^2}{8\pi}$$

Since the cross section is proportional to the excitation spectrum $E(\nu)$, we can finally write the cross section as a function of ν according to Eq. 17:

$$(17) \quad \sigma(\nu) = \frac{A_{21} E(\nu)}{\int_0^\infty E(\nu') \nu'^2 d\nu'} \frac{g_2}{g_1} \frac{c^2}{8\pi}.$$

CHAPTER 3

EXPERIMENTAL

This chapter describes the apparatus at Colorado State University that was used for producing and observing deposits of Ba and Ba⁺ in SXe. The main barium source, a Ba⁺ ion beam, is first described in Sec. 3.1, and then a neutral Ba getter source is discussed in Sec. 3.2. The co-deposit of Ba or Ba⁺ with Xe gas onto a cold sapphire window is described in Sec. 3.3. The technique for focusing the laser into the SXe is described in Sec. 3.4, and imaging of the laser region is described in Sec. 3.5, with attention to the effect of vibrations in Sec. 3.7. Finally, a system for scanning the focused laser across the sapphire window is described in Sec. 3.8.

3.1. ION BEAM

The Colutron ion beam system is a clean mass-selected source of Ba⁺ which, with the added capability of pulsing, can do a very wide range of deposit sizes, from billions of ions in a focused laser region all the way down to the single-ion level and below. The different components of this system are shown in Fig. 3.1 and described in the following subsections. Ions produced in a Colutron ion source receptacle are accelerated and collimated for passage through the mass filter. Several sets of deflection plates are available for steering, and Einzel lenses focus the beam near the final Faraday cup. A set of pulsing plates can be used to deposit 1- μ s, or continuous ion current can be used in depositing in SXe on the cold sapphire window.

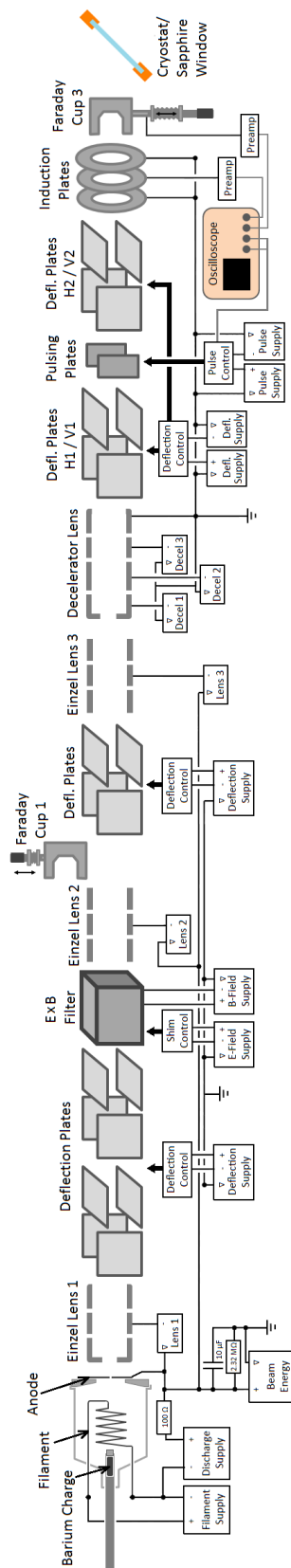


FIGURE 3.1. Ba^+ ion beam.

3.1.1. ION SOURCE

Ba^+ ions are produced in the source of a Model DCIS-101 Colutron ion gun [35]. It is shown in Fig. 3.2. A solid Ba charge is placed into the hollowed end of a stainless steel rod, which is capped by a loose screw. The source rod is inserted into the discharge chamber, where it is heated by a filament, vaporizing the Ba. The source is designed to produce a discharge between the anode plate and the filament cathode, through an argon buffer gas leaked into the source chamber. This controlled discharge also ionizes Ba atoms from the solid charge to produce the desired Ba^+ ion beam, and the Ar^+ ions are filtered out. In the present work, to avoid contamination of the SXe matrix with residual Ar gas, the buffer gas was not used. It has been found that, with care, the discharge can be maintained with Ba vapor alone. The longevity of ion current from a single charge is at least several 10s of hours. This suggests that Ba is coating the inner walls of the source chamber, and is heated enough to provide sufficient Ba pressure to support a discharge.

The discharge produces a plasma, containing barium ions. The application of an acceleration potential draws Ba^+ ions from the plasma. The 2 kV acceleration potential is applied between the ion source anode and the first element of Einzel lens 1 (L1). The potential of this lens is adjusted to collimate the ion beam for passage through the $E \times B$ velocity filter.

3.1.2. $E \times B$ VELOCITY FILTER

The $E \times B$ velocity filter selects Ba^+ by creating perpendicular electric and magnetic fields, which produce opposing forces on charged particles moving through the filter. The opposing forces will be equal for ions with velocity $v = \frac{E}{B}$. Since ion velocity is determined by mass (m), charge (q) and beam potential (V), the filter selects ions satisfying Eq. 18:

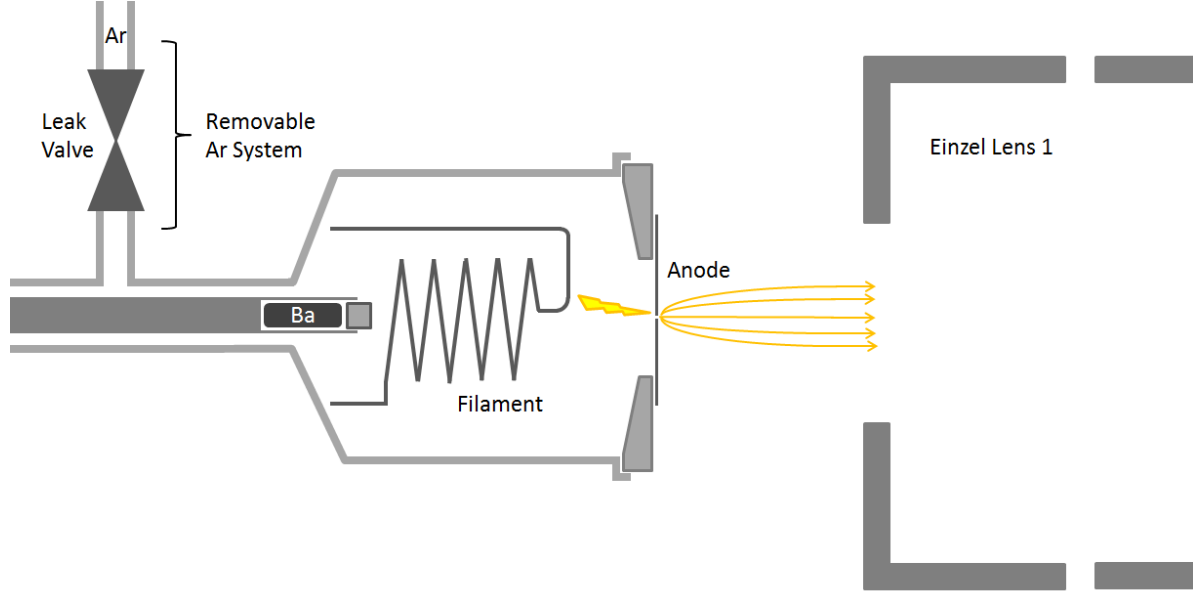


FIGURE 3.2. Ba^+ / Ar^+ ion source.

$$(18) \quad \frac{m}{q} = \frac{2VB^2}{E^2}$$

where B and E are the magnetic and electric fields, respectively. Those fields are chosen such that Ba^+ ions pass straight through. Other ions will be deflected.

The $E \times B$ filter is shown in Fig. 3.3. Electromagnets provide a vertical magnetic field. Electrode plates and field-shaping guard rings provide a horizontal electric field. The guard rings prevent lensing and astigmatism from fringe fields of the plates [35].

3.1.3. OTHER BEAM COMPONENTS

The first three sets of deflection plates shown in Fig. 3.1 can be used for beam diagnostics, and are set to 0 V during normal operation. The fourth set of deflection plates, H1 and V1, located just before the pulsing plates are set to constant values of +50 V and 0 V,

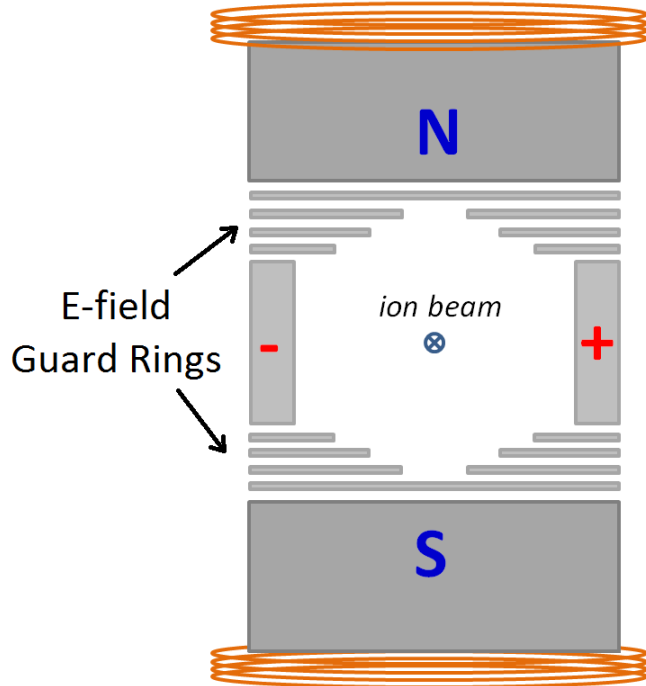


FIGURE 3.3. Colutron $E \times B$ ion velocity filter.

respectively. These voltages have been selected such that the beam, in both pulsing and continuous modes, can be deposited at the sapphire window for reasonable settings on the final deflection plates, H2 and V2. As described in Section 3.1.5, different settings in H2/V2 are required for peak ion current in Faraday cup 3 vs. peak deposit at the window.

Einzel lens 2 (L2) focuses the beam to pass through the aperture in the first element of the decelerator lens. Einzel lens 3 (L3) is set to zero in this setup. The decelerator lens can be used to vary Ba^+ deposit energy, which was done in [36], but in this work it acts as an Einzel lens with only the second element (D2) at non-zero voltage. It focuses the beam near the sample and Faraday cup 3 (there is no Faraday cup 2 in this setup).

Faraday cup 3 measures the ion current during experiments, and is retracted when deposits are being made. Calibration of deposits using Faraday cup 3 is described in Section

3.1.5. Faraday cup 1 can be used for beam diagnostics, and is usually retracted. An additional Faraday cup, cup W, can be attached to the coldfinger in place of the sapphire window for determining deflection plate voltages for depositing Ba^+ on the sapphire window, and for calibrating ion deposits. This is described further in Sec. 3.1.5.

To align the ion beam, L1 was first tuned to maximize ion current in Faraday cup 3, with L2, L3, and D2 set to zero. Since cup 3 is about 2 m away from L1, this approximately collimates the beam for passage through the $E \times B$ filter. The optimal value for L1 was found to be around -400 V relative to the 2000 V beam energy. Next, L2 and D2 were fine-tuned together to achieve maximal current in cup 3. Finally, the straightness of the beam was checked by peaking ion current with deflection plates H1 and V1 on cup 3 and cup W.

3.1.4. ION BEAM PULSING

To deposit small numbers of ions, it is desirable to be able to pulse the ion beam with short pulses. To achieve pulsed beams, the pulsing plates, normally set to 200 V and -200 V to deflect the beam, are pulsed to 0 V for 1 μs to pass a short pulse of ions straight forward. The pulsing circuit is shown in Fig. 3.4. Square waves, triggered by LabVIEW at 500 Hz, enter the circuit at (a). A transformer isolates a MOSFET switch from ground. Upon a trigger pulse the MOSFET switch shorts the pulsing plates for the period of the pulse.

The pulsing plates are followed by three induction plates, the middle plate of which provides a measure of the ion pulses. Just prior to a deposit, the charge in the pulses can be directly measured on cup 3. eV Products pre-amplifiers convert the ion current in the induction plates and cup 3 (or cup W) to voltage signals, which are recorded on a digital oscilloscope. An example of raw oscilloscope traces of Faraday cup 3 and induction plate

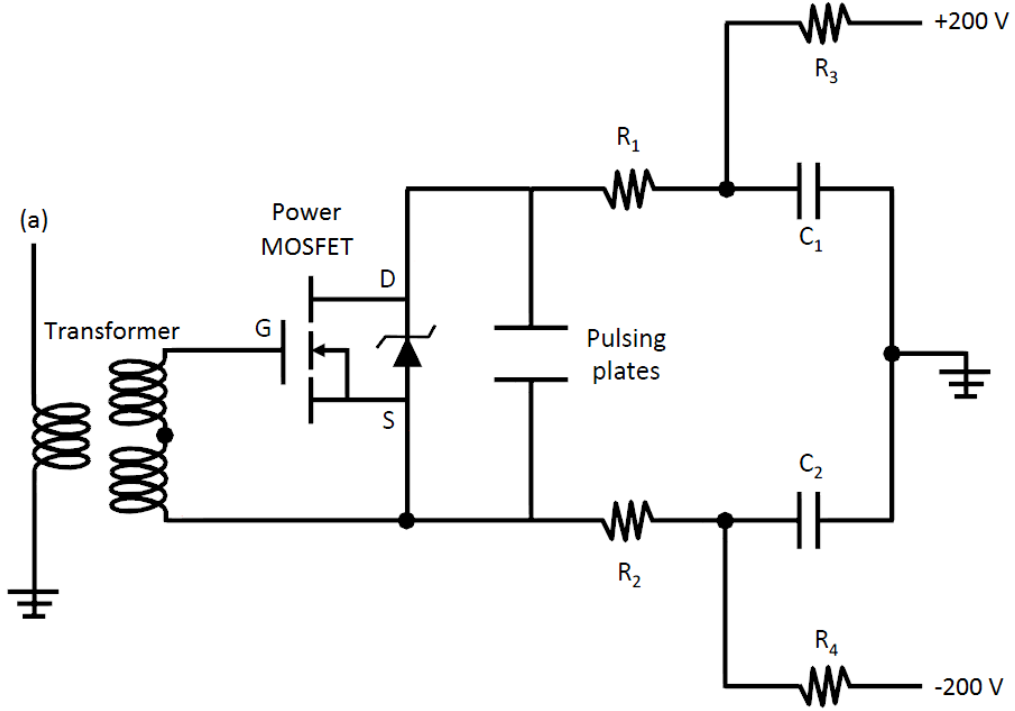


FIGURE 3.4. Pulsing circuit. $R_1 = R_2 = 470 \Omega$, $R_3 = R_4 = 20 \text{ k}\Omega$, $C_1 = C_2 = 680 \text{ nF}$. [36]

signals are shown in Fig. 3.5(a). The pre-amp output voltage is related to the input current according to Eq. 19:

$$(19) \quad I = \frac{-(V_{out} + R_1 C \frac{dV_{out}}{dt})}{R_1 M}$$

where $R_1 C$ and $R_1 M$ are determined by putting a known square pulse of current into the pre-amp through a large resistor. First, the time constant of an exponential fit to the signal decay after the pulse determines $R_1 C$. Then $R_1 M$ is determined by matching this shaped signal to the original square pulse. The actual currents in the induction plates and cup 3 derived using Eq. 19 are shown in Fig. 3.5(b). The induction signal is positive as ions are approaching the middle plate, and an equal but negative signal is seen after the ions pass

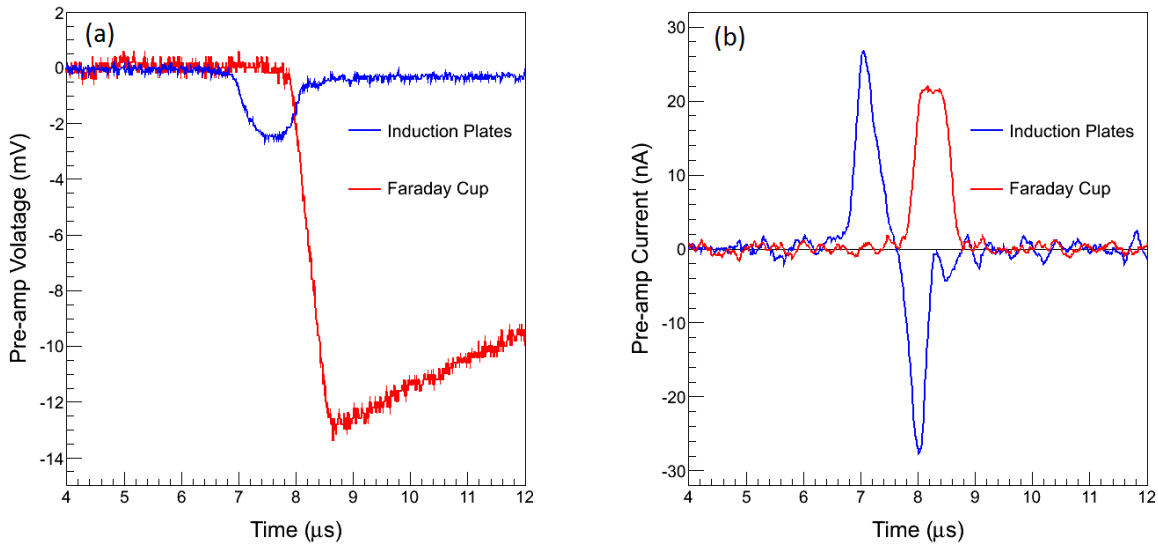


FIGURE 3.5. Raw (a) and shaped (b) pulse signals from induction plates and cup 3. The raw induction signal appears small because it is a less sensitive pre-amp (accounted for in shaping).

through. The Faraday cup stops the ions, so it produces only a positive induction signal as ions approach it.

Pulsing data also provide confirmation that the beam is composed of Ba^+ . The time between the center of the pulsing plate voltage overlap and the center of the pulse measured by the Faraday cup, along with the known distance traveled, determines the velocity measurement of the ions. The distance from the center of the pulsing plates to the Faraday cup was measured to be 31.5 ± 0.5 cm. Time-of-flight data, e.g. Fig. 3.6, give 39.8 ± 3.4 amu for Ar^+ ions and 136.8 ± 6.3 amu for Ba^+ ions, including an uncertainty on the time of flight of $\pm 0.1 \mu\text{s}$. These agree with the known atomic masses.

3.1.5. CALIBRATION OF ION DEPOSITS

The ratio of between ion current in cup 3 and cup W is measured to be $0.5 \equiv r_w$. Then, the ion density per pulse at the sapphire window is defined by:

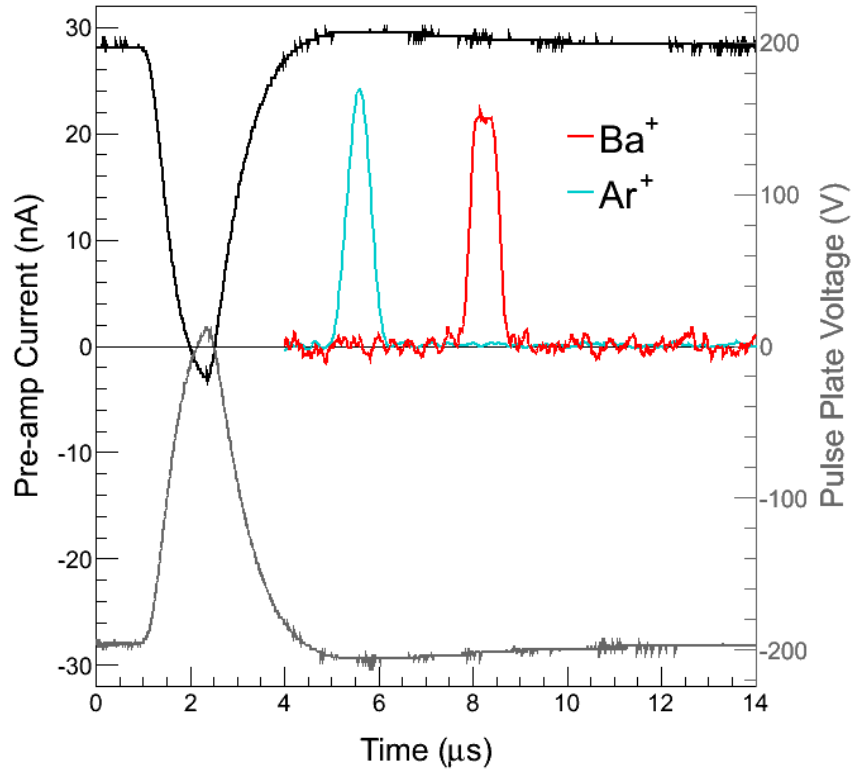


FIGURE 3.6. Arrival time of pulses at cup 3 vs. time of pulsing plate signal (black (+) and gray (-)) for Ar^+ and Ba^+ ions at 2000 eV.

$$(20) \quad \frac{\text{ions}}{\text{pulse} \times m^2} = \frac{Qr_w}{eA}$$

where Q is the charge/pulse at cup 3, A is the area of cup W, and e is the elementary charge. The radius of the opening in cup W is 1.4 mm. Each time cup W is inserted, the voltages on the final deflection plates H2 and V2 which optimize the signal in cup W, in pulsed and continuous mode, are determined. In the latest imaging experiments, these differed from the values for maximum cup 3 signal by about 70 V in H2 and 60 V in V2, corresponding to an effect of the undeflected beam of about 4 mm in x and y position at cup W relative to the center line from cup 3. This indicates the level of drift in optimal ion beam component settings that occur over time.

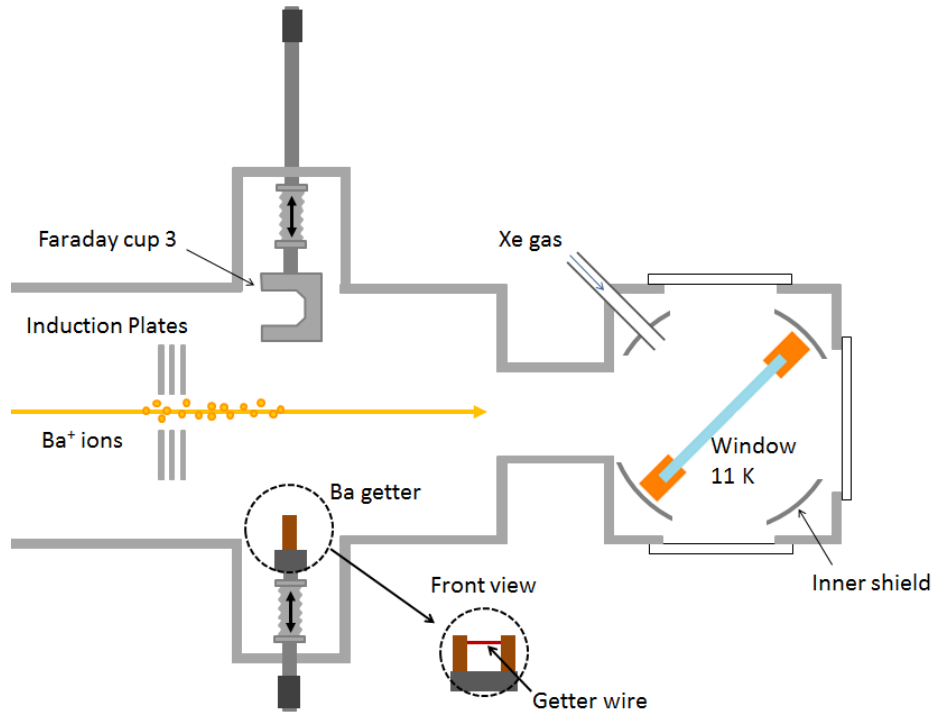


FIGURE 3.7. Apparatus near sapphire window, including induction plates, Ba getter, Faraday cup 3, Xe gas inlet, and sapphire window at 11 K.

3.2. BA GETTER SOURCE

A BaAl_4 getter, manufactured by SAES with part number ST 2/F/WIRE, can be inserted on a bellows to emit toward the sapphire window, as shown in Fig. 3.7. When heated, the getter emits neutral Ba with minimal Ba^+ due to the low temperature ($\sim 800^\circ \text{ C}$ determined by observing brick red color temperature). Getters were used extensively in previous work [37] for measuring the absorption and emission spectra of Ba in SXe with large Ba deposits. A getter was used briefly in this work in verifying that the 619-nm fluorescence peak, that is used for single Ba imaging, is actually a neutral Ba peak, as described in Section 5.2. The barium getters used in [37] were exothermic $\text{BaAl}_4\text{-Ni}$ flash getters. The getter used here is an endothermic BaAl_4 type, designed for more controlled Ba emission.

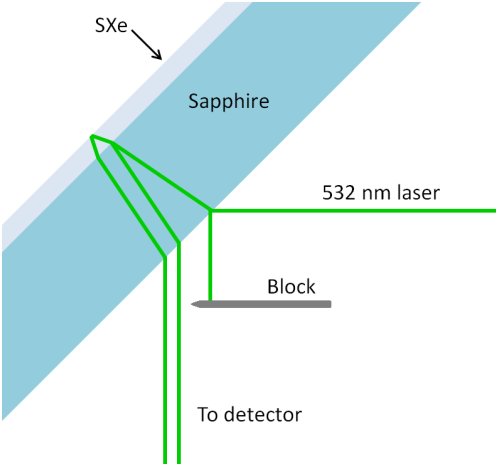


FIGURE 3.8. Setup for measuring SXe deposition rate by interference fringes.

3.3. SAMPLE DEPOSITION

The Ba^+/Ba is co-deposited with 99.995% purity Xe gas onto a cold sapphire window. Sapphire has good thermal conductivity at low temperature and good optical transparency in the visible. The window is held in a copper mount attached to a coldfinger and is tilted at 45° to allow access of the ion beam and Xe gas, as well as the excitation laser and collection optics. To begin a deposit, Xe gas is flowed toward the window via a leak valve, through an inlet system designed and built by Brian Mong and Shon Cook [37, 36]. Cup 3 is then retracted and the pulsing plates are pulsed to zero volts, depositing $1-\mu\text{s}$ pulses of Ba^+ ions into the SXe matrix as it grows. Cup 3 is then replaced, and the Xe leak stopped.

The SXe matrix deposition rates have been measured by interference fringes in a laser reflected from the front surface of the sapphire window and the SXe surface, as shown in Fig. 3.8. Fringes for SXe deposition at 52 K and 11 K are shown in Fig. 3.9(a) for the typical leak rate used in this work. The refractive index of SXe has a negligible dependence on temperature between 50 and 30 K [38], so these rates can be compared directly. A distribution of SXe deposition rate measurements from several deposits is shown in Fig.

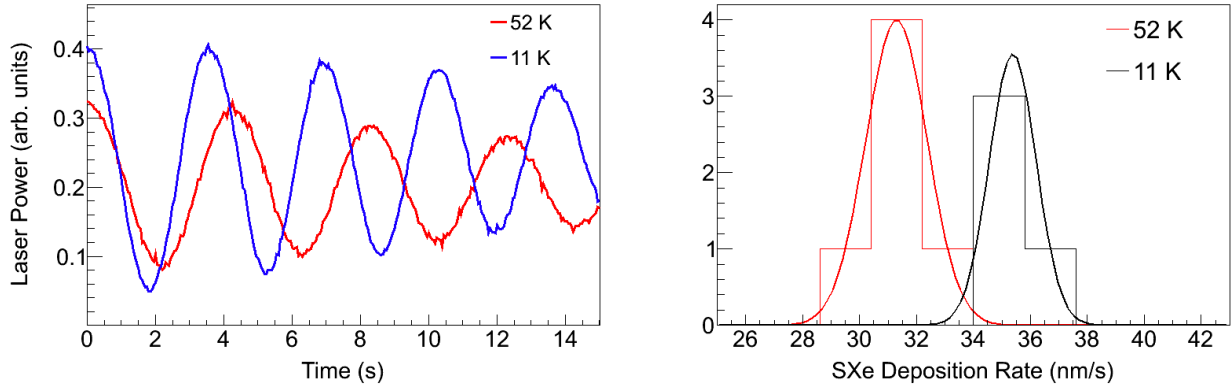


FIGURE 3.9. (a) Interference fringes for the same Xe gas leak rate deposited on the sapphire window at 11 K and at 52 K, and (b) distribution of SXe deposition rates calculated from fringe period of several measurements.

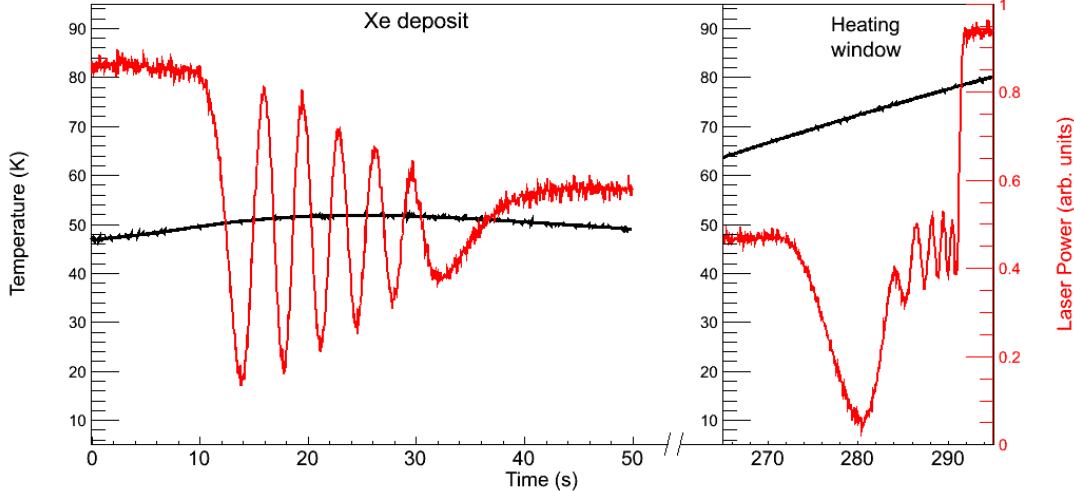


FIGURE 3.10. Interference fringes of a deposit at 52 K and of its subsequent evaporation when heating the sapphire window, and temperature vs. time curves.

3.9(b). A rate of 31.2 ± 0.9 nm/s is measured for deposits at 52 K, and a somewhat higher rate of 35.6 ± 0.9 nm/s is measured for deposits at 11 K.

To evaporate a sample, the window is heated to 100 K. Fringes appear during this process as well. The full set of fringes for a deposit at 52 K and its evaporation when heated is shown in Fig. 3.10, along with the window temperature. It is observed that the SXe evaporates between 73 K and 78 K. The same number of fringes appear in the deposit and

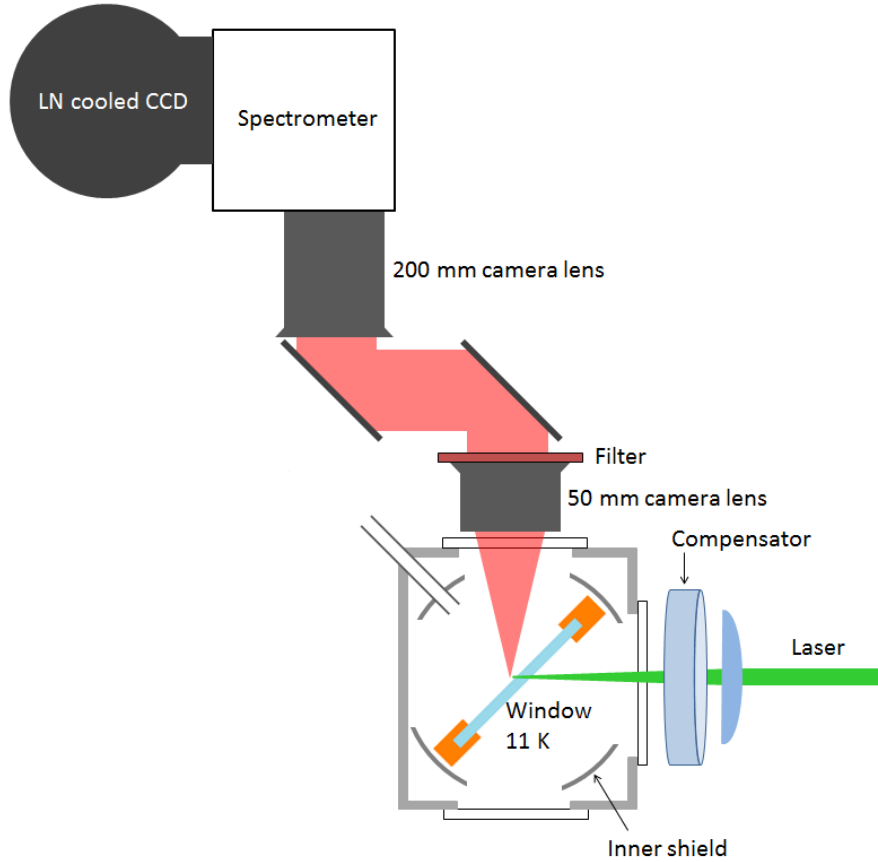


FIGURE 3.11. Apparatus in spectroscopy region, including optics for excitation, fluorescence collection, spectroscopy and detection.

the evaporation, indicating that the lower deposition rate at around 50 K is not due to simultaneous evaporation, but perhaps due to a different sticking coefficient. The variance in temperature during the deposit is due to the heater cycle. These Xe deposits were for a longer time than in a typical deposit during a fluorescence experiment, in order to observe several fringes.

3.4. LASER EXCITATION

Green to yellow laser excitation is done with a Coherent 599 dye laser, pumped by the 514-nm line of a Lexel 3500 Ar ion laser. Rhodamine 110 (R110) dye is used for the 542 - 566 nm wavelength range, and Rhodamine 6G (R6G) for the 567 - 590 nm range. Another

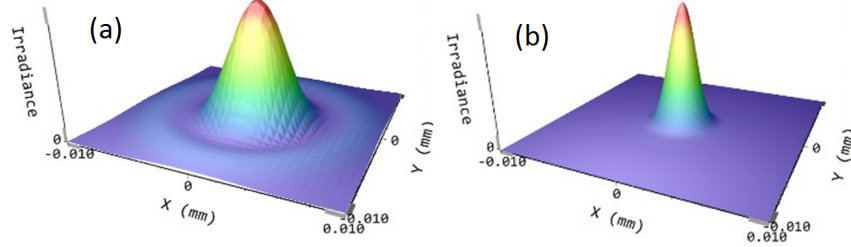


FIGURE 3.12. Calculated minimum laser spot size distributions, with wavelength 570 nm and incident laser radius $w = 7$ mm, for (a) bi-convex $f = 7$ cm lens, and (b) aspherical $f = 7.9$ cm lens. [39]

Coherent 599 dye laser with Coumarin 480 (C480) dye is used for blue excitation, which is pumped by a Kr ion laser. The Coherent 599 dye lasers are used with birefringent filters for wavelength tuning, but without etalons or single frequency stabilization, since the broad absorption of Ba in SXe does not require narrow band laser excitation.

The optics for these experiments is shown in Fig. 3.11. In initial work, including spectroscopy (Chapter 5) and some imaging (Chapter 6), a bi-convex was used. This lens had a little spherical aberration, resulting in blurring of the laser focus. This aberration does not affect the spectroscopy results in Chapter 5, where semi-focused beam $1/e^2$ radii of 100-1000 μm were used. However, spherical aberrations caused the minimum beam radius to be about 5 μm . To approach the diffraction limit in imaging small numbers (Chapter 6), a 7.9-cm focal length aspherical lens was used. A comparison of the minimum spot sizes for these two lenses, calculated by David Fairbank with Thorlabs software, is shown in Fig. 3.12.

The tilted sapphire window introduces astigmatism to the focused laser. To correct for this, compensating astigmatism is introduced by a fused silica optical flat of 1 cm thickness, placed after the lens, tilted in the y plane (the laser is along the z-direction, and the sapphire window is tilted in the x plane). The proper angle for the compensator was determined to be about 10° from normal by a ray matrix calculation [40]. The astigmatism of the SXe

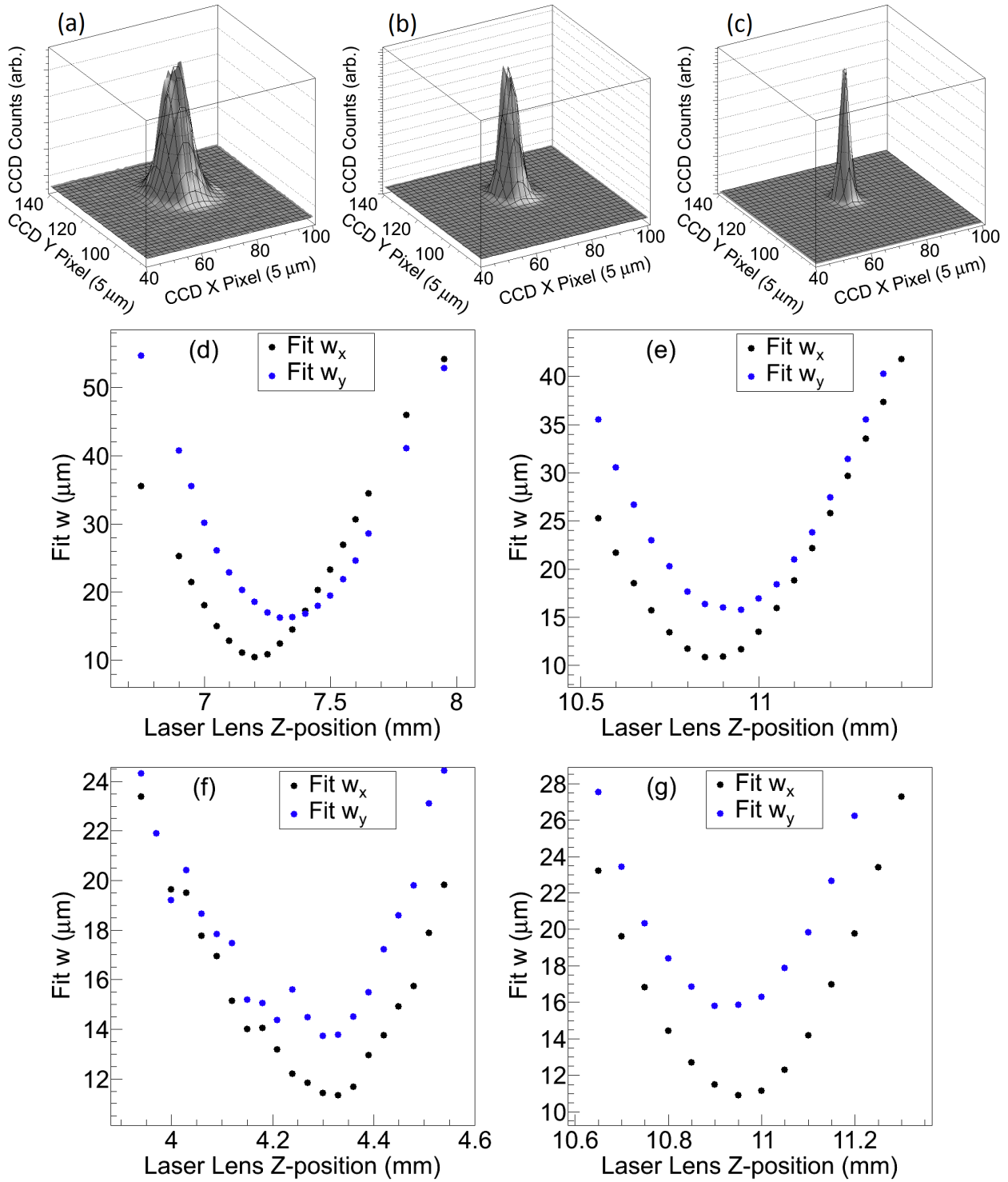


FIGURE 3.13. Example 2D Gaussian fits (black grid lines) with varying laser z position (a,b,c), and fit radii w_x (black) and w_y (blue) vs. laser focus lens position with (d) no compensator, and with compensator at about (e) 10°, (f) 11°, and (g) 13°.

layer is negligible since its thickness is only about half a micron in a typical fluorescence experiment. With the compensator, overlapping minimum spot sizes of $2.06 \mu\text{m}$ and $2.66 \mu\text{m}$ are calculated for x and y, respectively.

To observe the astigmatism and the effect of the compensator, the relative positions in z of the x and y foci were observed by imaging 619-nm Ba fluorescence from a large deposit of Ba^+ in SXe, with a varying laser focus. For each z-position of the laser focusing lens, an image was taken, and a 2D Gaussian fit determined the $1/e^2$ x- and y- radii, w_x and w_y , of the image. Although these radii are significantly larger than that of the laser beam due to SXe surface scattering and collection optics imperfections, the z-position of the best focus can be accurately determined. Example fits to the 619-nm fluorescence images for three laser focus positions, using the astigmatism compensator at $10\pm1^\circ$, are shown in Fig. 3.13(a,b,c). Gaussian fit values for w_x and w_y are plotted vs. laser focus position with (d) no compensator, and with the compensator at (e) $10\pm1^\circ$, (f) $11\pm1^\circ$, and (g) $13\pm1^\circ$. With no compensator (d), the focal positions for x and y are measured to be $127.6\pm2.5 \mu\text{m}$ apart. Compensation angles $10\pm1^\circ$ (e) and $13\pm1^\circ$ (g) can be seen to under- and over-shoot the optimal angle, respectively. The angle $11\pm1^\circ$ (f), which was used in imaging experiments, is near optimal, i.e. the x and y focal positions are consistent to within $45 \mu\text{m}$.

The laser spot size (A_{laser}) is defined as the area enclosed within the $1/e$ radii of the laser beam, according to Eq. 21:

$$(21) \quad A_{\text{laser}} = \frac{\pi w_x w_y}{2}$$

where $w_{x,y}$ are the x and y $1/e^2$ radii of the focused laser in the SXe. In the case of the bi-convex lens, $w_x \approx w_y \equiv w$.

3.5. COLLECTION OPTICS

Fluorescence is collected above the cryostat, as shown in Fig. 3.11. A 50 mm Nikon camera lens collimates the light, and one or more fluorescence filters sit on top of it. A band-pass filter is used for imaging, and a Raman filter is used for spectroscopy. The fluorescence is then guided by two steering mirrors, and is imaged by a 200 mm Nikon camera lens onto a Roper Scientific liquid-nitrogen-cooled CCD, with a net magnification of 4. The CCD has a quantum efficiency of 90% in the visible, and in its medium gain mode, records one count per four photoelectrons collected. At the set point of -100 °C, dark counts are negligible.

For spectroscopy, the 200 mm camera lens focuses the light onto the inlet slit of an Acton SP-2150i imaging spectrometer, which is then imaged by the spectrometer onto the CCD after reflecting off a diffraction grating. The 0-order reflection of the grating provides an image for alignment, and the grating can be tilted to distribute the 1st-order reflection across the horizontal CCD pixels for doing spectroscopy.

When a 1" diameter filter is used, the imaging system has a solid angle collection of about 1.5%. Each additional component in the collection optics, listed in Table 3.1, contributes some loss, resulting in a total collection efficiency (ϵ_c) of 1.1×10^{-3} with the spectrometer, and 2.1×10^{-3} without. The spectrometer also limits the system to an f-number of 4, though this is not limiting in this setup.

To avoid unnecessary fluorescence bleaching, a laser shutter was linked to the camera shutter with a LabVIEW program. This program also recorded laser power via a calibrated

TABLE 3.1. Factors contributing to optical collection efficiency. Total ϵ_c includes 1.5% solid angle collection.

Component	Efficiency	
Cryostat Window	0.99	
Camera Lens 50 mm	0.89	
Camera Lens 200 mm	0.91	
Steering Mirrors ($\times 2$)	0.95	
CCD Quantum Efficiency	0.90	
Filter	0.98	
Counts per Photoelectron (CCD)	0.22	$\epsilon_c(\text{w/o spectrom.}) = 2.1 \times 10^{-3}$
Spectrometer	0.5	$\epsilon_c(\text{w/ spectrom.}) = 1.1 \times 10^{-3}$

pickoff, as well as the temperature of the coldfinger near the sapphire window during observation.

Although the imaging spectrometer can produce spacial images with the 0-order grating reflection, better collection efficiency and imaging quality are achieved by removing the spectrometer and imaging directly onto the CCD. Band-pass filters were used to pass the desired Ba fluorescence peak(s) while greatly attenuating laser scatter and sapphire fluorescence.

An example raw image of the focused 570 nm dye laser on a Ba⁺ deposit using the fluorescence of the 619-nm peak is shown in Fig. 3.14. With 4 \times magnification, each pixel corresponds to 5 $\mu\text{m} \times 5 \mu\text{m}$ on the window. The laser's path through the window is faintly visible by the residual broad Cr³⁺ fluorescence that is passed by the 620-nm band-pass filter. The laser is focused at the top surface of the window, which faces the ion beam. The surface background is seen on the back surface, and the 619-nm Ba fluorescence stands out above both backgrounds on the top surface. The imaging resolution results in a 1/e² radius of about 12 μm when imaging the 2.06 $\mu\text{m} \times 2.66 \mu\text{m}$ 1/e² laser spot.

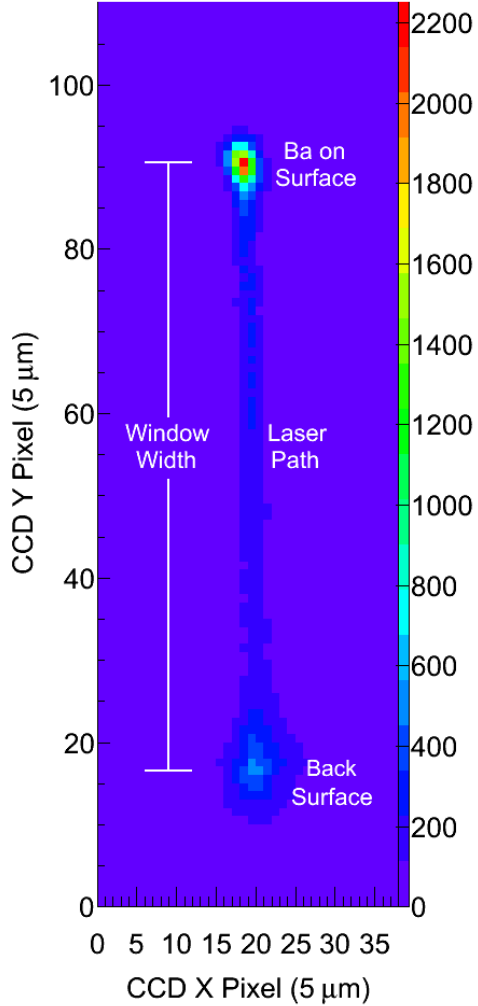


FIGURE 3.14. Example image of focused laser exciting a Ba^+ deposit on a c-plane sapphire window of 0.5 mm thickness. Fluorescence is passed by 620-nm band-pass filter.

3.6. WAVELENGTH CALIBRATION

Wavelength calibration of the spectrometer was done using three lasers whose wavelengths were first measured with a Burleigh Wavemeter: a red diode laser at 656.99 nm, a doubled Nd:YAG laser at 532.23 nm, and the C480 blue dye laser typically around 475 nm. These lasers were directed at the same position on the sapphire window, and their scatter was imaged along the same path as the Ba fluorescence. The WinSpec software applies the diffraction grating equation to calibrate each CCD pixel to a wavelength.

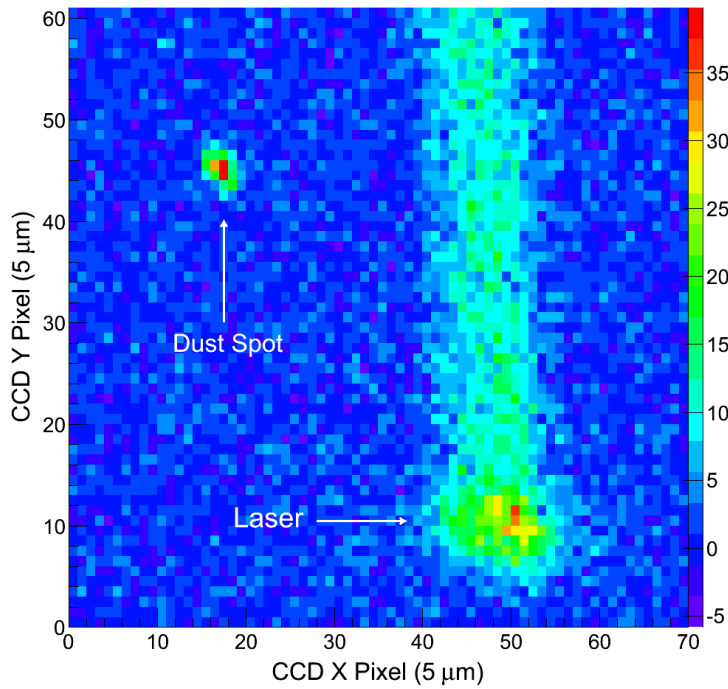


FIGURE 3.15. Example image of dust spot and laser during observation of cryostat vibrations.

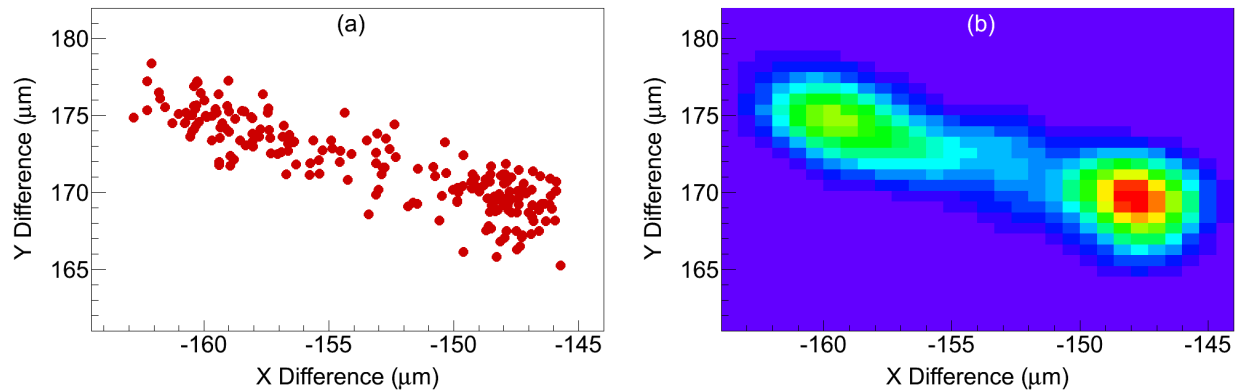


FIGURE 3.16. Cryostat vibration measurements based on relative position of dust spot vs. laser on sapphire window in 50-ms snapshots (a), with 2D Gaussians of $w_x \times w_y = 2.06 \mu\text{m} \times 2.66 \mu\text{m}$ overlaid on each point to represent total laser exposure vs. position (b).

3.7. VIBRATIONS AND EFFECTIVE LASER REGION

Relative vibrations between the laser and the sapphire window occur from a few sources.

Firstly, the laser is on a separate optical table from the cryostat and collection optics.

Secondly, the cryostat has some vibration due to its He pump cycles. Vibrations affect the total number of Ba atoms exposed during a measurement, but not the instantaneous number of Ba atoms in the laser beam area. Vibrations were observed by determining the position of a “dust spot” (a highly scattering feature on one sapphire window) relative to the position of the laser in an image on time scales down to 50 ms. An example of an image from this experiment is shown in Fig. 3.15. The dust spot was illuminated by a de-focused 657 nm diode laser, and the 570-nm dye laser was somewhat de-focused in order to optimally de-focus the red laser with the same focusing lens. For each frame, 2D Gaussian functions with variable widths and magnitudes were fit to locate the center of the laser spot and the dust spot in order to measure their relative position. The fit range for the laser spot was restricted in y so that it was not affected by the bulk sapphire fluorescence path. The distances in x and y between the dust spot and laser are plotted for each 50-ms snapshot in Fig. 3.16(a). The distribution shows a correlation between x and y, indicating vibration in a particular direction. The amplitude of the vibration is about $15 \mu\text{m}$ from this data. To calculate an effective laser spot size due to this vibration, each difference (x,y) between laser and dust spot was used as the center of a 2D Gaussian, each with $w_x = 2.06 \mu\text{m}$ and $w_y = 2.66 \mu\text{m}$ to represent the laser spot. Such Gaussian functions were summed for all points to produce a distribution of summed laser exposure, shown in Fig. 3.16(b). The area enclosed by a $1/e$ contour then is a measure of the effective total exposed area. On the other hand, signal at a given moment is still emitted only from the laser spot size. Then there are two possible definitions for the number of ions in the laser region, and thus the upper limit on the number of atoms. In the absence of signal bleaching, the instantaneous number of atoms exposed is a good definition for the number of atoms observed. If there is

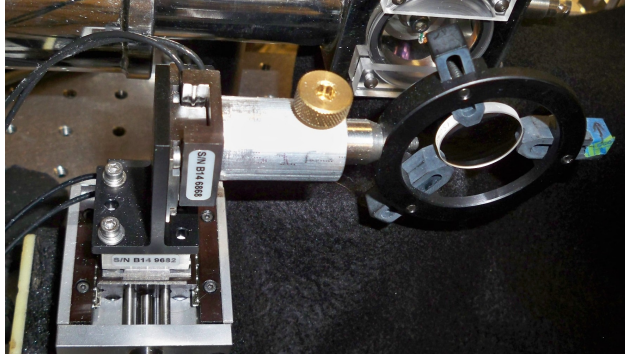


FIGURE 3.17. Asphere laser focusing lens mounted to two motorized Newport translation stages for laser scanning in x and y.

large bleaching, the more conservative estimate is more appropriate. Note that the factor between instantaneous and total exposure areas depends on the laser spot size. The factor is about 4.7 for $w_x \times w_y = 2.06 \mu\text{m} \times 2.66 \mu\text{m}$ (astigmatism compensation and no spherical aberration), and about 3 for $w_x \times w_y = 5 \mu\text{m} \times 5 \mu\text{m}$.

For imaging of single Ba atoms, the relative vibration is the vibration of most concern. Vibration of the laser itself is seen to be small in this study. Vibration of the collection optics will affect the imaging resolution, but not the number of atoms being observed, or the resolution of a single atom iamge in a laser raster scan. These vibrations were minimized by stable mounting on large diameter posts.

3.8. LASER SCANNING

In order to obtain images of separated single atoms, the laser focusing lens is attached to motorized translation stages which scan the laser position by scanning the lens in x and y, as shown in Fig. 3.17. These stages sat atop a manual z-translation stage for laser focusing. A LabVIEW program coordinates movement of these stages such that x or y position is stepped in between CCD frames, and each frame then corresponded to a position in a laser scan grid.

Relative laser-window vibration may be eliminated by using a different cryostat, or by gating the laser with a shutter to block exposure during He pump surges. With no vibration, resolution of Ba atoms in scanned images is limited only by the size of the laser beam, not by the resolution of the collection optics and the CCD pixel size.

CHAPTER 4

METHOD

The method of spectrum fitting is discussed in Sec. 4.1, which is used in analysis for separating contributions of semi-resolved fluorescence peaks. Background signals are discussed in Sec. 4.2 with the purpose of optimizing signal-to-background.

4.1. FITTING OF SPECTRA

In most circumstances, the different fluorescence peaks in a spectrum overlapped. Thus it was necessary to fit the fluorescence spectra with a sum of peak-specific fit functions in order to extract peak heights and integrals. These were used, e.g., in excitation spectra, annealing, and bleaching curves for different peaks. Gaussians, Lorentzians and asymmetric functions were used, depending on the best match to a specific peak.

4.1.1. FITTING SPECTRA WITH GREEN EXCITATION

Example fits to spectra of Ba⁺ deposits for several different green excitation wavelengths are shown in Fig. 4.1. To incorporate the tail in the shape of the 577- and 591-nm peaks, an asymmetric function of the form $A(1+\text{erf}(\frac{x-a}{\sigma_1})(1-\text{erf}(\frac{x-a}{\sigma_2}))$ was used, where a is the fixed center-defining parameter, σ_1 and σ_2 are fixed left and right width parameters, and A is the free amplitude parameter. The function erf() is an error function. The 570-, 601-, 619-, and 670-nm peaks were fit with Gaussian functions with fixed widths (σ) of 1.7 nm, 4.7 nm, 5.3 nm, and 6.7 nm, respectively. Rather than attempting frame-by-frame background subtractions, additional Gaussians were fit to the broad and sharp background fluorescence. Two broad Gaussians centered at around 590 nm and 702 nm, and one sharp Gaussian at 694 nm, were chosen by fitting spectra of Xe-only deposits. These backgrounds

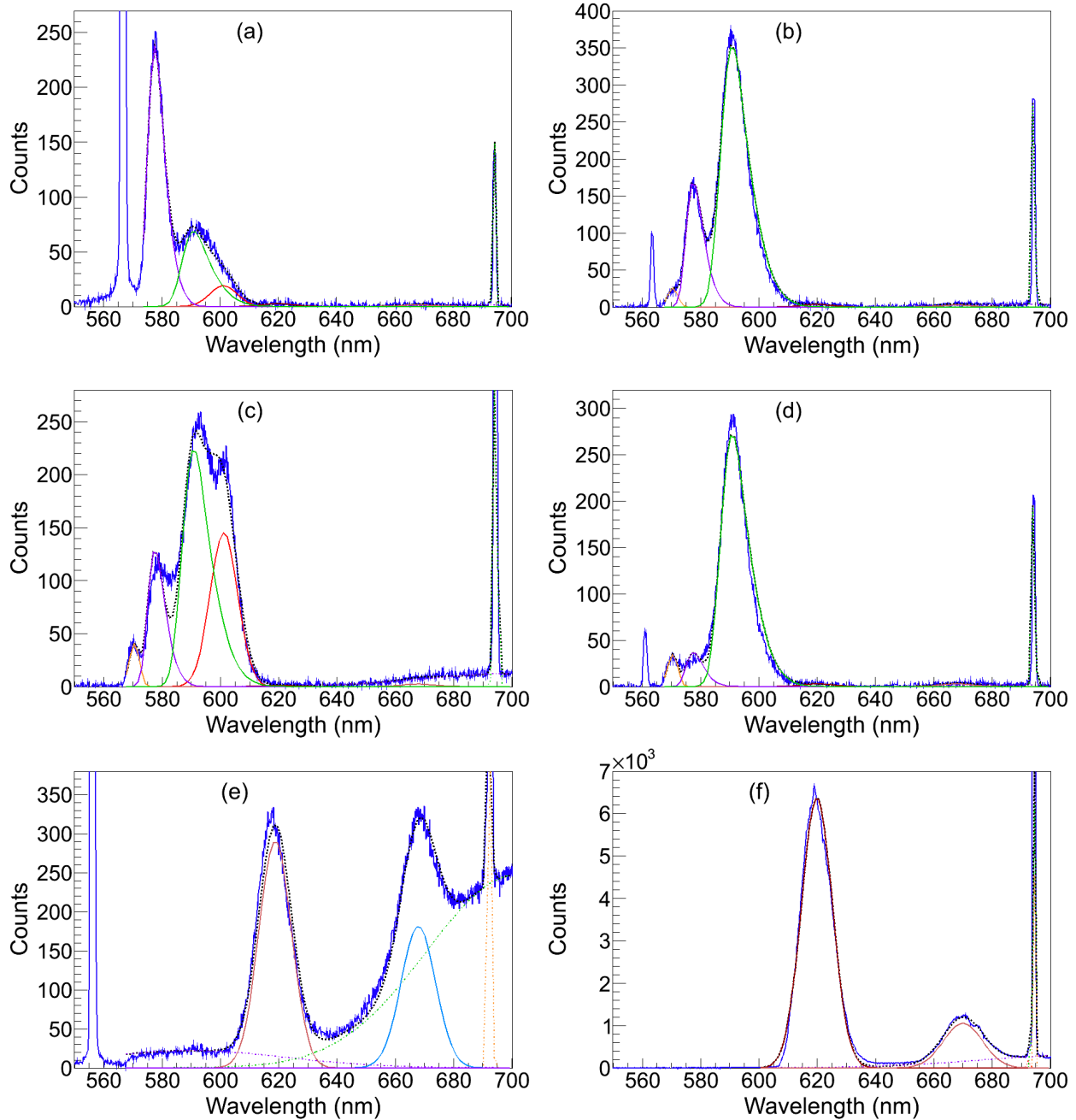


FIGURE 4.1. Example fits to spectra of Ba^+ deposits with green excitation at (a) 566.6 nm, (b) 563.4 nm, (c) 546.3 nm, (d) 561.0 nm, (e) 555.9 nm, and (f) 567.3 nm. Laser scatter can be seen in the lower wavelengths for some figures, especially in (a) where it is on the edge of the Raman filter cutoff.

and their excitation spectra are discussed in 4.2. The full fit, i.e. the sum of each contributing peak fit, is the dotted black line. Though the shapes do not match perfectly for all excitation wavelengths, the fits still follow the peak amplitudes well. Ba emission and excitation spectra results are discussed in Sec. 5.1.

4.1.2. FITTING SPECTRA WITH BLUE EXCITATION

Example fits to spectra of Ba^+ deposits for several different blue excitation wavelengths are shown in Fig. 4.2. Gaussian functions were used for 532-, 568-, and 575-nm peaks with standard deviations (σ) of 2.4 nm, 5.0 nm, and 0.7 nm, respectively. Lorentzian functions were used for the 553-, 592-, 635-, and 669-nm peaks with half width at half maxima (γ) of 1.7 nm, 13.8 nm, 10.4 nm, and 9.1 nm, respectively. Similar to spectra with green excitation, the background components were fit with two broad Gaussians centered at 546.0 nm and 703.3 nm, with respective σ of 49.0 nm and 30.5 nm, as well as one sharp Gaussian centered at 693.4 nm peak with σ of 0.5 nm. The fits around 478 nm (e.g., (c)) are not quite right, mainly due to a shift in central value of the 592-nm peak. However, fit values still follow respective peaks heights well. The 522- and 575-nm peaks are seen in (c), though the 522-nm peak is left out of the fitting range since it sits on the edge of the Raman filter cutoff. These spectra are discussed in Sec. 5.5.

4.2. BACKGROUND SPECTRA

The sharp and broad background discussed in Sec. 4.1.1 is mainly due to Cr^{3+} impurity ions in the sapphire window. A spectrum of this fluorescence with 562 nm excitation is shown in Fig. 4.3(a). The strong, sharp peak at 694 nm is a well-known $^2E - ^4A_2$ emission in the d^3 configuration of Cr^{3+} impurities in the sapphire bulk [41, 42]. An excitation spectrum

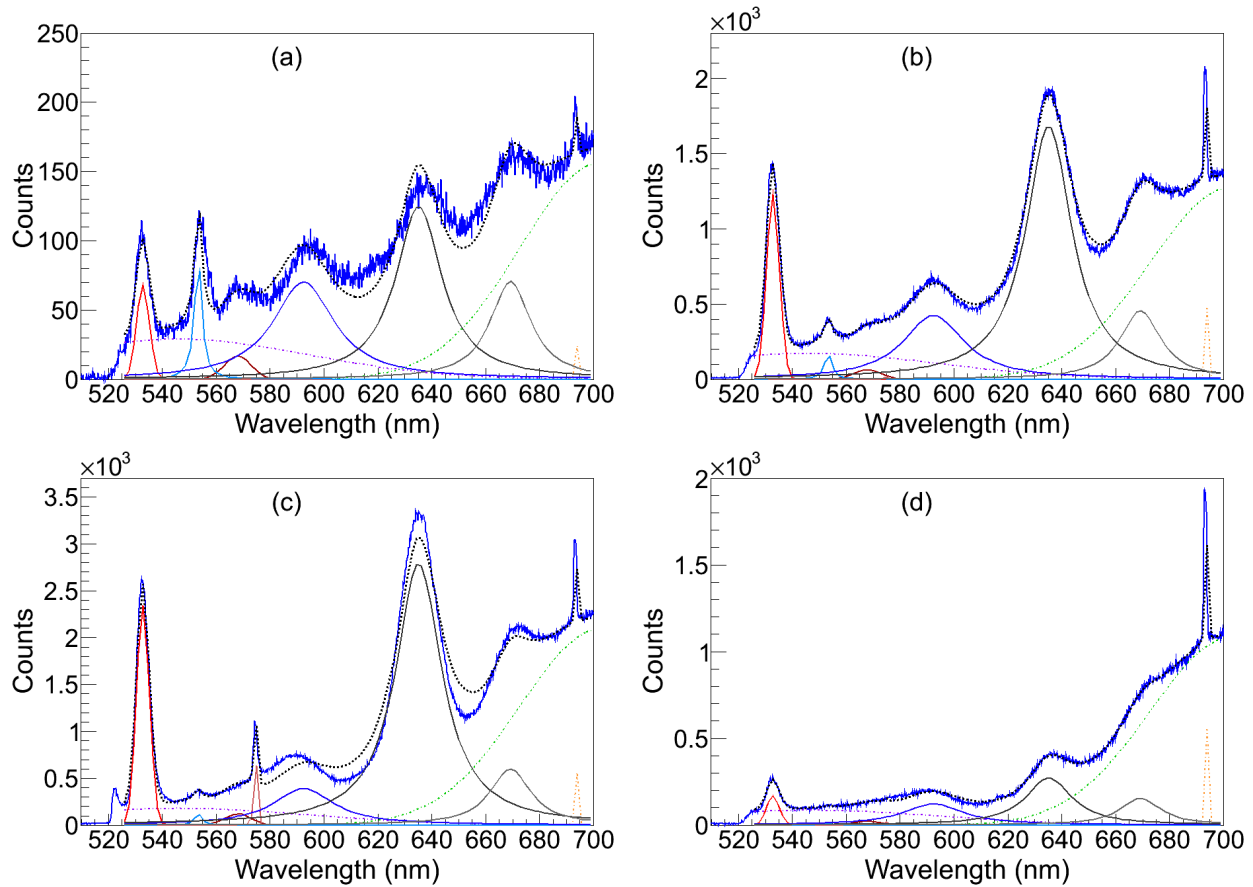


FIGURE 4.2. Example fits to spectra of Ba^+ deposits with blue excitation at (a) 461.7 nm, (b) 468.2 nm, (c) 478.3 nm, and (d) 488.2 nm.

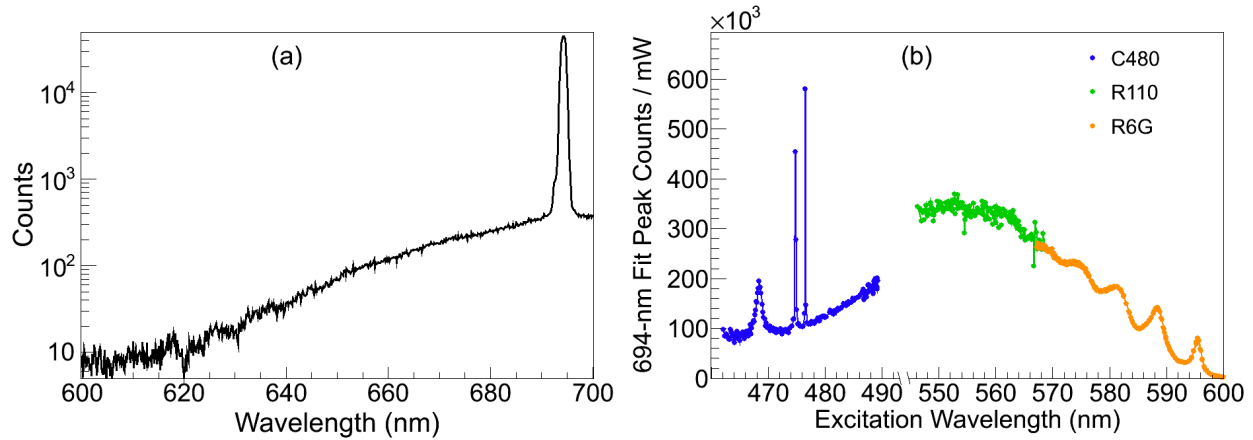


FIGURE 4.3. (a) Sapphire bulk emission with 562-nm excitation at 11 K, and (b) excitation spectrum of the sharp 694-nm emission peak using three different laser dyes. Due to different laser powers and exposure times, the R110 and R6G were scaled to match at their boundary.

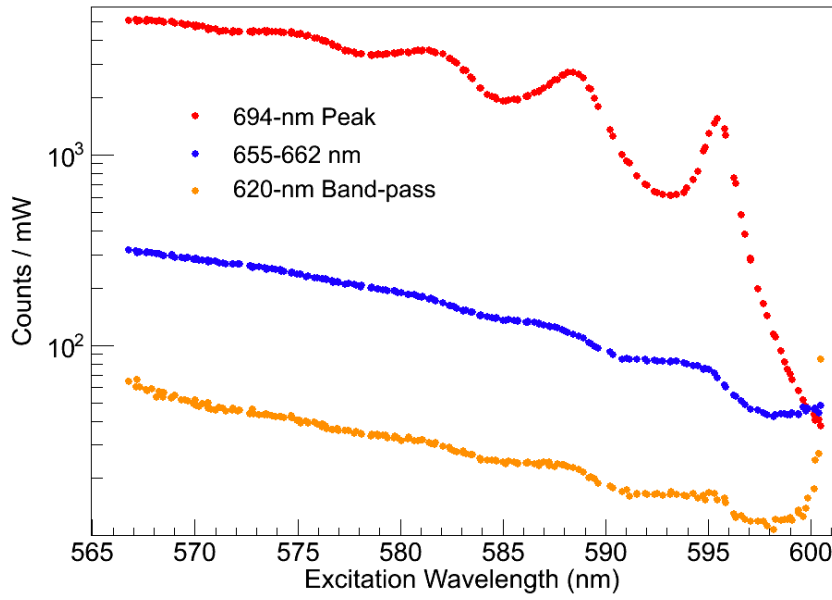


FIGURE 4.4. Excitation spectra for weaker sapphire bulk emissions (blue,orange) along with that of the strong 694-nm emission (red) at 11 K.

for this peak is shown in Fig. 4.3(b) over the range all three dyes R6G, R110, and C480, using one of the sapphire windows with higher Cr^{3+} content. Multiple features are observed in the excitation spectrum, obtained by integrating the 694-nm peak fit (Sec. 4.1) vs. excitation wavelength. The broad absorption in the green/yellow, peaking around 550 nm, with vibrational peaks on the red tail, agree with well understood features in the spectrum of Cr^{3+} in sapphire at 77 K, including three sharp peaks in the blue at 468.4, 474.8, and 476.5 nm [43, 44]. In addition to the 694-nm peak, a weaker and much broader emission is observed, along with three weak peaks in the 615-635 nm region. Excitation spectra for these fluorescence components are shown in Fig. 4.4 for the R6G dye range. In this experiment, the laser was de-focused to about $w = 200 \mu\text{m}$, and the emission observed had contribution of the surface background as well as the bulk sapphire emission. This is negligible for the prominent 694-nm peak, however the rising features of the surface background emission, near 600 nm and 567 nm, can be seen in the excitation spectra of the weaker components (blue,

and especially orange curves in Fig. 4.4). Nonetheless, observation of the same vibrational peaks as in the 694-nm peak excitation spectrum demonstrates that the broad emission and weak peaks in the 620 band-pass (Fig. 4.3(a)) are also due to Cr³⁺ in the sapphire. Commercially available c-plane quality sapphire windows contain low concentrations of Cr³⁺. Sample windows of 0.75" diameter and 0.02" thickness from a few companies were tested, and those from Meller Optics produced the lowest sapphire bulk emission in the 620-nm band-pass region.

An additional background emission was observed from the surfaces of the window. Its broad fluorescence is shown in Fig. 4.5(a) with a 610-nm Raman filter cutoff and 570.4 nm excitation, and its excitation spectrum is shown in Fig. 4.5(b) over the R6G dye range. The nature of this emission has not been determined, however a few features were identified. One was that the emission increased as the window temperature was decreased, down to about 100 K where it remained flat down to 11 K, shown in Fig. 4.6. Another feature of the surface background is that it bleaches with laser exposure. In order to reduce this background in imaging experiments, as well as to reduce run-to-run variation in the background due to bleaching, the sapphire window was pre-bleached for at least half an hour. Decay of the surface background emission, with intermittent observation during a pre-bleaching process, is shown in Fig. 4.7. For efficient pre-bleaching, the dye laser tuned to 580.5 nm for higher laser power, though the observation points in Fig. 4.7 are taken with the dye laser at 570 nm with the same laser power used in the following Ba imaging experiment. During imaging experiments, frequent Xe-only deposits were made in order to track surface background emission to establish proper background subtraction.

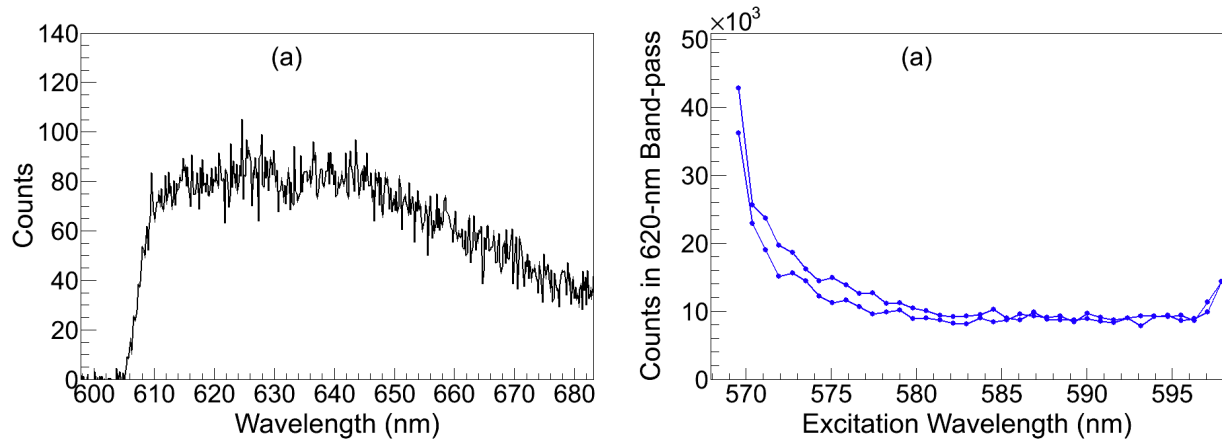


FIGURE 4.5. (a) Surface background emission spectrum w/ excitation at 570.5 nm, and (b) excitation spectrum through wavelengths in R6G dye range. The sharp drop in (a) around 608 nm is the Raman filter cutoff.

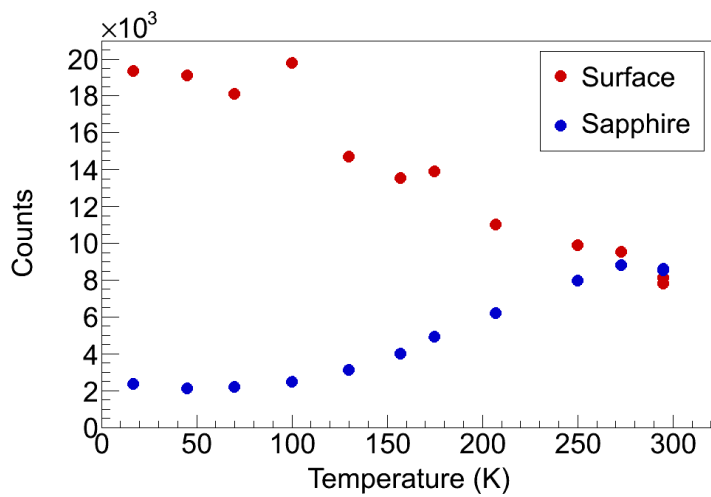


FIGURE 4.6. Temperature dependence of surface (red) and sapphire bulk (b) backgrounds.

Consideration of signal-to-background (S/\sqrt{B}) guided the choice of 570 nm for excitation of the 619-nm fluorescence. S/\sqrt{B} for emission passed by the 620-nm band-pass filter is plotted vs. excitation wavelength in Fig. 4.8 for the surface background (B_{surf}) as well as for the sapphire bulk emission (B_{sap}). The peak in S/\sqrt{B} represents the optimal excitation wavelength respective to each of the two background sources. Around 568.5 nm is optimal vs. the sapphire emission, and around 571 nm is optimal vs. the surface background emission.

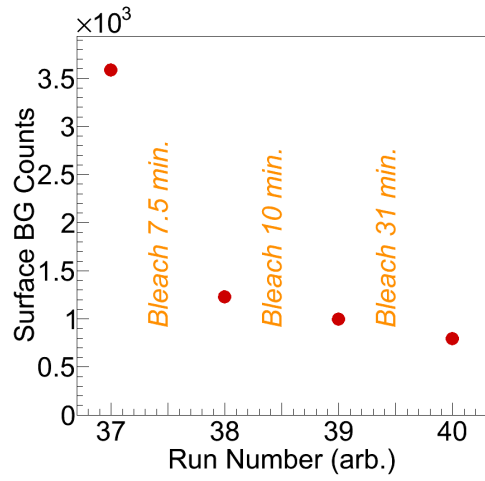


FIGURE 4.7. Decay of surface background emission during pre-bleaching of the sapphire window.

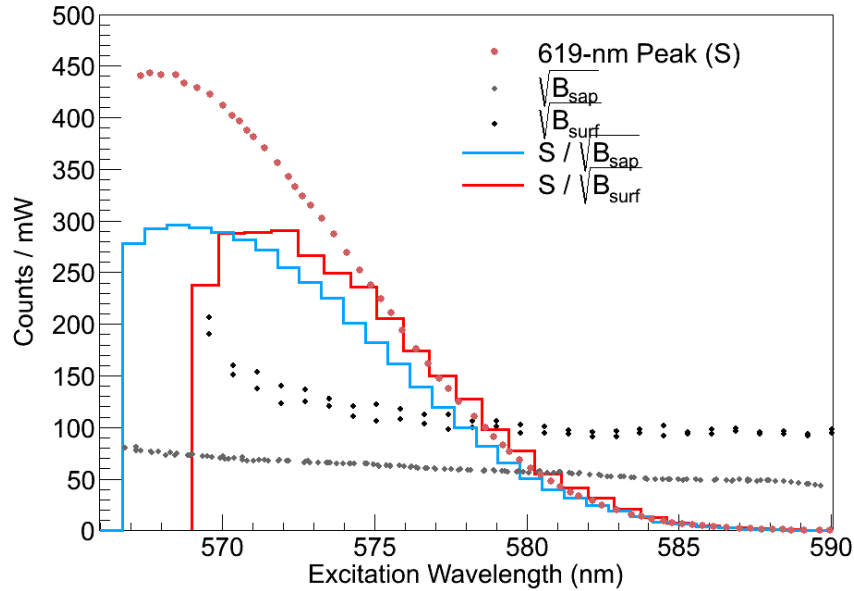


FIGURE 4.8. Optimization of signal to background with the 619-nm fluorescence signal (S) for emission from the surface background (B_{surf} , red) and for the bulk sapphire emission (B_{sap} , cyan).

570 nm, which was used in sensitive imaging experiments, is nearly optimal in both cases, although the bulk sapphire background contribution was small in these experiments.

CHAPTER 5

RESULTS: SPECTROSCOPY

The spectroscopy of Ba in SXe was studied in detail beyond that reported in two previous theses [36, 37], with the goal of imaging single Ba atoms. Emission and excitation spectra are analyzed in Sec. 5.1, with particular interest in the 619-nm peak in Sec. 5.2. Studies of temperature and bleaching effects in Sections 5.3 and 5.4 aid in determining optimal conditions for observation. Finally, candidate emission lines for Ba⁺ in SXe are discussed in Sec. 5.5.

5.1. EXCITATION AND EMISSION OF BA IN SXE

Deposits of Ba in SXe absorb primarily between 540 nm and 570 nm. An absorption spectrum, obtained by observing absorption of white light by a large Ba deposit at 10 K, is shown in Fig. 5.1. Significant broadening, as well as a 4-nm redshift of the central peak, occur relative to the vacuum $6s^2 \ ^1S_0 \rightarrow 6s6p \ ^1P_1$ absorption value of 553.5 nm. Initial absorption and emission spectra was done with the Ba getter source [20, 36, 37], which is expected to produce neutral Ba with minimal Ba⁺. The emission spectrum in Fig. 5.1 was obtained by 557-nm excitation of a Ba⁺ deposit, made at 45 K and observed at 11 K. Observation of the same 577- and 591-nm fluorescence peaks from Ba getter deposits demonstrates that these peaks are emission of neutral Ba. Therefore some neutralization of the ions takes place during the deposit [20, 36, 37]. The fraction of ions neutralized has not yet been determined.

Emission spectra, scaled by laser power, of a Ba⁺ deposit made at 44 K and observed at 11 K are shown in Fig. 5.2(a) for a few different excitation wavelengths. The 577- and 591-nm peaks are clear at all three wavelengths, with varying strength. Peaks at 570 nm

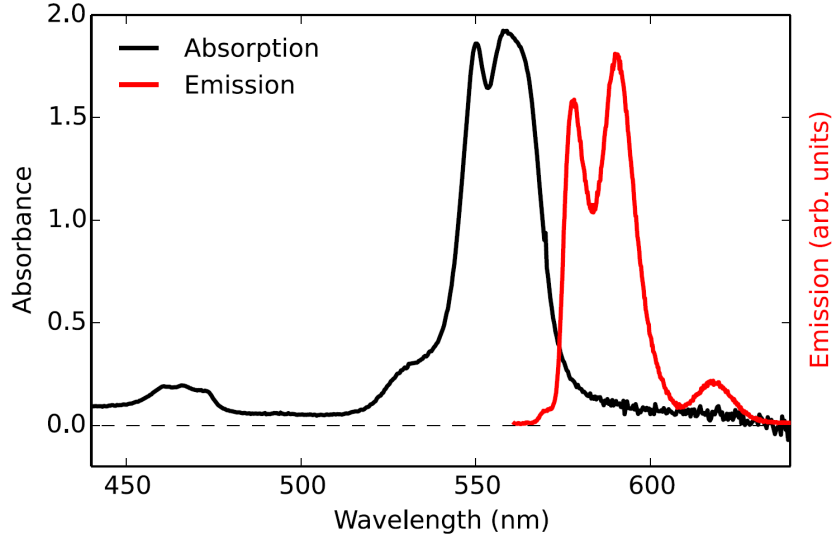


FIGURE 5.1. Absorption and emission spectra of neutral Ba in SXe. The absorption is of a Ba getter deposit at 10 K, and the emission is of a (neutralized) Ba⁺ deposit, deposited at 45 K and observed at 11 K with 557 nm excitation. From [20].

and 601 nm, first reported here, are both clear at 546-nm excitation. The 619-nm peak is stronger at higher wavelength, and the 670-nm peak is clear at 556-nm excitation.

Excitation spectra, shown in Fig. 5.2(b), were produced by scanning the dye laser and measuring the magnitude of each fluorescence peak vs. excitation wavelength. For each frame, the spectrum was fit with a sum of peak-specific fit functions, where function shape parameters were fixed (centers and widths) and magnitudes were allowed to float. Fitting is described in Section 4.1.1. Since the dye laser power varies over the tuning range, fluorescence counts at each excitation wavelength are scaled to the laser power in that frame. Since signal levels are dependent on the deposit size, the absolute scale is arbitrary. Thus, curves were scaled for visibility on the same plot. The discontinuity around 566 nm for the 619- and 670-nm peaks is the boundary between the scan range of different laser dyes. R6G dye was used for higher wavelengths and R110 for lower wavelengths. Bleaching, discussed in Sec. 5.4, was prevented from occurring in the 570-, 577-, 591-, and 601-nm peaks during

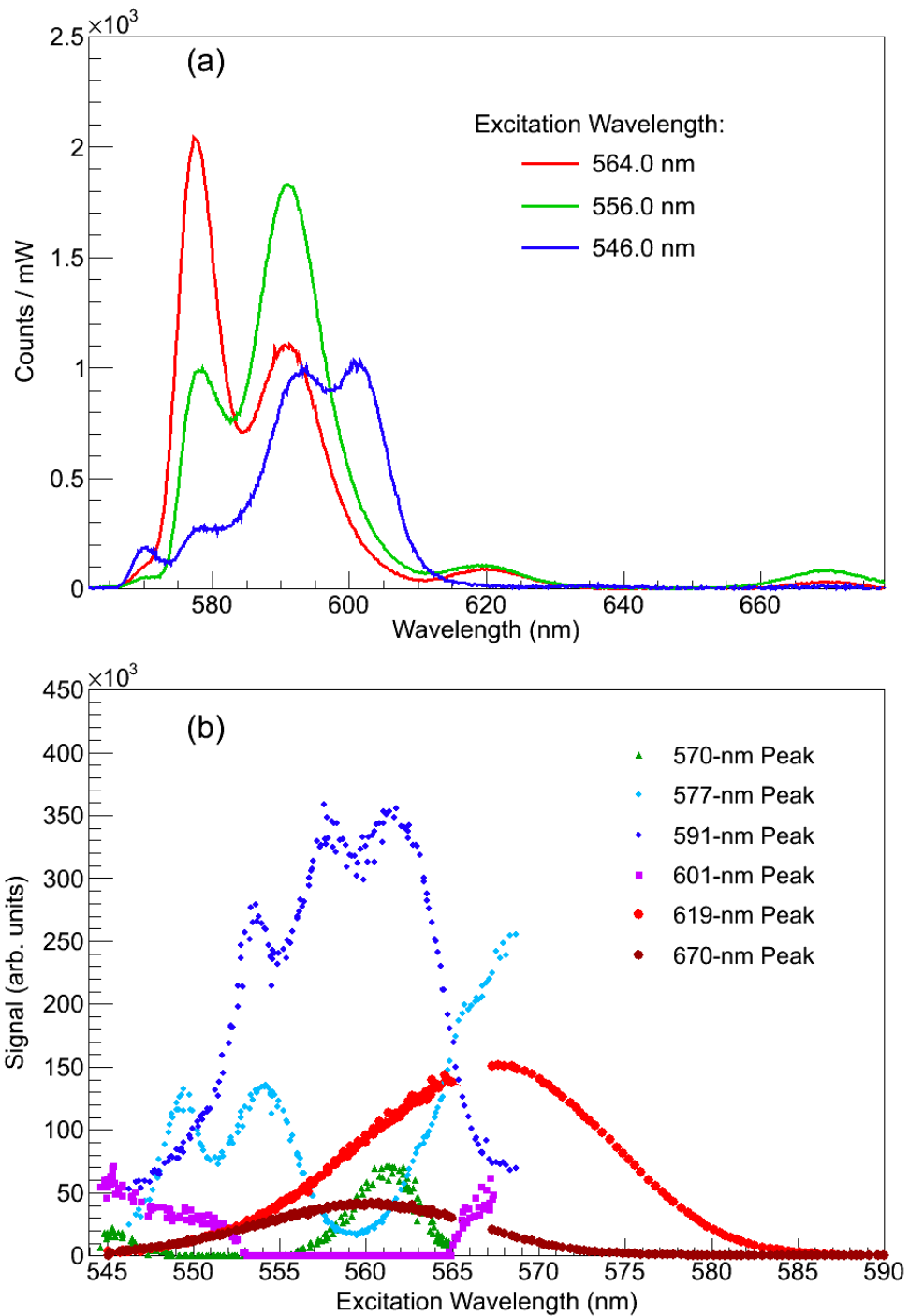


FIGURE 5.2. (a) Fluorescence spectra for a few different excitation wavelengths, and (b) excitation spectra for all observed Ba fluorescence peaks. Exposures are 1 s.

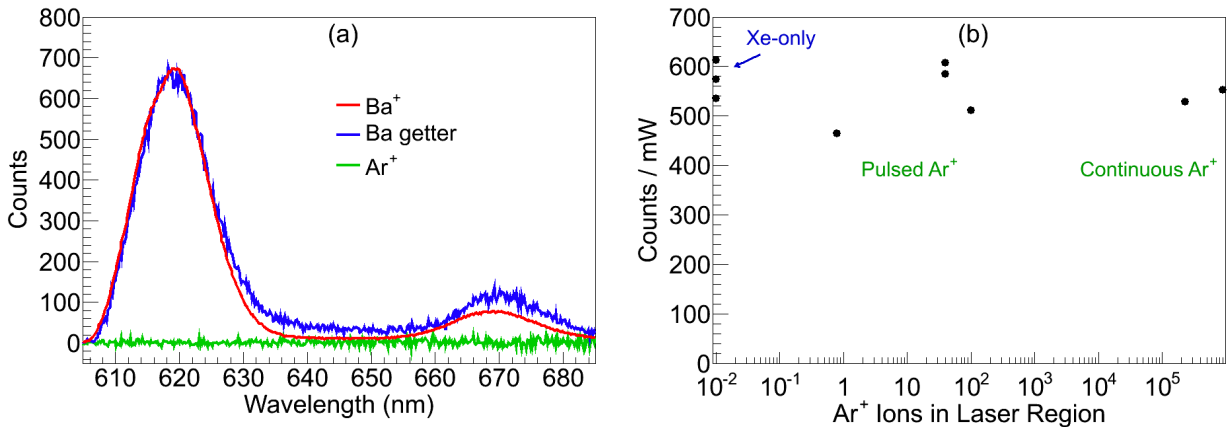


FIGURE 5.3. Comparison of signal observed for deposits with the Ba^+ ion beam (red), Ba getter (blue), and Ar^+ ion beam (green) (a), and signal through 620-nm band-pass from deposits of small to large numbers of Ar^+ ions in SXe.

excitation spectrum scans by using low laser intensities. For those peaks, maximal laser power was 0.1 mW, and the laser radius was $w = 7 \text{ mm}$ with no focusing. The scans for the 619- and 670-nm peaks, which bleach only at much higher intensities, were done with the laser somewhat focused to radii of $w = 1000 \mu\text{m}$ in the R110 dye range, and $w = 200 \mu\text{m}$ in the R6G dye range, with maximal laser powers of 10 mW and 100 mW, respectively.

5.2. 619-NM PEAK ATTRIBUTION

The 619-nm peak, as well as the 670-nm peak, was demonstrated to be related to neutral Ba by a few further tests. The spectra of a large Ba^+ deposit and a deposit made with the Ba getter are compared in Fig. 5.3(a). The 619-nm and 670-nm peaks are observed with both sources with similar shapes. Since the getter produces only neutral Ba, these peaks are attributed to neutralized Ba^+ ions. Observation of a deposit of Ar^+ of similar energy and charge in SXe is also shown in Fig. 5.3(a). The lack of fluorescence in the Ar^+ deposit eliminates a matrix-damage-related source of the fluorescence, such as color centers. Imaging experiments of Ar^+ deposits were also performed, with both pulsing and

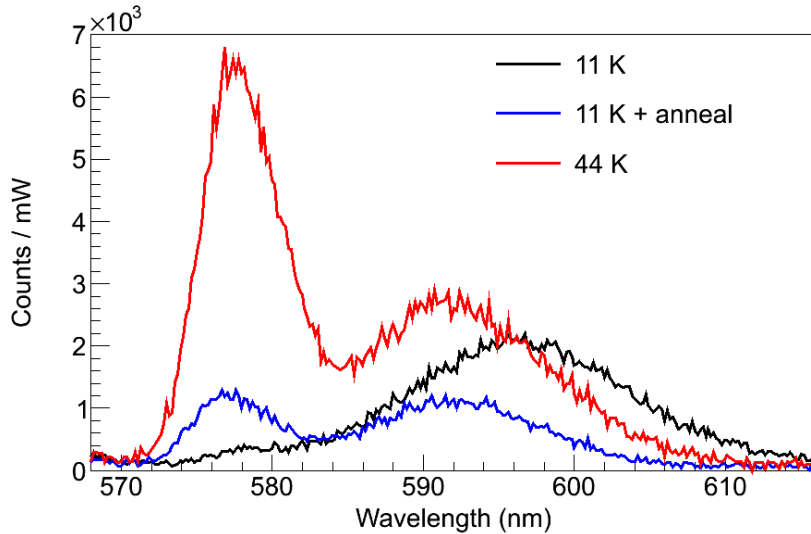


FIGURE 5.4. Spectra of peaks around 590 nm of a Ba^+ deposit made at 11 K before and after annealing to 39.4 K, and one made at 44 K. All observations are at 11 K. Both Ba^+ deposits are 15 s, however the 44 K deposit is scaled slightly to account for different ion current. Laser power was about 0.1 mW with an unfocused beam radius of $w = 7.056$ mm, at 566 nm wavelength.

continuous ion beams. Summed counts/mW from these deposits are shown to be consistent with background in Fig. 5.3(b). To be similar to Ba imaging experiments discussed in Sec. 6.2, the focused dye laser was at 570 nm, and a 620-nm band-pass filter was used on the fluorescence.

5.3. ANNEALING/TEMPERATURE DEPENDENCE

Emission spectra can depend on the thermal history of the deposit, such as the temperature at which it was made, and any annealing of the deposit. Spectra observed at 11 K with different thermal histories are shown in Fig. 5.4. Peak shapes in the annealed deposit look similar to those in the deposit made at 44 K. However, larger signal is observed in the deposit at 44 K. The broader emission around 596 nm in non-annealed 11-K deposits may be due to a higher population of the 601-nm peak, which is not resolved from the 591-nm peak. The deposit temperature dependence of the 619-nm peak is illustrated by images comparing

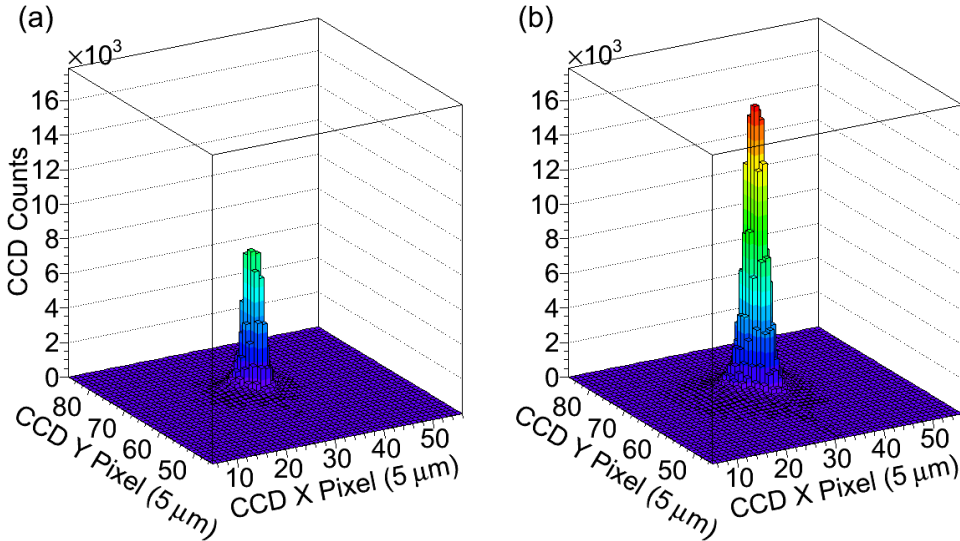


FIGURE 5.5. Images of 619-nm fluorescence in focused 570-nm laser region for deposits made at (a) 11 K and (b) 52 K. Deposits are 3 s of continuous Ba^+ current. Exposures are 0.1 s. Observation is at 11 K.

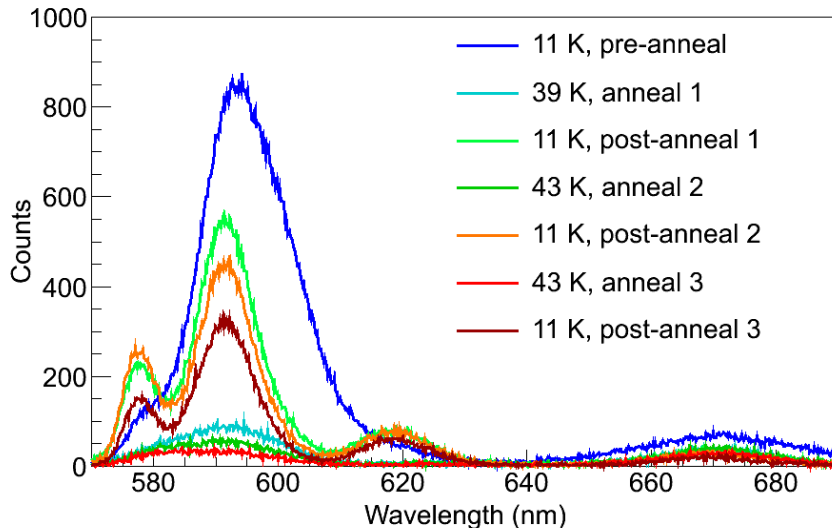


FIGURE 5.6. Spectra of a large Ba^+ deposit through several annealing cycles. The initial deposit was at 11 K. The laser power was about 0.2 mW with an unfocused beam radius of $w = 7.056$ mm, at 564 nm wavelength. [20]

the fluorescence from a focused laser through the 620-nm band-pass filter, shown in Fig. 5.5. The level of 619-nm signal is about 3 \times larger in deposits made at 52 K vs. 11 K. Imaging is described in detail in Chapter 6. These tests guided the standard of depositing at 50 \pm 5 K when observing the 577-, 591-, and/or 619-nm peaks.

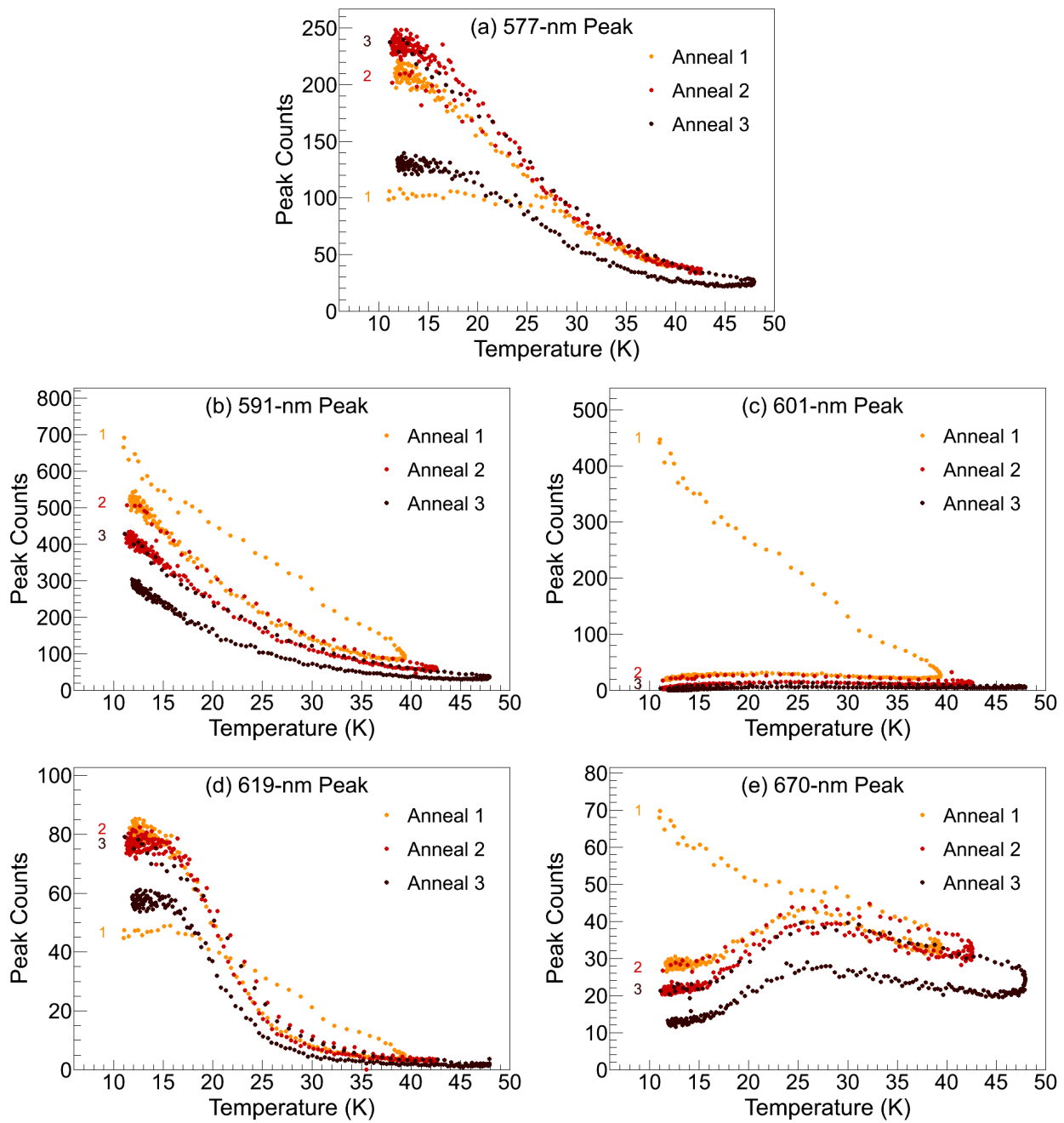


FIGURE 5.7. Fit peak counts for the (a) 577-, (b) 591-, (c) 601-, (d) 619-, and (e) 670-nm fluorescence peaks through three annealing cycles of the Ba^+ deposit made at 11 K. “1”, “2”, and “3” mark the beginning of each anneal cycle. The laser power was about 0.2 mW with an unfocused beam radius of $w = 7.056$ mm at 564 nm wavelength.

Fluorescence spectra with 564 nm excitation through several annealing cycles for a deposit made at 11 K are shown in Fig. 5.6. The initial exposure shows significant 591- and 601-nm (unresolved from one another) emission, with some 577-nm emission. All peaks are reduced at the high temperature ends of the anneal cycles. The return to lower temperatures results in an overall increase for some peaks, e.g. the 577- and 619-nm peaks, and an overall loss of others, e.g. the 670-nm peak.

Fit peak counts (fitting is described in Sec. 4.1) vs. temperature are shown in Fig. 5.7. The 577-nm and 619-nm peaks gained significantly with the first anneal, suggesting that they are due to more stable matrix sites. Both of these peaks remained about the same after the second cycle (small gain in 577-nm), and both had loss after the third cycle, which reached the higher temperature of 48 K. The 591-nm had moderate loss with each cycle. The 601-nm peak had nearly complete loss in the first anneal cycle. The 670-nm peak had significant loss, with more loss after each succeeding anneal cycle, each of which reached higher a temperature than the last.

Aside from matrix site changes, direct temperature dependence of fluorescence can be observed in annealing cycles. The 577-, 591- and 619-nm peaks have their highest amplitude at 11 K. The 577-nm and 619-nm peaks reach a plateau at 11 K, while the 591-nm may benefit from even lower temperatures. This suggests that a probe in nEXO may need to be extracted from the liquid chamber and moved to a separate evacuated chamber in order to cool to 11 K or below for most efficient observation.

5.4. BLEACHING

Decay of fluorescence with laser exposure, or bleaching, was observed for all six Ba fluorescence peaks. Examples of bleaching spectra are shown in Fig. 5.8, with excitation at

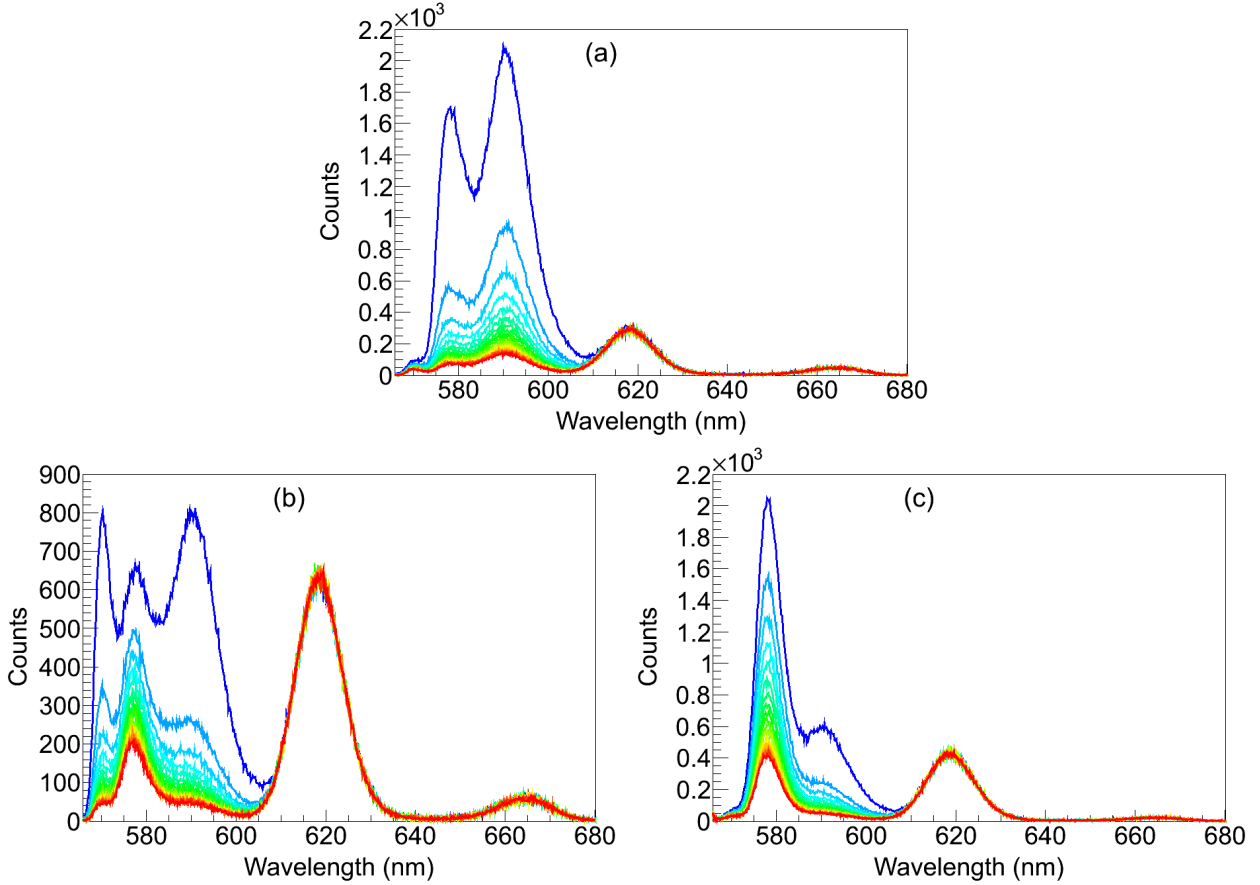


FIGURE 5.8. Bleaching Ba emission peaks with excitation at (a) 556.9 nm, (b) 562.6 nm, and (c) 566.3 nm. Laser power and exposure times are (a) 1.3 mW and 1 s, (b) 7.5 mW and 0.2 s, and (c) 5.8 mW and 0.2 s. Every tenth exposure is shown, beginning with the second in the darkest blue, ending with the darkest red. Each is a 5-s continuous Ba^+ deposit at 45 K, observed at 11 K. [20]

(a) 556.9 nm, (b) 562.6 nm, and (c) 566.3 nm, using a semi-focused laser of radius $w = 1000 \mu\text{m}$. Each curve is the Ba emission spectrum at different points in time. Bleaching is seen to be rapid for the 570-, 577-, 591-, and 601-nm peaks. Negligible bleaching is observed for the 619- and 670-nm peaks in Fig. 5.8. Nevertheless, even for these lines, some small bleaching was observed with the much higher intensity of a focused beam.

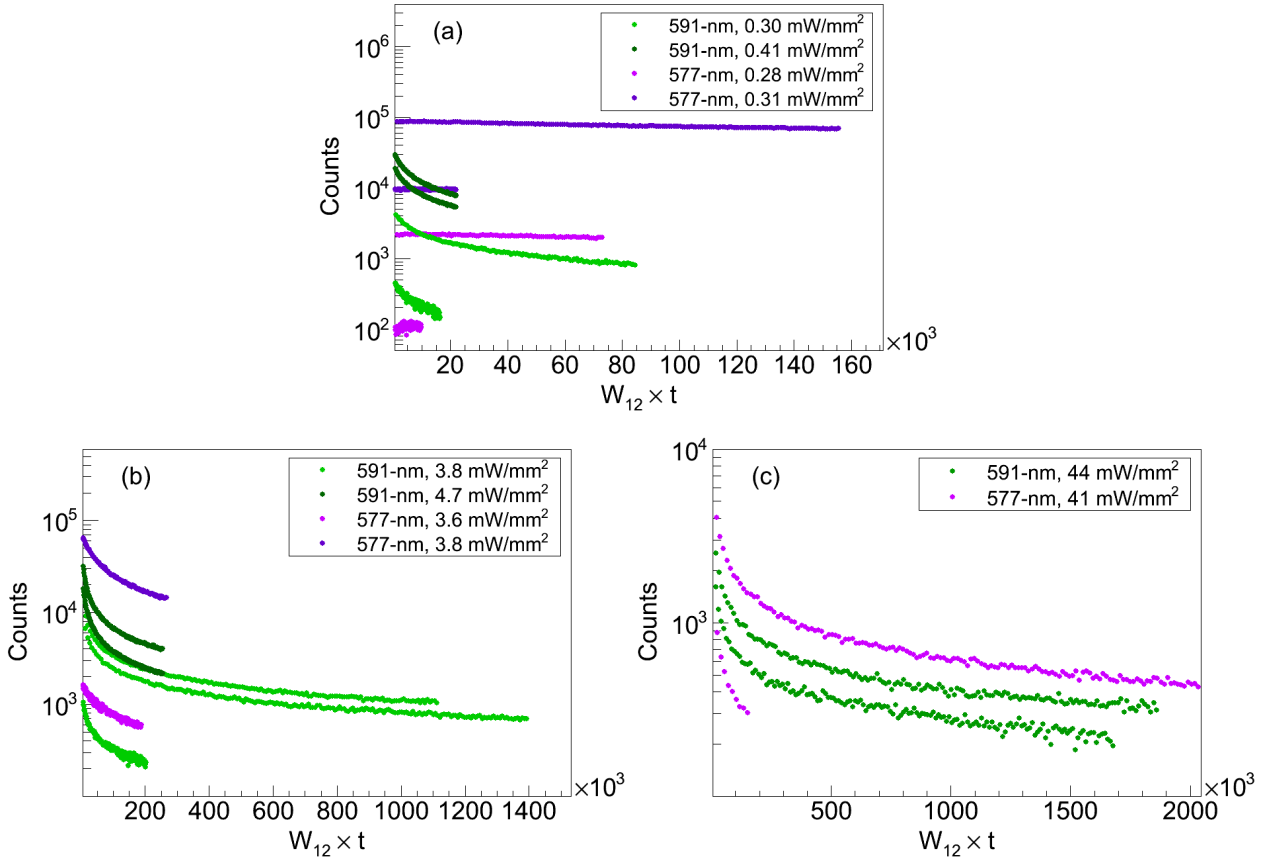


FIGURE 5.9. Fluorescence vs. number of excitations for three orders of magnitude (a,b,c) in laser intensity, for the 577-nm (purple) and 591-nm (green) fluorescence peaks. The deposits were continuous Ba^+ at 45 K, observed at 11 K, and exposures were 0.2 or 2 s.

5.4.1. BLEACHING OF THE 577- AND 591-NM PEAKS

The integrated counts for different peaks in each spectrum were determined by fits to the spectra, as described in Sec. 4.1. Integrated counts vs. number of excitations ($W_{12} \times t$) are shown in Fig. 5.9 for both the 577-nm (purple) and 591-nm (green) fluorescence peaks, with laser intensities varying by two orders of magnitude from about 0.3 mW/mm^2 (a) to about 40 mW/mm^2 (c). Intensities for each run are listed in the legends. The excitation wavelengths used were 566.3 nm for the 577-nm peak and 562.6 nm for the 591-nm peak. Bleaching is more rapid in the 591-nm peak than the 577-nm peak when low intensity is used

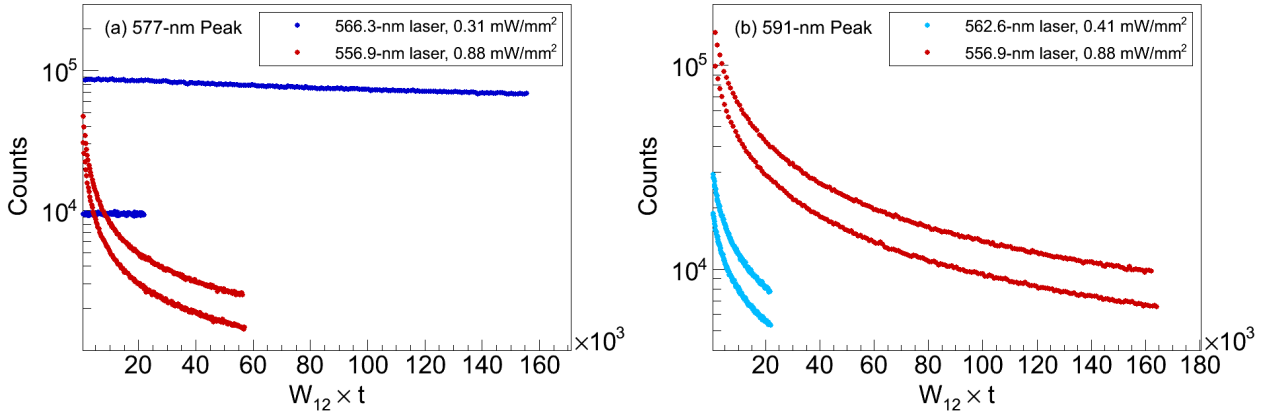


FIGURE 5.10. Fluorescence vs. number of excitations with different excitation wavelengths for (a) the 477-nm peak, and (b) the 591-nm peak. Deposits are continuous Ba^+ at 45 K, observed at 11 K.

(a). For medium (b) and high (c) intensity, bleaching rates are similar. In order to calculate the excitation rate W_{12} for each run according to Eq. 13, the cross section $\sigma(\nu)$ was calculated using the integral of the corresponding excitation spectrum (Fig. 5.2), as explained in Sec. 2.4. Cross sections at maximal excitation were calculated to be $5.2 \times 10^{-19} \text{ m}^2$ for the 577-nm emission peak, and $3.4 \times 10^{-19} \text{ m}^2$ for the 591-nm emission peak.

Comparisons of bleaching with different excitation wavelengths are shown in Fig. 5.10 for (a) the 577-nm peak, and (b) the 591-nm peak. In the case of the 577-nm peak (a), the excitation wavelengths (566.3 and 556.9 nm) correspond to different peaks in the excitation spectrum (Fig. 5.2). Very different bleaching rates were observed. In the case of the 591-nm peak (b), the excitation wavelengths (562.6 and 556.9 nm) correspond to neighboring peaks in the triplet structure of the excitation spectrum. The bleaching rates are similar, with a somewhat faster rate for the 556.9-nm excitation, which had about $2 \times$ the intensity.

Ultimately, these studies suggested the usage of the 577-nm peak in imaging small numbers of atoms due to its lower bleaching rate, especially with excitation on the high-wavelength end of the range studied. Imaging of Ba atoms using a combination of the 577-

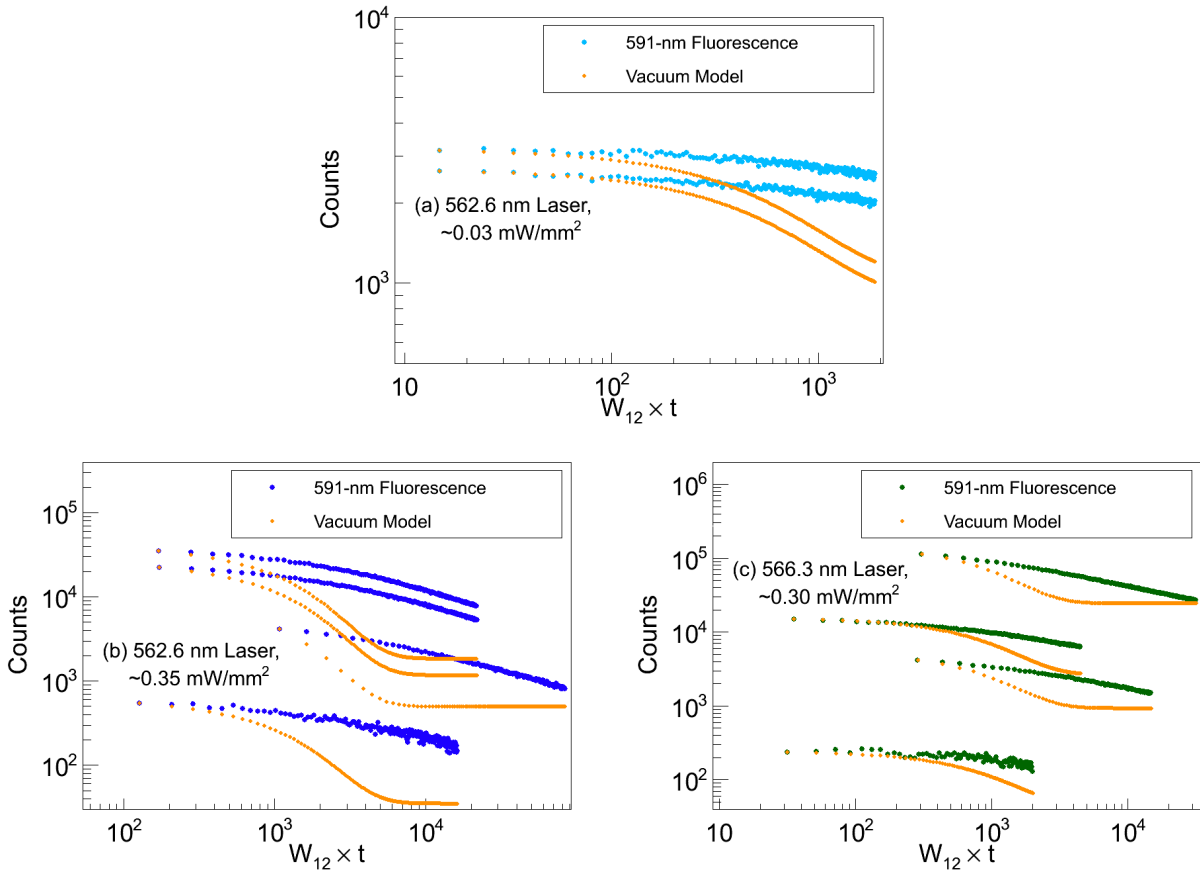


FIGURE 5.11. Vacuum model (orange) comparisons to 591-nm fluorescence with excitation at 562.6 nm (a,b), and 566.3 nm (c). Deposits were continuous Ba^+ at 45 K, observed at 11 K.

and 591-nm peaks with excitation at 566 nm, via a band-pass filter passing 573 - 599 nm FWHM, is discussed in Sec. 6.1.

A numerical model of fluorescence vs. time for a 5-level system of Ba in vacuum is described in Sec. 2.2. Using the Ba vacuum transition parameters given in Table 2.1, the model is compared to bleaching data of the 591-nm peak in Fig. 5.11. W_{12} in each model is calculated in the same way as its respective data run. Each model is normalized to the beginning of its respective data set. Agreement between the model and data is observed for the first ~ 100 excitations with on-resonance 562.6-nm excitation (a), at which point the vacuum model begins more rapid decay. With the same 562.6-nm excitation and $10\times$ laser

power (b), where the first point is above 100 excitations, this deviation begins immediately. With the off-resonance excitation wavelength of 566.3 nm (c), the model agrees with data for the first \sim 200 excitations. The less rapid decay in the data vs. the model between \sim 100-200 and \sim 5,000 excitations indicates a lower optical pumping rate in the SXe vs. in vacuum. However, the steady state level reached by the vacuum model above \sim 5,000 excitations is not reached by the date. Rather, it appears that bleaching continues beyond $3\text{-}5 \times 10^4$ excitations.

The fluorescence efficiency ϵ_f is the total number of photons emitted per photons absorbed (Sec. 2.4). This was measured in the first of exposure, before substantial bleaching has occurred, and is plotted vs. W_{12} in Fig. 5.14 for the 577- and 591-nm peaks. Fluorescence efficiency is fairly constant below $W_{12} \approx 100 \text{ s}^{-1}$, and begins to decline at higher W_{12} . This is explained by the effect of greater bleaching at higher W_{12} in the first exposure. Using the lowest values of W_{12} , ϵ_f is measured to be about 2×10^{-3} for the 591-nm peak with 562.6-nm excitation, and 5×10^{-4} for the 577-nm peak with 566.3-nm excitation. The bleaching model does not explain such small fluorescence efficiency. However, these values assume that 100% of deposited Ba⁺ ions are observable by these fluorescence peaks, which may not be the case.

5.4.2. BLEACHING OF THE 619-NM PEAK

On the scale of bleaching intensity in Fig. 5.8, the 619-nm peak does not bleach at all. Nevertheless, it does bleach somewhat at much higher laser intensities. At a few mW of 570-nm excitation, bleaching is observed when the laser is focused. This indicates a significant deviation from the vacuum model, particularly that decays from D states are competitive with decays into D states. 619-nm fluorescence counts, integrated from the image of a focused laser region with $w_x \times w_y = 2.06 \mu\text{m} \times 2.66 \mu\text{m}$, are plotted vs. number of excitations in Fig. 5.12 for three laser powers. W_{12} incorporates the cross section for the 619-nm peak,

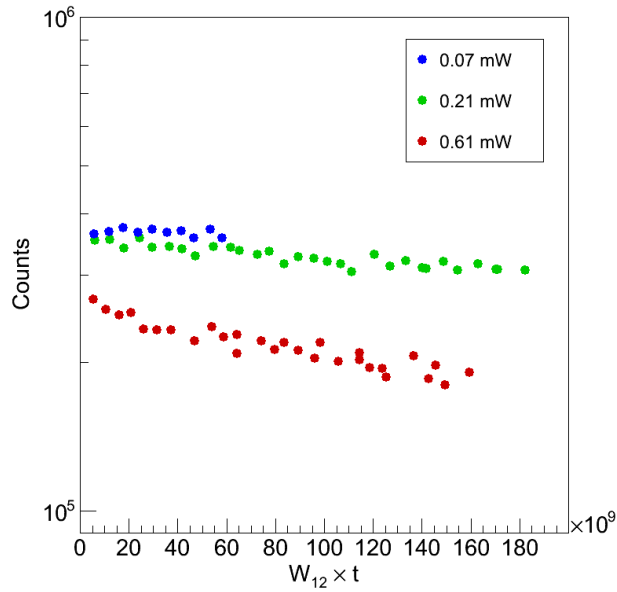


FIGURE 5.12. 619-nm fluorescence counts vs. number of excitations for three laser powers. Excitation is 570 nm focused to $w_x \times w_y$ beam radii of $2.06 \mu\text{m} \times 2.66 \mu\text{m}$. All one deposit of 5 s continuous Ba^+ at 50 K, observed at 11 K from low to high laser intensity.

calculated to be $3.1 \times 10^{-19} \text{ m}^2$, as is done for the 577- and 591-nm peaks in Sec. 5.4.1. Even with the higher laser power of 0.61 mW, 70% of the signal remains after 160×10^9 excitations, many orders of magnitude beyond the bleaching time of the 577- and 591-nm peaks. The linearity in the semi-log plot indicates a single exponential decay, indicating that a simple 3-level model, solved in previous theses [37, 36], describes the bleaching rate over this range of excitations.

5.4.3. RE-PUMPING

Re-pumping of optically pumped Ba could require up to three additional lasers, one for each of the populated metastable D states. The optimal excitation wavelength for each transition would need to be discovered using tunable lasers in the infrared. However, mixing of states and/or alterations in transition rates for Ba in the Xe matrix could lower the number of lasers needed. Re-pumping was attempted, with low-cost and on-hand lasers, for

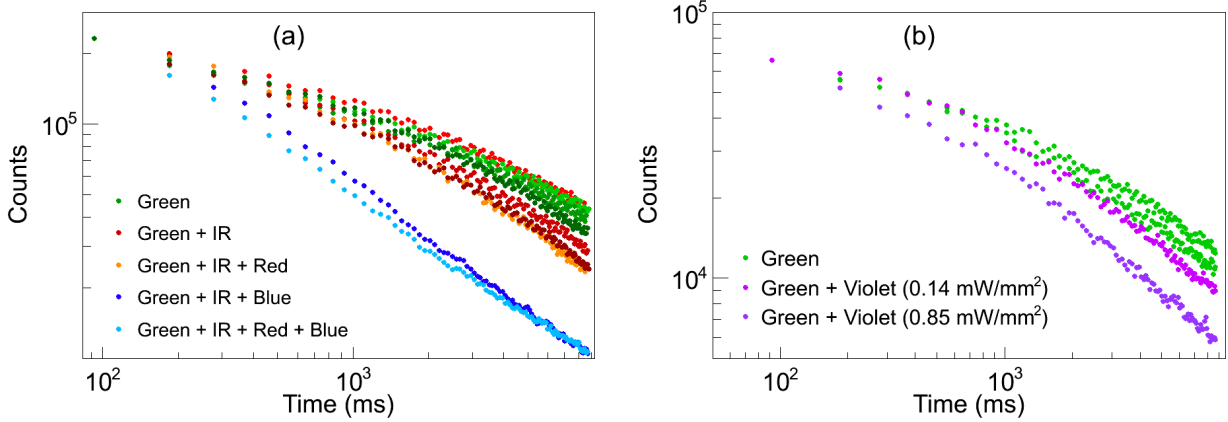


FIGURE 5.13. Bleaching data with and without additional re-pump lasers at (a) 1064 nm (~ 18 mW/mm 2), 1550 nm (~ 9 mW/mm 2), 657 nm (~ 9 mW/mm 2) and 472.64 nm (~ 14 mW/mm 2), and (b) 406 nm. All curves have 1.4 - 1.5 mW of 555-nm excitation, semi-focused to around 600- μ m beam radius. Deposits are (a) 6 s and (b) 3 s continuous Ba $^+$ at 11 K.

the direct infrared transitions as well as the higher-level transitions shown in Fig. 2.1. A 1550-nm diode laser and a 1064-nm Nd:YAG laser were used to attempt direct re-pumping from the ^1D and ^3D states, respectively. A 657-nm diode laser was used to attempt excitation from the ^3D states into the higher-level $5d6p\ ^3\text{D}_1$ $^\circ$ state, similar to the red laser utilized in the Ba MOT in [27] for the $6d5d\ ^3\text{D}_1$ state. The blue C480 dye laser and 406-nm Kr ion laser were used to attempt excitation from the ^1D state into the higher-level states $6s7p\ ^1\text{P}_1$ $^\circ$ and $6s8p\ ^1\text{P}_1$ $^\circ$, respectively.

591-nm fluorescence counts vs. time for several Ba $^+$ deposits made and observed at 11 K are shown in Fig. 5.13 for several laser combinations, all of which were combined by dichroic filters into the same path. Each curve is a separate deposit, all of which are scaled to begin at the same point for comparison. In Fig. 5.13(a), green-only (555 nm) excitation (i.e., no re-pump lasers) is shown along with green + IR (1064 nm and 1550 nm), green + IR + red (657 nm), green + IR + blue (C480 dye at 472.64 nm), and green + IR + red + blue. Increased bleaching was observed by inclusion of these re-pump lasers, especially with the

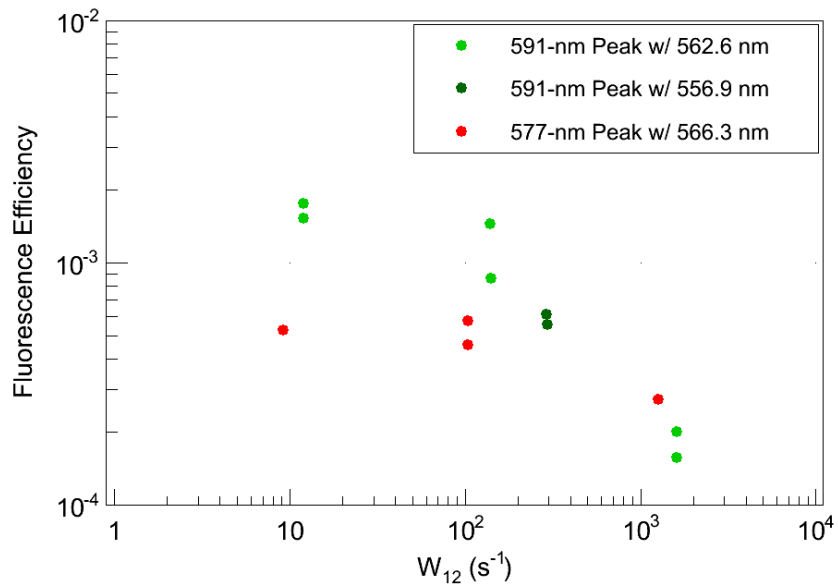


FIGURE 5.14. Fluorescence efficiency vs. W_{12} using the first exposure frame for the 577-nm (red) and 591-nm (green) peaks. Deposits are 5 s continuous Ba^+ at 50 K, observed at 11 K with laser radius $w = 1000 \mu\text{m}$.

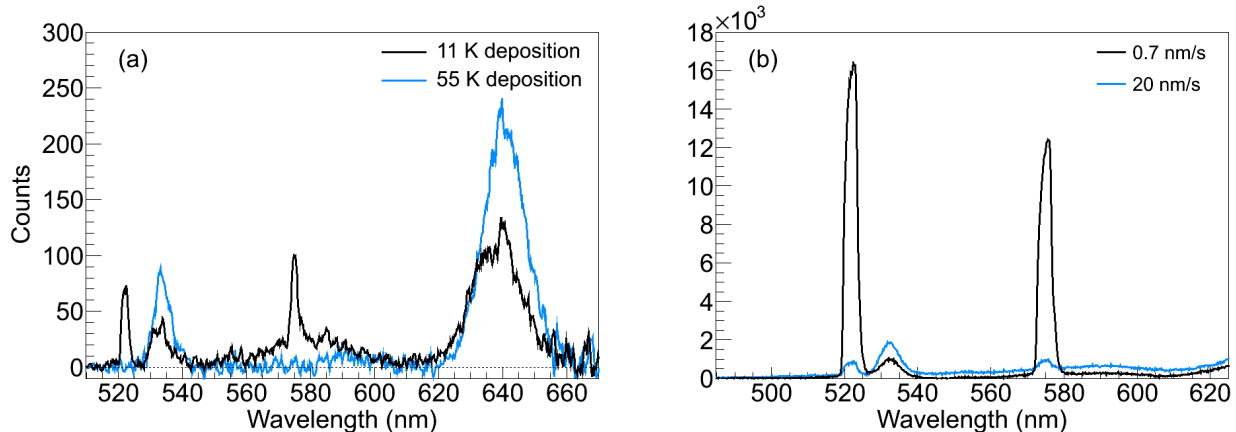


FIGURE 5.15. Comparison of Ba^+ deposits made at (a) 55 K vs. 11 K, and (b) 20 nm/s vs. 0.7 nm/s.[20]

blue laser. In Fig. 5.13(b), green-only is shown again along with green + violet (Kr ion laser at 406 nm) at two different powers. Increased bleaching was observed with the violet laser, with more bleaching at the higher violet laser power.

5.5. BLUE EXCITATION / CANDIDATE Ba^+ LINES

Blue excitation of Ba^+ in SXe was first explored in the thesis of Shon Cook. A set of sharp emission peaks were observed at 522, 575, 637, 712, and 814 nm, in decreasing emission strength. These peaks were attributed to emission from different vibrational states of a molecule composed of Ba and one or more H atoms, that is denoted as BaH_x [36]. This assignment is supported by two additional experiments in this thesis. Firstly, a reduction of those peaks is observed in deposits made at 50 K, well above the H_2 freezing temperature of 12 K, vs. deposits made at 11 K, as shown in Fig. 5.15(a). Secondly, the peaks are much stronger in deposits made with lower leak rates, as shown in Fig. 5.15(b), for deposits made at 11 K.

Several additional emission peaks are prominent in deposits made at 50 ± 5 K and observed at 11 K. Representative spectra at four blue excitation wavelengths are shown in 5.16(a). Peaks at 532, 553, 568, 592, 635, and 669 nm are observed. Excitation spectra for these peaks are shown in 5.16(b). The largest peaks at 532 nm and 635 nm have identical excitation spectra, indicating that they are due to the same excitation transition. It is possible that the 532- and 635-nm peaks are emission from the $P \rightarrow S$ and $P \rightarrow D$ transitions, respectively, of matrix-isolated Ba^+ ions. However, matrix effects would need to be responsible for the higher number of counts observed in the 635nm peak vs. the 532-nm peak, whereas the $P \rightarrow S$ transition is about $4\times$ more likely than the $P \rightarrow D$ transition in vacuum. Further study of these emission peaks is needed to assign them to Ba^+ .

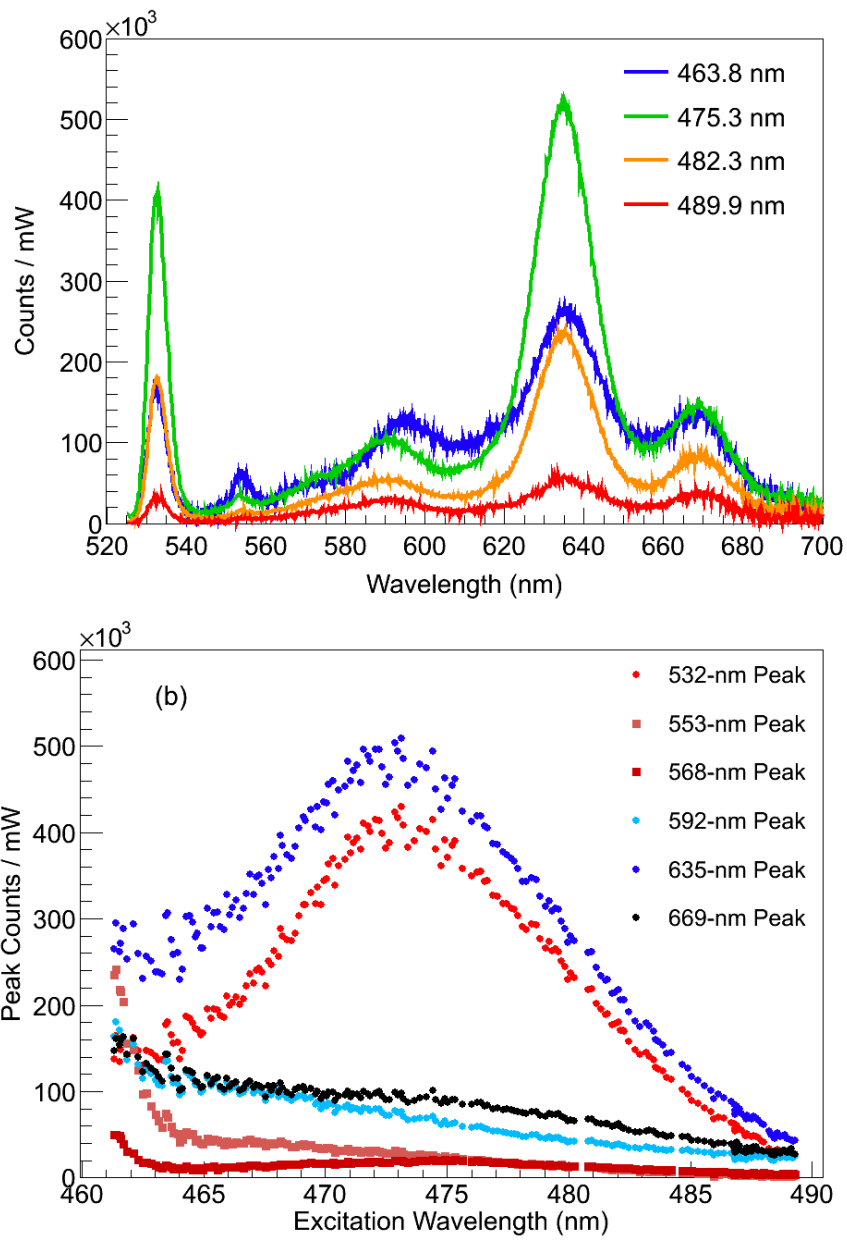


FIGURE 5.16. (a) Background-subtracted fluorescence spectra for a few different excitation wavelengths, and (b) excitation spectra for peaks observed through C480 dye range.

CHAPTER 6

RESULTS: IMAGING

Results from Ba spectroscopy presented in Chapter 5 were used to determine the best conditions for imaging small numbers of Ba atoms in SXe. Optimum excitation wavelengths were determined by studying the excitation spectra of the signal as well as the background. Bleaching studies determined optimum laser intensity to be used. Deposits made at 50 ± 5 K produced more Ba fluorescence signal than those made at 11 K. Based on these considerations, an image of Ba atoms emitting at 577 and 591 nm is presented in Sec. 6.1 at the level of ≤ 2700 atoms instantaneously exposed. Images of Ba atoms emitting at 619 nm down to the single-atom level are then presented in Sec. 6.2. Initial scanned images of Ba^+ deposits are presented in Sec. 6.3.

6.1. IMAGING 577- AND 591-NM FLUORESCENCE

First attempts at imaging small numbers of Ba atoms in a focused laser region were done with the 577- and 591-nm Ba fluorescence peaks together using a 586-nm band-pass filter, which passes 573 - 599 nm FWHM. This filter has a 2" diameter, resulting in a nominal collection efficiency of 8.4×10^{-3} , $4\times$ the efficiency given in Table 3.1. An image of ≤ 2700 atoms instantaneously in the laser region is shown in Fig. 6.1 for a 100-s exposure with $0.02 \mu\text{W}$ of 566-nm excitation. The laser was focused by the bi-convex lens, resulting in a beam radius of $5 \mu\text{m}$, as discussed in Sec. 3.4. With this spot size, the factor between total and instantaneously atoms exposed is 3, as discussed in Sec. 3.7, resulting in ≤ 8300 total atoms exposed. At this low intensity, no bleaching was observed in the four frames observed (frame 1 is shown). Groups of 9 (3×3) CCD pixels have been binned in software to produce

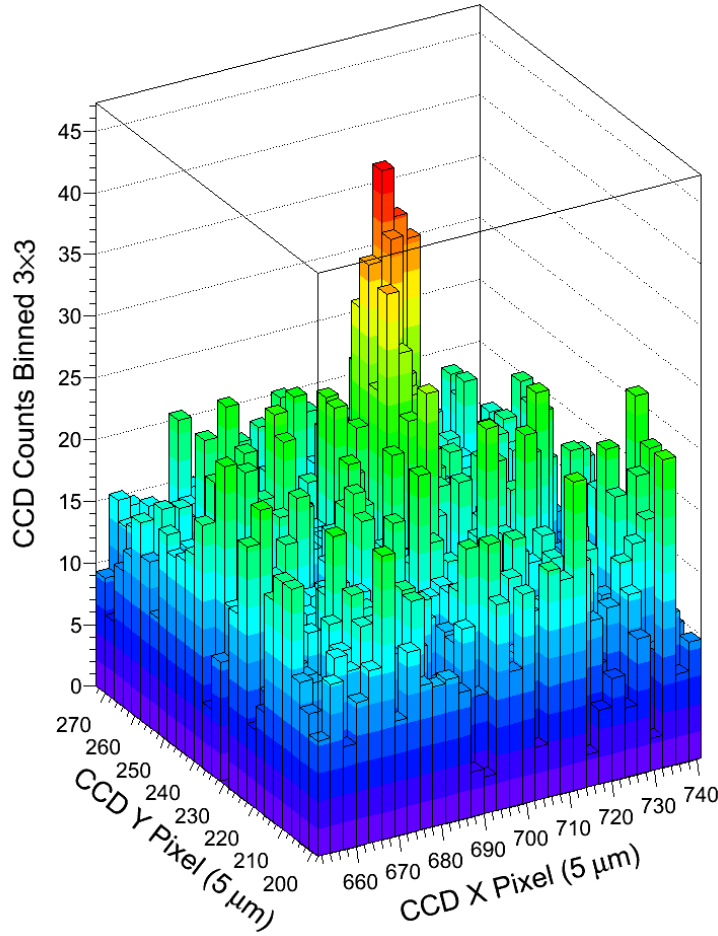


FIGURE 6.1. Image through 586-nm band-pass filter of $\leq 2.7 \times 10^3$ Ba atoms in SXe. 100-s exposure with $.03 \mu\text{W}$ of 566 nm excitation, with laser beam radius of $5 \mu\text{m}$. Sample was deposited at 50 K and observed at 11 K. 3×3 pixel binning was done with software.

the peak shown. Detection of single Ba atoms in these sites may require several re-pump lasers, as discussed in 5.4. As a result of low total exposure, neither the sapphire nor the surface backgrounds are present in these images.

6.2. IMAGING 619-NM FLUORESCENCE

Raw images of Ba^+ deposits and their preceding and succeeding Xe-only deposits are shown in Fig. 6.2 for deposits of (a) ≤ 49 (≤ 230), (b) ≤ 4 (≤ 20), and (c) ≤ 1 (≤ 5) instantaneous (total) number of Ba atoms exposed. Exposures are 60 s with around 0.24 mW

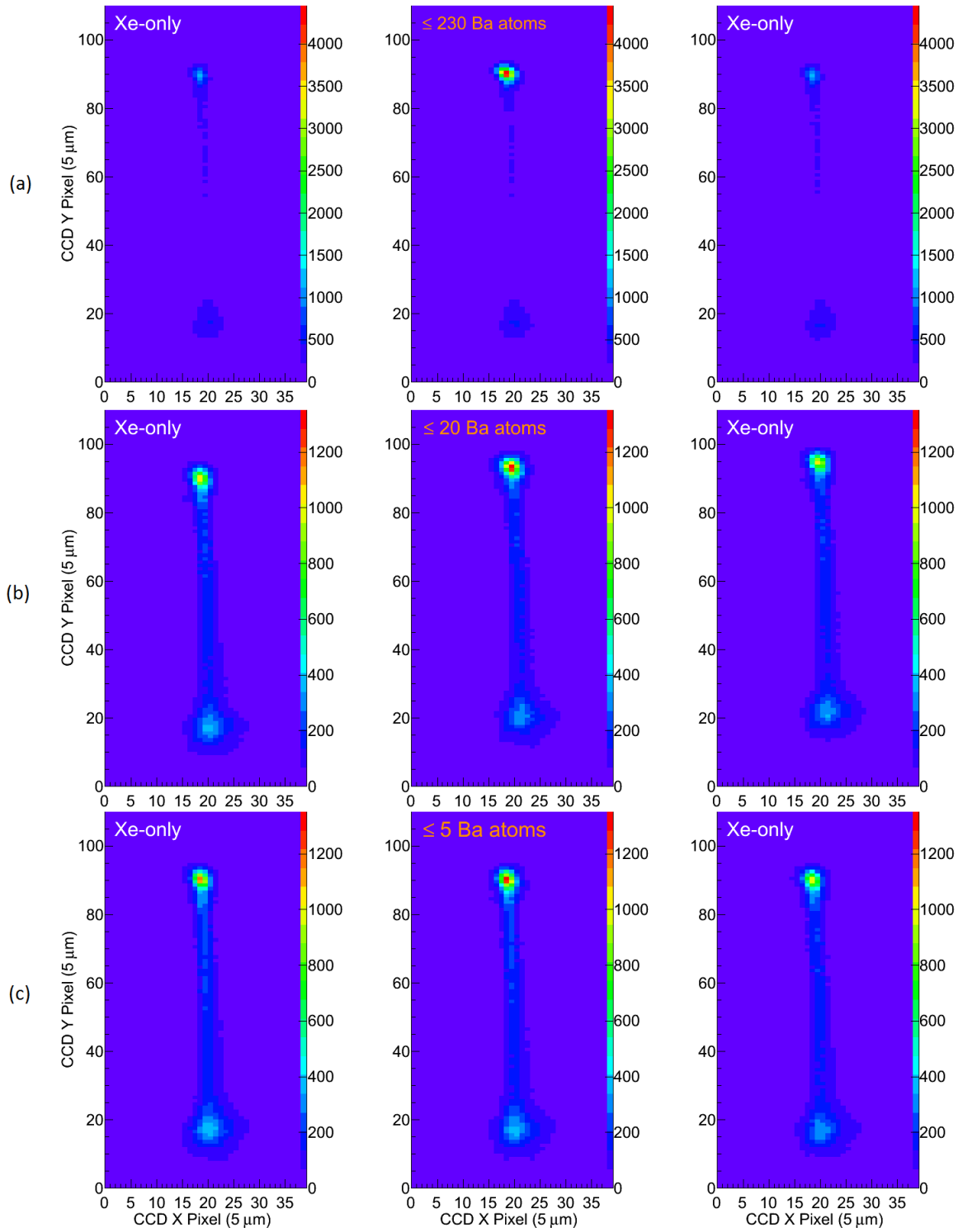


FIGURE 6.2. Raw images through 620-nm band-pass filter of three Ba^+ deposits yielding (a) ≤ 49 , (b) ≤ 4 , and (c) ≤ 1 Ba atoms, with their preceding and succeeding Xe-only deposits. Samples were deposited at 50 K and observed at 11 K.

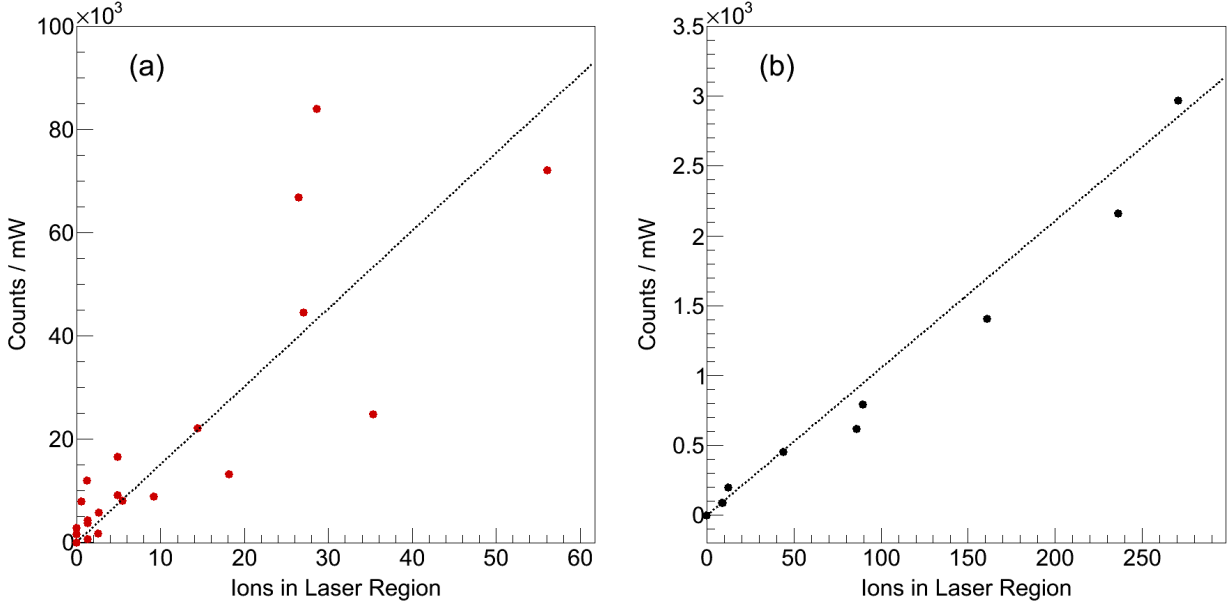


FIGURE 6.3. 619-nm signal, scaled by laser power, vs. instantaneous number of Ba^+ exposed by focused laser at 570 nm for experiments with (a) aspherical, and (b) bi-convex laser focusing lenses. Exposure times are (a) 60 s, and (b) 3 s.

of 570 nm excitation focused to $w_x \times w_y = 2.06 \mu\text{m} \times 2.66 \mu\text{m}$ with the aspherical laser focusing lens and astigmatism compensator. Thus the factor between total and instantaneously exposed atoms is 4.7. Signal is distinguishable from background by eye, even with an instantaneous number of exposed atoms at the 1-atom level.

To determine signal level, counts were summed from a 3-pixel \times 3-pixel ($15\mu\text{m} \times 15\mu\text{m}$) region centered on the laser spot in the image. Background was determined by averaging the 3-pixel \times 3-pixel sum of the Xe-only runs before and after each Ba^+ run. Signal and background were scaled to laser power, and then background was subtracted.

The integrated 619-nm fluorescence signal is plotted vs. instantaneous number of ions (upper limit on atoms) exposed in Fig. 6.3 for many deposits in two experiments with two different laser focusing lenses: (a) asphere with astigmatism compensation, and (b) bi-convex. Exposures were (a) 60 s with 0.24 mW laser power, and (b) 3 s with 2 mW laser

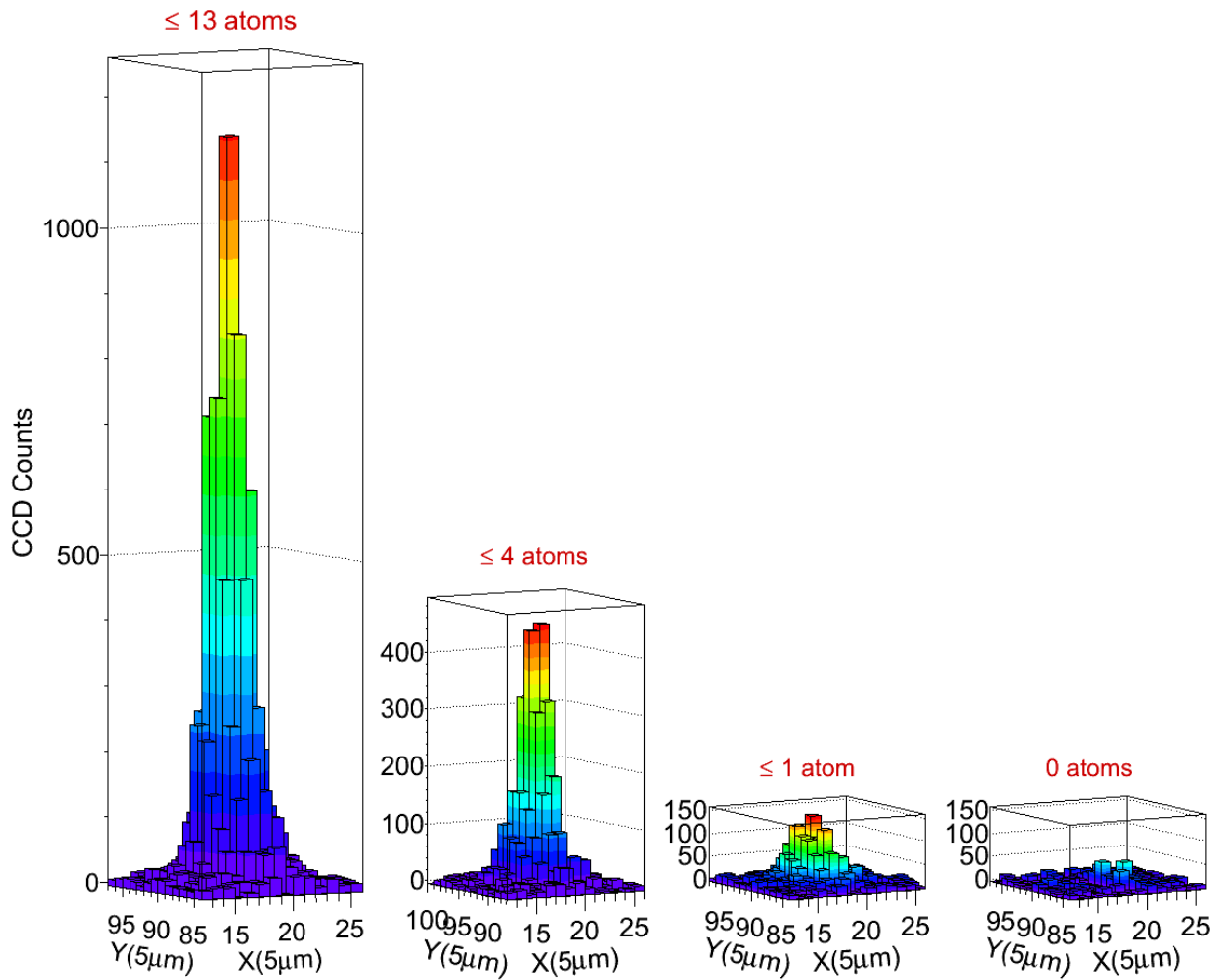


FIGURE 6.4. Subtracted images of 619-nm fluorescence in focused laser region for runs near linear trend line in signal vs. ions deposited. Exposures are 60 s with around 0.24 mW of 570 nm excitation focused to $w_x \times w_y = 2.06 \mu\text{m} \times 2.66 \mu\text{m}$.

power, respectively. The two experiments demonstrate linear relationships between signal and number of ions exposed over more than two orders of magnitude. This is important evidence that the 619-nm peak arises from Ba and not, e.g., Ba₂, which would exhibit a quadratic relationship with ions deposited. Zero-ion deposits are produced by retracting the Faraday cup for 1 s without pulsing the ion beam. The slope of the linear fit in (a), which

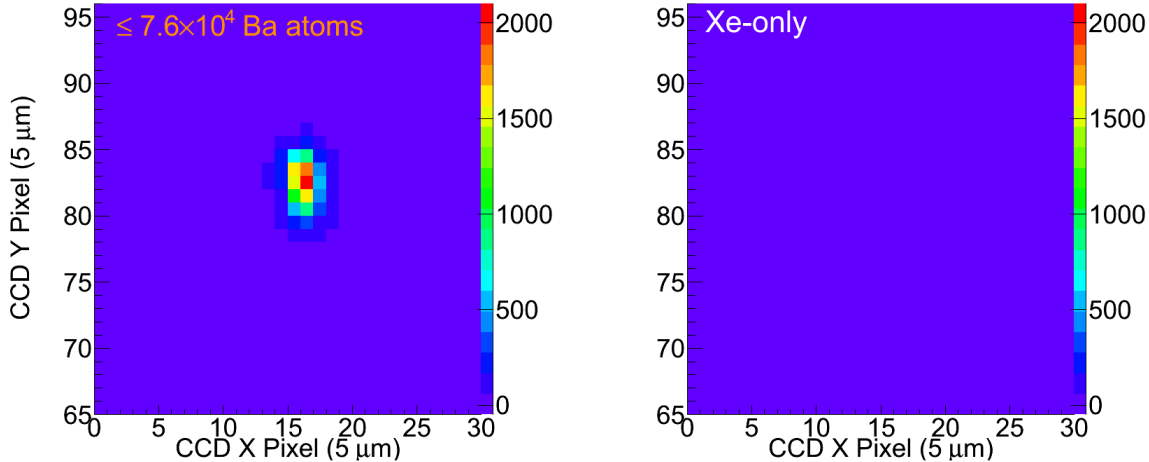


FIGURE 6.5. Raw images through 620-nm band-pass filter of a Ba^+ deposit yielding $\leq 7.6 \times 10^4$ Ba atoms, with its succeeding Xe-only deposit. Exposures are 0.5 s with 0.6 mW of 572 nm excitation focused with asphere and astigmatism compensator.

does not include a constant value, gives about 1500 ± 160 counts/mW per atom with 60-s exposures.

Images of 619-nm Ba fluorescence are shown in Fig. 6.4 for a few deposits near the linear trend line. In each case the image of the preceding Xe-only deposit is subtracted so that only the Ba fluorescence is seen. Clear, sharp peaks are observed from an instantaneous number of atoms all the way down to the single-atom level. This result is significant advance beyond the sensitivity reported in [20], and a major step toward the ultimate success of Ba tagging. It is generating excitement and interest in the nEXO collaboration.

Another very significant observation is the lack of Ba fluorescence in Xe-only deposits made after evaporating the matrix, even for large Ba^+ deposits. This is demonstrated in Fig. 6.2, where no Ba fluorescence is present in the Xe-only runs following each of the deposits. This is shown further for a $\leq 76,000$ Ba atom deposit in Fig. 6.5. The lack of a history effect after evaporation of each sample is important for the implementation of this method of Ba tagging on a probe in nEXO. Once a Ba daughter has been identified in SXe on a

cold probe, the sample can be removed without the Ba atom or ion giving false positives on subsequent events.

6.3. SCANNED IMAGES

The ultimate demonstration of single-atom imaging will be to scan the focused laser over samples with more widely separated Ba atoms, observing a peak when the laser moves over individual atoms. The resolution in a scanned image is determined by the laser spot size, even when the imaging optics have a lower resolution. Preliminary scans were performed by scanning the focusing lens in a raster pattern, using the setup described in Sec. 3.8. Summed counts/mW from a 3×3 pixel area around the focused laser are plotted vs. raster position for several deposits in Fig. 6.6. These scans are grids of 20 points in X at about $3.75 \mu\text{m}/\text{step}$, by 5 points in Y at about $4.78 \mu\text{m}/\text{step}$. An overall higher signal is observed with $48.4 \text{ Ba}^+/\text{step}$ (c), however single-atom peaks are not distinguished in the sparse deposit of $0.18 \text{ Ba}^+/\text{step}$ (b). The aspherical laser focusing lens and astigmatism compensator are used for $w_x \times w_y = 2.06 \mu\text{m} \times 2.66 \mu\text{m } 1/e^2$ laser region, though cryostat vibrations increase the exposed region as described in Sec. 3.7. This had the effect of exposing neighboring step regions to the laser. Pre-bleaching of the surface background was done with a raster of the dye laser at 580.5 nm, in a 22×7 grid centered on the 20×5 grid used during the following experiment, with 10 s at each location.

Signal levels from the scanned images in Fig. 6.6 are consistent with previous experiments, with approximately 270 ± 180 counts/mW per Ba atom with 10-s exposures. However, background levels were somewhat higher, at around 6,000 counts/mW. The scanned images of Xe-only deposits (Fig. 6.6(b)) produce a measure of step-to-step variation in the surface background which competes with the single-atom signal. The difference in counts between

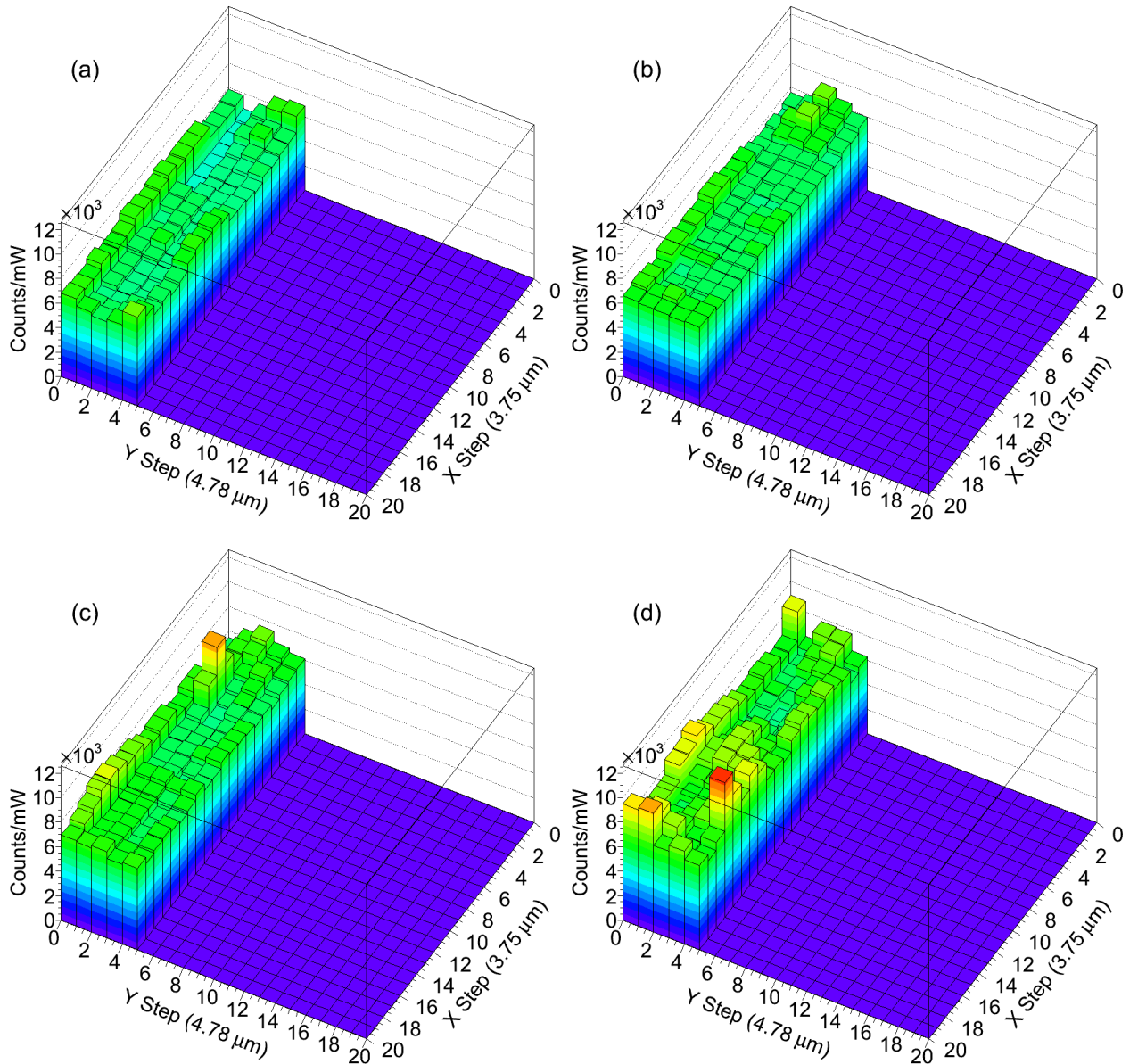


FIGURE 6.6. Early attempts at scanned images of a few deposits: (a) 0.48 Ba^+ /step, (b) Xe-only, (c) 0.63 Ba^+ /step, and (d) 5.7 Ba^+ /step. Exposures are 10-s with 0.4-0.5 mW of focused 570 nm laser.

successive grid steps is shown as a distribution in Fig.6.7 for all Xe-only deposits in this set of scanned images. The single-atom signal level of 250 counts/mW, acquired from the data set in Figures 6.2, 6.3 and 6.4, is marked with a gray dotted line. It is difficult to distinguish single Ba atoms from background fluctuations under these conditions.

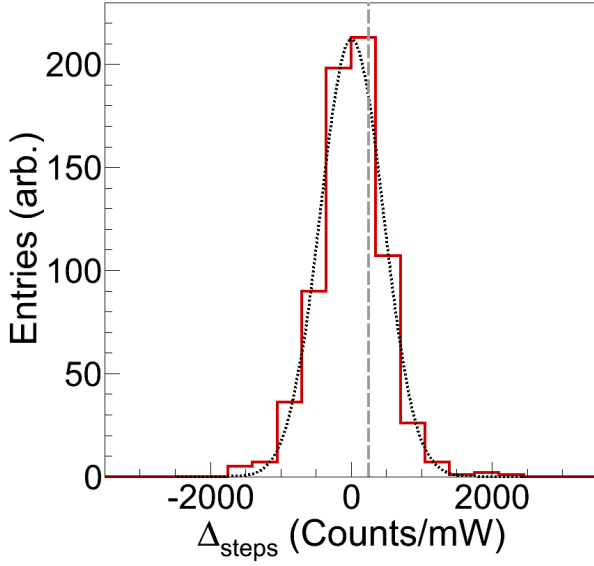


FIGURE 6.7. Distribution of difference in counts (Δ_{steps}) between successive scan frames in raw Xe-only deposits.

The single-atom signal level of 250 ± 27 counts/mW assumes 100% conversion of deposited Ba^+ ions. Thus, it is possible that single Ba atoms produce more signal than this, and that, e.g., the peaks around step (4,1) in Fig. 6.6(c) and step (16,4) in Fig. 6.6(d) are due to single atoms. However, background levels must be reduced further to be sure. The next steps in scanned imaging of Ba atoms, discussed in Sec. 7.1, will involve reducing the surface background.

CHAPTER 7

CONCLUSIONS

Single-atom-level imaging of Ba atoms in SXe has been demonstrated with deposits of Ba⁺ ions in a focused laser region. The low-bleaching 619-nm fluorescence peak was used, with around 0.2 mW of 570-nm excitation, over 10s of seconds of exposure. This achievement is a major step toward the ability to tag Ba daughters in the nEXO neutrinoless double beta decay experiment. Ba tagging is perhaps the only experimental method with the ability to probe the normal hierarchy phase space of Majorana neutrino mass.

Detailed studies of the spectroscopy of Ba and, to some degree, Ba⁺ in SXe have been presented and have been published recently in [20]. Thermal history effects and temperature dependence of fluorescence have been presented. Bleaching of the fluorescence was studied at various excitation wavelengths and intensities, with comparison to a model of the rate equations. Ultimately, these studies were utilized in reaching the single-atom-level sensitivity with the 619-nm fluorescence, as well as in imaging the 577- and 591-nm fluorescence at the $\leq 10^3$ -atom level. Blue excitation of Ba⁺ deposits in SXe has revealed several newly reported emission peaks which are candidates for matrix-isolated Ba⁺ ions.

7.1. FUTURE WORK

The next step in the demonstration of Ba tagging in SXe will be imaging separate Ba atoms in SXe in images in which the laser beam is rastered across an area of the sample.

To achieve good scanned images, overcoming the surface background emission is the first priority. Pre-bleaching of the sapphire window has been done in the first attempts

at scanned images, though further study is needed to perfect the procedure. Ba emission could be separated from background by different emission lifetimes, as is done in single quantum dot or molecule studies (<http://epub.uni-regensburg.de/9917/1/Boehmer.pdf> or <http://pubs.acs.org/doi/abs/10.1021/cr980132z?journalCode=chreay>). Studies of fluorescence lifetimes of the 619-nm signal vs. the background using a pulsed laser and a photomultiplier tube for fast detection will be explored, in order to determine whether a fluorescence time gating technique may remove background. One exciting outcome of the atom counting inherent in scanned images is that they will provide the first measurement of the percentage of deposited Ba⁺ ions that are visible as Ba atoms via the 619-nm fluorescence.

To improve Ba tagging efficiency, it would be good to be able to image Ba atoms in other matrix sites. Exploration of re-pumping wavelengths for the 577- and 591-nm peaks will be done using tunable lasers in the infrared. The ability to count atoms emitting with these different wavelengths would be very valuable. It is not yet known if Ba⁺ captured from LXe will remain as Ba⁺ or neutralize to Ba. The ability to count Ba⁺ ions is also important and will be pursued by continuing study of the candidate Ba⁺ emission peaks with blue excitation.

Ultimate demonstrations of Ba tagging in SXe will be done by grabbing out of LXe on cold probes. Construction of an apparatus is occurring simultaneously in our laboratory, in which a cold probe can be lowered into a LXe cell. Initial tests of freezing LXe on Joule-Thompson probes have been successful. Ba⁺ will be produced by laser ablation of Ba metal and drifted into the LXe, a process demonstrated in [18], and onto the cold probe by electrodes. In order to reach temperatures around 10 K, where the Ba fluorescence is strong, the probe will be raised to an isolated pumping region for further cooling and observation.

The next breakthrough in particle/nuclear physics may lie in the discovery of Majorana neutrino mass, and the search for $0\nu\beta\beta$ is of key importance in this discovery. Extreme sensitivity in experimental technique is required, and ingenious ideas, including the great challenge of Ba tagging must be invented and demonstrated to reduce competing backgrounds to zero over operating times of many years. It is expected to reach unprecedented sensitivity in neutrinoless double beta decay in the second phase of nEXO. Based on progress that has been made, including this work, the future of Ba tagging is bright.

BIBLIOGRAPHY

- [1] C.D. Ellis and W.A. Wooster, “The average energy of disintegration of radium e,” *Proceedings of the Royal Society (London)* **A117** 109-123 (1927).
- [2] F. Wilson, *American Journal of Physics* **36**, 12 (1968).
- [3] Y. Fukuda *et al.* (Super-Kamiokande Collaboration), *Phys. Rev. Lett.* **81** 1562 (1998).
- [4] S.T. Petcov, W. Rodejohann, T. Shindou, Y. Takanishi, *Nuclear Physics B* **739**, 208233 (2006).
- [5] M. Danilov *et al.*, *Physics Letters B* **480**, 1218 (2000).
- [6] K.A. Olive *et al.* (Particle Data Group), “14. Neutrino Mass, Mixing, and Oscillations,” *Chin. Phys. C* **38**, 090001 (2014) (<http://pdg.lbl.gov>)
- [7] P.A.R. Ade *et al.* (Planck Collaboration), *Astronomy and Astrophys.* **571**, A16 (2014).
- [8] N. Steinbrink *et al.*, *New Journal of Physics* **15**, 113020 (2013).
- [9] J. Albert *et al.* (EXO-200 Collaboration), *Phys. Rev. C* **89**, 015502 (2014).
- [10] M. Moe, *Phys. Rev. C* **44**, R931 (1991).
- [11] M. Auger *et al.*, *JINST* **7**, P05010 (2012).
- [12] R. Nielson *et al.*, *Nuclear Instruments and Methods in Physics Research A* **608**, 68 (2009).
- [13] E. Conti *et al.*, *Phys. Rev. B* **68**, 054201 (2003).
- [14] M. Auger *et al.*, *Phys. Rev. Lett.* **109**, 032505 (2012).
- [15] J. Albert *et al.* (EXO-200 Collaboration), *Nature* **510**, 229 (2014).
- [16] N. Ackerman *et al.* (EXO-200 Collaboration), *Phys. Rev. Lett.* **107**, 212501 (2011).
- [17] A. Gando *et al.* (KamLAND-Zen Collaboration), *Phys. Rev. C* **86**, 021601 (2012).
- [18] K. Hall, *In-situ Laser Tagging of Barium Ions in Liquid Xenon for the EXO Experiment*. Colorado State Universtiy Thesis/Dissertation (2012).

- [19] K. Twelker *et al.*, *Review of Scientific Instruments* **85**, 095114 (2014).
- [20] B. Mong *et al.*, *Phys. Rev. A* **91**, 022505 (2015).
- [21] J. Albert *et al.* (EXO-200 Collaboration), *Phys. Rev. C* **92**, 045504 (2015).
- [22] J. J. Curry, *Journal of Physical and Chemical Reference Data* **33**, 725 (2004).
- [23] J. Migdalek and W. E. Baylis, *Phys. Rev. A* **42**, 6897 (1990).
- [24] V. A. Dzuba and J. S. M. Ginges, *Phys. Rev. A* **73**, 032503 (2006).
- [25] A. Mohanty *et al.*, *Hyperfine Interactions* **233**, 113-119 (2015).
- [26] N. Yu, W. Nagourney, H. Dehmelt, *Phys. Rev. Lett.* **78**, 26 (1997).
- [27] S. De, U. Dammalapati, K. Jungmann, L. Willmann, *Phys. Rev. A* **79**, 041402(R) (2009).
- [28] W. Neuhauser, M. Hohenstatt, P. Toschek, and H. Dehmelt, *Phys. Rev. Lett.* **41**, 233 (1978).
- [29] M. Green *et al.*, *Phys. Rev. A* **76**, 023404 (2007).
- [30] E. Whittle, D. Dows, G. Pimentel, *The Journal of Chemical Physics* **22**, 1943 (1954).
- [31] C. Crepin-Gilbert and A. Tramer, *Int. Reviews in Physical Chemistry* **18**, No. 4, 485-556 (1999).
- [32] H. A. Jahn and E. Teller, *Proceedings of the Royal Society of London A* **161**, 220-235 (1937).
- [33] M. Ryan *et al.*, *J. Phys. Chem. A* **114**, 3011-3024 (2010).
- [34] R. Pellow and M. Vala, *The Journal of Chemical Physics* **90**, 5612 (1989).
- [35] L. Wöhlin, “The Colutron, a Zero Deflection Isotope Separator,” *Nuclear Instruments and Methods* **27** 55-60 (1964).

- [36] S. Cook, *Detection of Small Numbers of Barium Ions Implanted in Solid Xenon for the EXO Experiment*. Colorado State Universtiy Thesis/Dissertation (2012).
- [37] B. Mong, *Barium Tagging in Solid Xenon for the EXO Experiment*. Colorado State Universtiy Thesis/Dissertation (2011).
- [38] A. C. Sinnock, *J. Phys. C: Solid St. Phys.* **13**, 2375-91 (1980).
- [39] D. Fairbank (private communication, 2015).
- [40] Tache, J.-P., *Applied Optics* **26**, 429 (1987).
- [41] D. F. Nelson, M. D. Sturge, *Physical Review* **137**, 4A (1965).
- [42] C. Guguschev, J. Gotze, M. Gobbels, *American Mineralogist* **95**, 449-455 (2010).
- [43] R. A. Ford, O. F. Hill, *Spectrochimica Acta* **16**, 493-496 (1960).
- [44] D. S. McClure, *Solid State Phys.* **9**, 399-525 (1959).
- [45] D. Richard Sears, Harold P. Klug, *The Journal of Chemical Physics* **37**, 12 (1962).